UNIVERSITY OF OXFORD

DEPARTMENT OF CHEMISTRY

Surface Mapping of Faceted Metal Oxides by Chemical Probe-assisted NMR for Catalytic Applications

BY

YUNG-KANG PENG

ST. EDMUND HALL

A THESIS SUBMITTED FOR THE DEGREE
DOCTOR OF PHILOSOPHY
2017

DECLARATION

I confirm this is my own work unless stated otherwise and the use of all materials from other sources has been properly and fully acknowledged.

Yung-Kang Peng

DEDICATION

To my parents

ACKNOWLEDGEMENTS

First of all, I would like to thank Professor Edman Tsang for the opportunity to join his research group and his advice, support and guidance throughout the past four years. Additionally, I would also like to thank the Clarendon scholarship of Oxford University for the three-year full funding and the financial support from Taiwan study abroad scholarship for the final year of thesis writing. I am indebted to St. Edmund Hall, the Department of Chemistry and the University of Oxford for the provision of a stimulating research environment and facilities that allowed me to develop my chemistry skills during my DPhil study.

The research presented in this thesis would not have been possible without the valuable support I have received from the following people: Dr. Fenglin Liao for her assistance with the synthesis of ZnO nanoparticles presented in Chapter 4. Dr. Jin Qu (East China University of Science & Technology, China) for the DFT ZnO calculation presented in Chapter 4. Dr. William Mayor for the training of EPR. Dr. Ye Lin for TEM and PL investigations on ZnO nanoparticles presented in Chapter 4 and 5. Dr. Zhang Li and Ms. Yiying Fu (Fudan University, China) for the training of molecule-adsorbed NMR sample preparation and the collection of NMR data presented in Chapter 4, 5 and 6. Dr. Nick Rees in CRL for his kind help in solid-state NMR measurement. Prof. Hung-Lung Chou (National Taiwan University of Science and Technology, Taiwan) for the DFT TiO_2 calculation presented in Chapter 6. Dr. Yichen Hu for the synthesis and catalytic testing of TiO_2 nanoparticles. Mr. Ivo F. Teixeira for TEM investigation on TiO_2 nanoparticles presented in Chapter 6. Dr. Ashley Shepherd for her assistance with XPS data collection and analysis.

I would like to thank all the Tsang group member of past and present: Dr. Simon Fairclough, Dr. Keizo Nakagawa, Dr. Weiran Zheng, Dr. Terry Wu, Dr. Abdullah Khan, Dr. Amy Kolpin, Dr. Clive Eley, Dr. Tiantian Jia, Dr. Aaron Lau, Dr. Hanif Mahadi, Dr. Fenglin Liao, Dr. Ieuan Ellis, Dr. Tugce Ayvali, Dr. Ian McPherson, Dr. Haohong Duan, Dr. Pu Zhao, Dr. Ye Lin, Dr. Benedict Lo, Ms. Hannah Kreissl, Mr. Bin Yu, Mr. Ivo Freitas Teixeira, Ms. Elizabeth Raine, Mr. Sultan Alshuhri, Ms. Meng-Jung Lee, Mr. Josh Fellowes, Mr. Thomas Lau, Mr. Tim Sudmeier, Mr. Jiri Kulhavy, Mr. Linus Lin, Mr. Simson Wu, Ms. Kirsty Purchase, Ms. Tatchamapan Yoskamtorn, Ms. Tianyi Chen.

Finally, I would like to thank all of my friends who have supported me throughout this journey. I owe it all to you.

PUBLICATIONS

My main project in Tsang's group is to develop a new surface technique that can provide facet-specific information of metal oxide surface features in both qualitative and quantitative manner. So far, two papers on zinc oxide and one paper on titanium oxide have been published.

1. **Yung-Kang Peng**, Lin Ye, Jin Qu, Li Zhang, Yingyi Fu, Ivo F. Teixeira, Ian James McPherson, Heyong He and **S. C. Edman Tsang***, "Trimethylphosphine-assisted Surface Fingerprinting of Metal Oxide Nanoparticle by ^{31}P Solid-state NMR: A Zinc Oxide Case Study", *J. Am. Chem. Soc.* **2016**, *138*, 2225–2234.

2. **Yung-Kang Peng**, Yingyi Fu, Li Zhang, Ivo F. Teixeira, Lin Ye, Heyong He and **Shik Chi Edman Tsang***, "Probe-Molecule-Assisted NMR Spectroscopy: A Comparison with Photoluminescence and Electron Paramagnetic Resonance Spectroscopy as a Characterization Tool in Facet-Specific Photocatalysis", *ChemCatChem* **2017**, *9*, 155–160.

3. **Yung-Kang Peng**, Yichen Hu, Hung-Lung Chou, Yingyi Fu, Ivo F. Teixeira, Heyong He and **S. C. Edman Tsang***, "Mapping Surface-modified Titania Nanoparticles with Implications for Activity and Facet Control", *Nat. Commun.* **2017**, *8*, 675.

In addition to the above project in Tsang's group, I also have a side bio-imaging project using magnetic nanoparticles as magnetic resonance imaging (MRI) contrast agents for brain imaging and stem cell collection in collaborations with Hong Kong Baptist University and National Taiwan University. Two published papers and one manuscript provisionally accepted are listed below:

1. **Yung-Kang Peng**, Cathy N. P. Lui, Tsen-Hsuan Lin, Chen Chang, Pi-Tai Chou, Ken K. L. Yung and **S. C. Edman Tsang***, "Multifunctional Silica-coated Iron Oxide Nanoparticles: A Facile Four-in-one System for In Situ Study of Neural Stem Cell Harvesting", *Faraday Discuss.* **2014**, *175*, 13−26.

2. **Yung-Kang Peng**, Cathy N. P. Lui, Yu-Wei Chen, Shang-Wei Chou, Pi-Tai Chou, Ken K. L. Yung* and **S. C. Edman Tsang***, "Engineering of Single Magnetic Particle Carrier for Living Brain Cell Imaging: A Tunable T1-/T2-/Dual-Modal Contrast Agent for Magnetic Resonance Imaging Application", *Chem. Mater.* **2017**, *29*, 4411–4417.

3. **Yung-Kang Peng**, Cathy N. P. Lui, Yu-Wei Chen, Shang-Wei Chou, Pi-Tai Chou, Ken K. L. Yung* and **S. C. Edman Tsang***, "Engineered Core-Shell Magnetic Nanoparticle for MR Dual-Modal Tacking and Safe Magnetic Manipulation of Ependymal Cells in Live Rodent", *Nanotechnology*, **2018**, *29*, 015102.

However, the bio-imaging part won't be included in this thesis as it is difficult to integrate both projects to give an overall introduction. As the bio-imaging project is an extension of my master research at National Taiwan University, I would prefer to focus on the first project "the newly-developed surface technique and its applications on metal oxides", conducted throughout my DPhil study at University of Oxford.

ABSTRACT

Semiconductive metal oxides are of great importance in environmental remediation and electronics because of their ability to generate charge carriers when excited with appropriate energy. The electronic structure, light absorption and charge transport properties have made the transition metal oxides an attractive material as photocatalyst. Recently, facet-engineering by morphology control has been intensively studied as an efficient approach to further enhance their photocatalytic performance.

However, various processing steps and post-treatments used in the preparation of facet-engineered particles may generate different surface active sites which may affect their photocatalysis. Moreover, many traditional techniques (PL, EPR and XPS) used for materials characterization (oxygen vacancy, hydroxyl group, cation…etc.) are not truly surface specific but analyzing a range from surface few layers to bulk. Accordingly, they can only provide very limited information on chemical states of the surface active features and their distribution among facets, causing difficulties to unambiguously correlate facet-dependent results with activity. As a result, this often leads to different interpretations amongst researchers during the past decades.

As the publications of titanium and zinc ranked top two among studies of first row of transition oxides in the past decades, this thesis will firstly review on the disagreements generated among researchers when they correlated the performance of ZnO and TiO_2 with their facet activities based on traditional techniques. As there are shortcomings of these techniques in producing truly facet-dependent features, some results can be misleading and with no cross-literature comparison. To address these issues, we have

developed a new technique “probe-molecule-assisted NMR” which allows a genuine differentiation of surface active sites from various facets. This surface-fingerprint technique has been demonstrated to provide both qualitative (chemical shift) and quantitative (peak intensity) information on the concentration and distribution of truly surface features among facets. In light of the new technique, this thesis will revisit the facet-dependent photocatalytic properties and shed light on these issues.

Key words: Surface characterization, Facet-dependent activity, Surface features, Oxygen vacancy, Nuclear magnetic resonance.

THESIS OVERVIEW

This thesis can be broken down into an introduction (chapter 1), two methods chapters (chapter 2 and 3), three results chapters (chapter 4-6) and an overall conclusion (chapter 7). The contents of each chapter are as follows

Chapter 1 reviews how researchers correlate the performance of the two most popular photocatalysts, ZnO and TiO_2, wih their facet activities based on data collected from traditional characterization techniques. The background of probe-assisted NMR and its corresponding results on ZnO and TiO_2 will also be briefly introduced.

Chapter 2 gives the background and details of the characterization techniques used.

Chapter 3 provides detailed synthetic methods and instrument operating parameters.

Chapter 4 focuses on the surface mapping of ZnO nanoparticles with preferential exposed facets by the probe-assisted NMR technique.

Chapter 5 compares the surface information of ZnO obtained by probe-assisted NMR with traditional characterization tools such as photoluminescence and electron paramagnetic resonance spectroscopy.

Chapter 6 focuses on another metal oxide, TiO_2. The chemical probe-assisted NMR is found not only can differentiate surface features between facets but also distinguish the electronic effect of surface-adsorbed molecules imposed on those surface features.

Chapter 7 concludes and outlooks the impact of the work presented.

THESIS CONTENTS

Chapter 1 Introduction: facet-dependent photocatalysis of nanosize metal oxide and the progress of their characterization

1.1. Photocatalysis

Environmental pollution becomes one of the most severe issues we are currently facing on a global scale. The release of toxic chemicals and industrial waste into the air and water has resulted in the up-rises of pollution-related diseases and climatic changes. Photocatalysis using inexhaustibly irradiations of the Sun has shown its potential as an environmentally sustainable and economically viable way to address those concerns during the past decades [1,2]. The term "photocatalysis" consists of the combination of photochemistry and catalysis implying that light and a catalyst are necessary to initiate or to accelerate a redox reaction. In most cases, heterogeneous photocatalysis involving photoreactions at the catalyst surface refers to semiconductor photocatalysis. Nowadays, metal oxide materials with well-defined sizes, structures, compositions and shapes have been extensively developed as photocatalysts for various reactions including water splitting, CO_2 reduction and pollutant degradation [3-5].

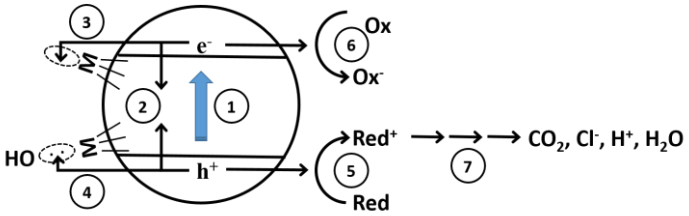

Figure 1-1. Seven primary steps in the mechanism of photocatalysis [6].

In general, there are seven basic steps are involved in the mechanism of semiconductor photocatalysis [6] **(Figure 1-1)**: (1) formation of charge carriers by photon absorption; (2) charge carrier recombination; (3) trapping of a conduction-band electron at a surface

cation site (i.e. M^{n+}) to yield $M^{(n-1)+}$; (4) trapping of a valence-band hole at a surficial M-OH group; (5) initiation of an oxidative pathway by a valence-band hole; (6) initiation of a reductive pathway by a conduction-band electron; and (7) further thermal (e.g., hydrolysis or reactions with active oxygen species) and photocatalytic reactions to yield products. Fundamental studies concerning those very fast photocatalytic processes inside and at the surface of the semiconductor, are not carried out very often. However, the knowledge of these processes is of utmost importance for the understanding of the photocatalytic reaction mechanism and thus for a better design of photocatalytic systems.

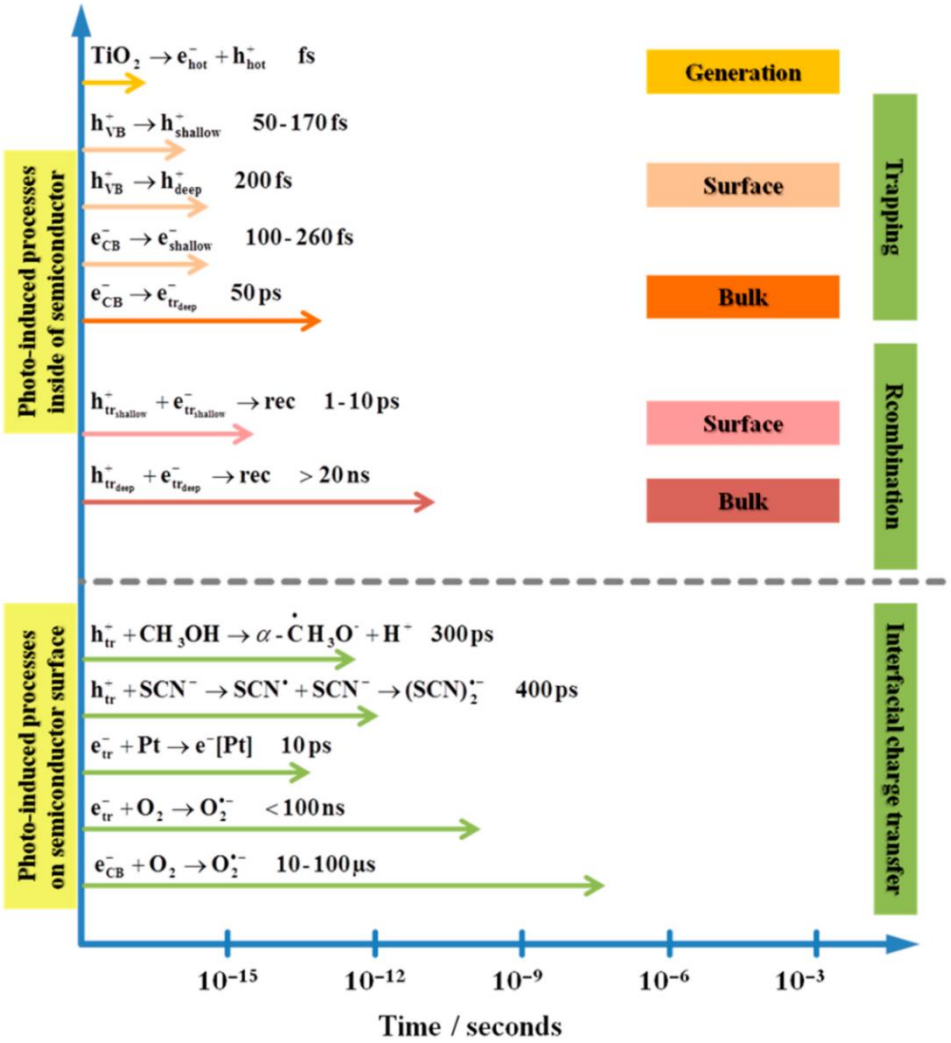

Figure 1-2. Photoinduced reactions in TiO_2 photocatalysis and corresponding time scales [3].

Figure 1-2 provides an overview of the photoinduced events inside and on the surface of a TiO_2 photocatalyst in the time scale region from femtoseconds to microseconds [3]. Generally, the efficiency of photocatalytic processes is rather small that most of the photogenerated e^-/h^+ pairs (~90%) recombine rapidly after excitation and therefore low photonic efficiency (<10%) for most semiconductor-based photocatalytic reactions [6]. Since this recombination process is the major disadvantage in semiconductor photocatalysis, many strategies have been adopted during the past to improve the photonic efficiency (inhibit recombination process).

1.2. Strategies to improve photocatalytic efficiency

Comparing to the time scale of charge recombination in bulk (nano second, **Figure 1-2**), the photogenerated e^-/h^+ can be trapped by surface states forming $e_{shallow}^-/h_{shallow}^+/h_{deep}^+$ in a much shorter time scale (femto second) right after the generation of e^-/h^+ pairs [7]. Accordingly, the increase of surface states can effectively extract photogenerated e^-/h^+ to catalyst surface for later redox reaction and avoid their recombination in bulk. Therefore, the shrinkage of particle size has been pursued as a strategy to boost the number of trapped sites (catalytic sites) on catalyst surface for a better photocatalytic activity. Later, cation/anion doping has also been adopted to further counter the recombination problem by enhancing the charge separation as the dopants may more efficiently trap electrons/holes [1-4]. However, as shown in **Figure 1-2**, the recombination rate of surface $e_{shallow}^-$ and $h_{shallow}^+$ (pico second) is still at least ten times faster than the interfacial charge transfer (i.e. steps (5) and (6) in **Figure 1-1**), which is the rate limiting step in heterogeneous photocatalysis. According to Fogler [8], this interfacial charge transfer can be divided into following five independent steps as shown in **Figure 1-3**: (1) Mass transfer of the reactant(s) (e.g. A) in the bulk fluid/gas phase to the surface. (2) Adsorption of the reactant(s) onto the photon activated surface.

(3) Photocatalysis reaction for the adsorbed phase on the surface (e.g. A/B). (4) Desorption of the intermediate(s) (e.g. B) from the surface. (5) Mass transfer of the intermediate(s) (e.g. B) from the interface region to the bulk fluid/gas.

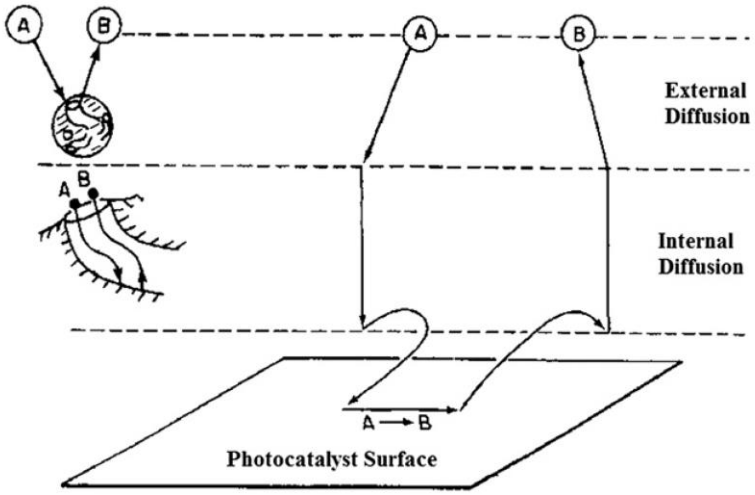

Figure 1-3. Adsorption/desorption steps in heterogeneous catalytic reaction [8].

In terms of rate determination, the overall rate of photocatalytic reaction is equal to the slowest step of all the elementary steps of the reaction. As the mass transfer steps (step 1 and 5) are usually very fast compared with the reaction steps (step 2, 3 and 4), the molecules in the immediate vicinity of the active sites are indistinguishable from those in the bulk fluid/gas phase. In this scenario, the mass transfer steps are not rate limiting and do not affect the overall rate of photocatalytic reaction. Vinodgopal and Kamat first reported the dependence of the photodegradation rate of the organic molecules on surface coverage of the photocatalysts used [9]. This outlines the importance of the adsorption-reaction-desorption interactions between molecules and surface of the catalyst during the reaction (step 2, 3 and 4). Recently, the surface/facet-tailoring for photocatalytic materials has indeed been proved an efficient strategy to further enhance their photocatalytic performance [5].

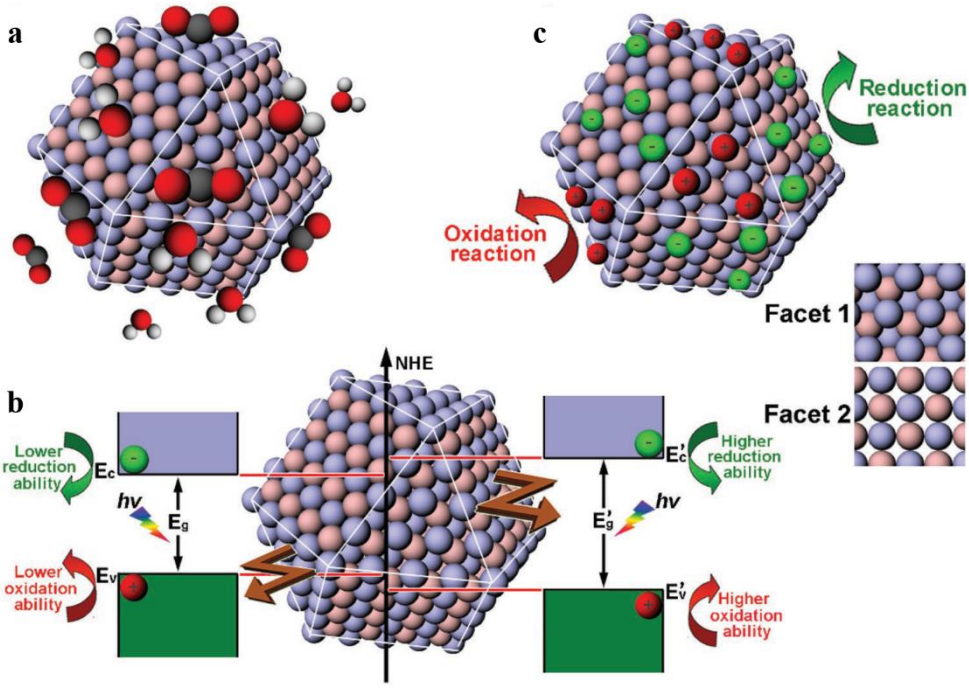

Figure 1-4. Schematics illustrating the important roles of facets in the surface design of photocatalytic materials. a) Adsorption and activation of reactant molecules on different facets. b) Redox abilities of photogenerated charge carriers tuned by the surface electronic band structures of different facets. c) Accumulations of photogenerated electrons or holes on different facets [5].

The facets exposed on photocatalyst surface have been found to affect the photocatalytic activity through various mechanisms. For example, (1) surface atomic arrangements determine the adsorption and activation energy of reaction molecules, and thus tuning catalytic activity and selectivity **(Figure 1-4a)** [10,11]. (2) The surface electronic structures (i.e. surface chemical states), which vary with surface facets, provide the photogenerated charge carriers with different redox abilities for catalytic reactions **(Figure 1-4b)** [12]. (3) When the semiconductor is enclosed by multiple facets, the difference in electronic structures of surface facets result in the spatial charge separation which intrinsically separates the photogenerated electrons and holes on different facets for reduction and oxidation reaction, respectively **(Figure 1-4c)** [13-15]. These considerations have added exciting variables in tailoring morphology of nanoparticles (NPs) with preferentially exposed facets during the past decades.

Unfortunately, facets with high reactivity are unstable and tend to diminish rapidly to minimize surface energy during the crystal growth. Accordingly, a structural directing specie (SDS) or surfactant is usually employed in the shape control of NPs, which renders them in metastable and high-energy forms [16]. Those adsorbates which range from simple inorganic species, organic molecules to polymer can subtly modify the chemical state of surface features (especially metal cations) and provide a kinetic growth control for the formation of metastable shaped NPs. As the growth rate of a crystal facet depends on the surface energy (high-energy facets grow more quickly than low energy facets), different morphologies of NP could thus be prepared by using various structural directing molecules [16]. In the facet engineering for decent photocatalysts, the simplest way is to increase the percentage of the exposed facets with higher photocatalytic performance. The high coverage of one facet on surface would facilitate the investigations on facet-dependent photocatalytic activity and related mechanisms. Accordingly, the understanding gained from the mechanism study can provide a guide for identifying the facet with high activity for increased photocatalytic performance. This rational approach has been widely used for the development of facet-engineered photocatalysis of transition metal oxide during the past decades.

1.3. Different interpretations amongst researchers

Usually, adsorbates (i.e. SDS or surfactant) employed in the shape control of NPs are removed before the photocatalytic testing to avoid its interfering to the interested properties on this surface. However, in most cases, those so-called “clean surfaces” were not so clean as they claimed. Noticed that residue adsorbates have been shown to remain on the facets and influence the adsorption of reactant molecules and, in particular, the chemical states of surface cation [17]. This forms a physical obstacle from reliably evaluating the facet-dependent photocatalytic performance. Also, from

thermodynamic point of view, a new equilibrium between the uncapped high energy facet and its exposed environment (e.g. ambient) must have achieved to minimize the increased system energy. This stabilization usually accompanies with the generation of surface features such as oxygen vacancy (V_o), hydroxyl group or cation with various chemical states, which play a decisive role in various applications (e.g. optoelectronic devices, heterogeneous (photo)catalysis). Given that each facet possesses distinctive intrinsic energy, it is understandable that both distribution and concentration of those surface features differ from facet to facet after reaching equilibrium with its exposed environment. Moreover, various processing steps used for shaped NPs from group to group further complicate the correlation of facet activity and thus always lead to different interpretations amongst researchers. In our opinion, the blocking stone to deeper the understanding on the facet-dependent photocatalysis is the lack of proper characterization technique/method that can provide facet-based information on both qualitative and quantitative manner. As the studies of titanium and zinc ranked top two among first row of transition oxides during the past decades **(Figure 1-5)**, we herein focus on their facet-dependent photocatalysis and corresponding characterization techniques adopted for activity correlation.

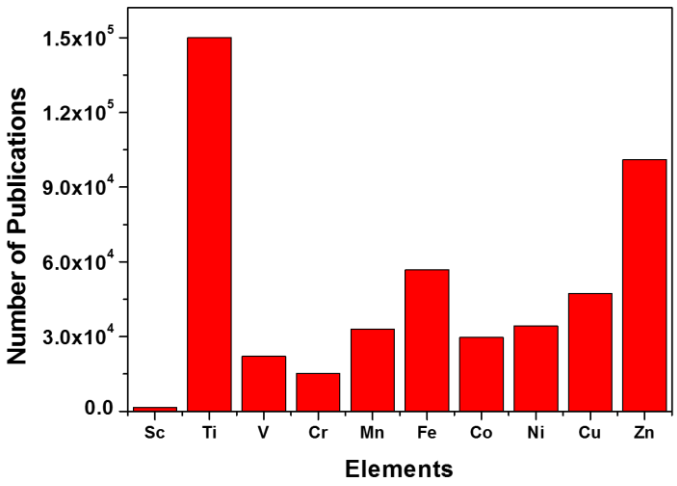

Figure 1-5. Comparison of total numbers of publications on different transition oxides since 2000 (collected based on Web of Science database).

1.4. Facet-dependent photocatalysis of ZnO NPs and characterization

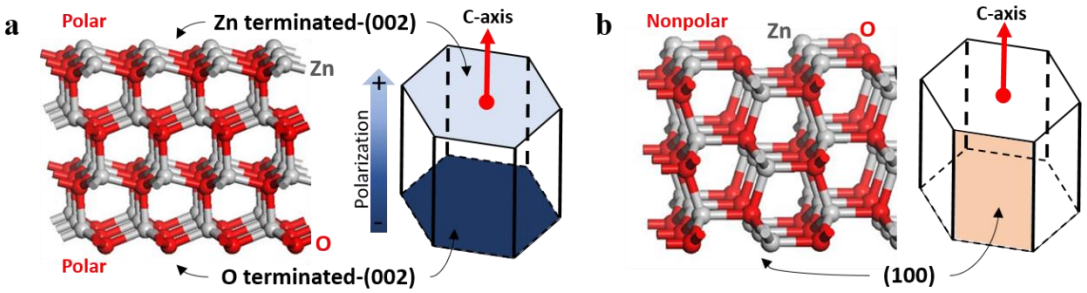

Figure 1-6. Schematic illustration of the hexagonal structure (wurtzite) of ZnO. The three main crystallographic exposed planes and corresponding atomic arrangement are shown in (a) Zn-(002) and O-(002) facets with the intrinsic polarization field and (b) nonpolar (100) facet.

ZnO is a wide band gap semiconductor (3.3 eV) with a high exciton binding energy of 60 meV and piezoelectric properties. It is well known that ZnO is a polar crystal (wurtzite structure) composed of tetrahedrally coordinated O^{2-} and Zn^{2+} ions stacking along the *c*-axis and thus its surface consists of a positively charged Zn-terminated (002) plane (Zn-(002)), a negatively charged O-terminated (002) plane (O-(002)) **(Figure 1-6a)** and nonpolar planes (100) with C_{6V} symmetry **(Figure 1-6b)** [18]. The specificity of polar surface comes from the combined effect of orientation and termination which is responsible for the existence of a macroscopic polarization along the surface normal and a surface electrostatic instability. Similar to the case of ferroelectric materials, a depolarization mechanism is required to stabilize these surfaces, which can be achieved in many ways: by a deep modification of the surface electronic structure (i.e. total or partial filling of surface states) or by strong changes in the surface stoichiometry (e.g. surface reconstruction, formation of surface defects or adsorption of foreign species) [18]. These processes may change the original surface configurations, in which the local environment of the surface atoms is very different from the bulk or non-polar facet, and

new electronic surface states (e.g. defects) may appear in the bandgap of the metal oxide. Accordingly, tailoring ZnO NPs with preferentially exposed polar (002) facets has been receiving increasing attention due to superior performances in solar cells and photocatalysis [19-21], methanol synthesis [22,23], optoelectronics [24] and gas sensing [25], which were all attributed to increased concentration of oxygen vacancies (V_o). Particularly, in the field of photocatalysis which is closely associated with the coordination environment and electronic states of the surface active atoms.

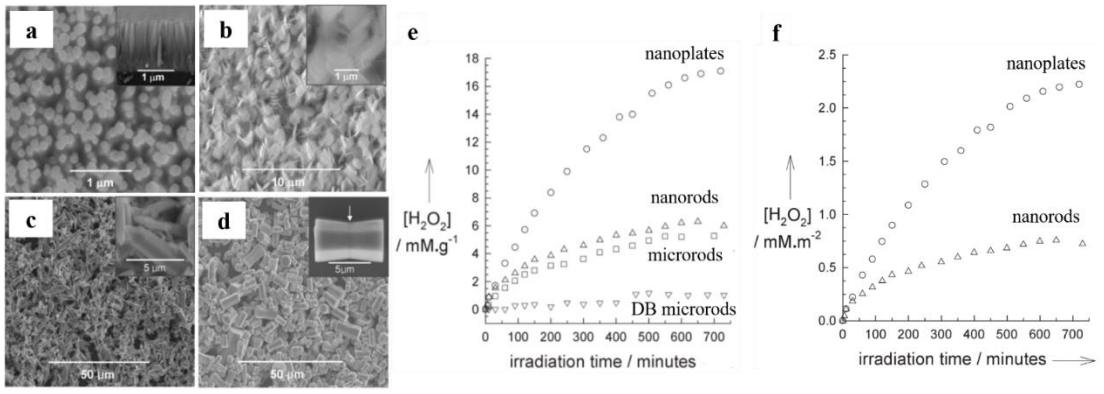

Figure 1-7. a-d) SEM images of ZnO (a) nanorods, (b) nanoplates, (c) microrods and (d) dumbbell (DB) microrods. (e) Weight-normalized and (f) surface-area-normalized time profiles of the evolution of H_2O_2 in UV-illuminated (wavelength $\lambda > 300$ nm) suspensions [19].

The facet activity of polar Zn-(002) facet in the photocatalytic generation of H_2O_2 was firstly showed by Choy's group [19]. They prepared various ZnO morphologies **(Figure 1-7a-d)** with calculated surface area of Zn-(002) facet (according to SEM images) in the order of nanoplates (3.53 m^2/g), nanorods (0.12 m^2/g), microrods (0.03 m^2/g) and dumbbell microrod (0 m^2/g). Noted that the dumbbell microrod with masked Zn-(002) faces (indicated by white arrow in **Figure 1-7d inset**) exposed only O-(002) faces at both ends. The area of the exposed polar Zn-(002) facet was found proportional to the photocatalytic H_2O_2 generation normalized either by weight **(Figure 1-7e)** or by surface area **(Figure 1-7f)**. However, using electron microscopy as a major characterization

technique to establish the correlation of photocatalytic performance to facet activity is far from enough without controversy. For decades, a high $V_{o\ surface}$ concentration and its relation to exposed (002) facets have been regarded as the main criterion for high photocatalytic activity. It would be ideal to correlate the measured photocatalytic activity directly with the Vo surface concentration in quantitative manner. However, the $V_{o\ surface}$ of ZnO is highly unstable when in contact with environment (i.e. H_2O favors the formation of OH surface or O2 for surface adsorption). The high affinity say for water molecule to $V_{o\ surface}$ on ZnO O-(002) was indeed observed experimentally by Diebold et al. using STM and scanning tunneling spectroscopy (STS) [26]. Accordingly, the mechanism proposed by Jang et al. [19] and McLaren et al. [21] that the preferentially adsorbed OH^- on positive charged polar surface might be another factor for photocatalytic activity. These ions can react with photo-generated holes (h^+) to produce reactive species •OH radicals, hence enhancing the photocatalytic activity. Nowadays, the photocatalytic mechanism of ZnO is still not clear mainly due to the lack of appropriate technique to provide quantitative $V_{o\ surface}$ and OH correlation in relevant to facet-dependent properties of ZnO.

1.4.1. Using PL as a main facet-characterization technique

To probe bulk defect sites, photoluminescence spectroscopy (PL) at short excitation wavelength has been commonly employed to characterize transition metal oxide semiconductors. These materials can capture the photons from the excitation source with energy equal to or greater than their band gap energy. The photons are then absorbed by the oxide semiconductor nanocrystal and cause the generation of photoexcited electrons and holes in the conduction and valence bands, respectively. The excited electron–hole pairs, known as excitons, are then subject to recombination, in particular, on the defect centers to give trap-state luminescence.

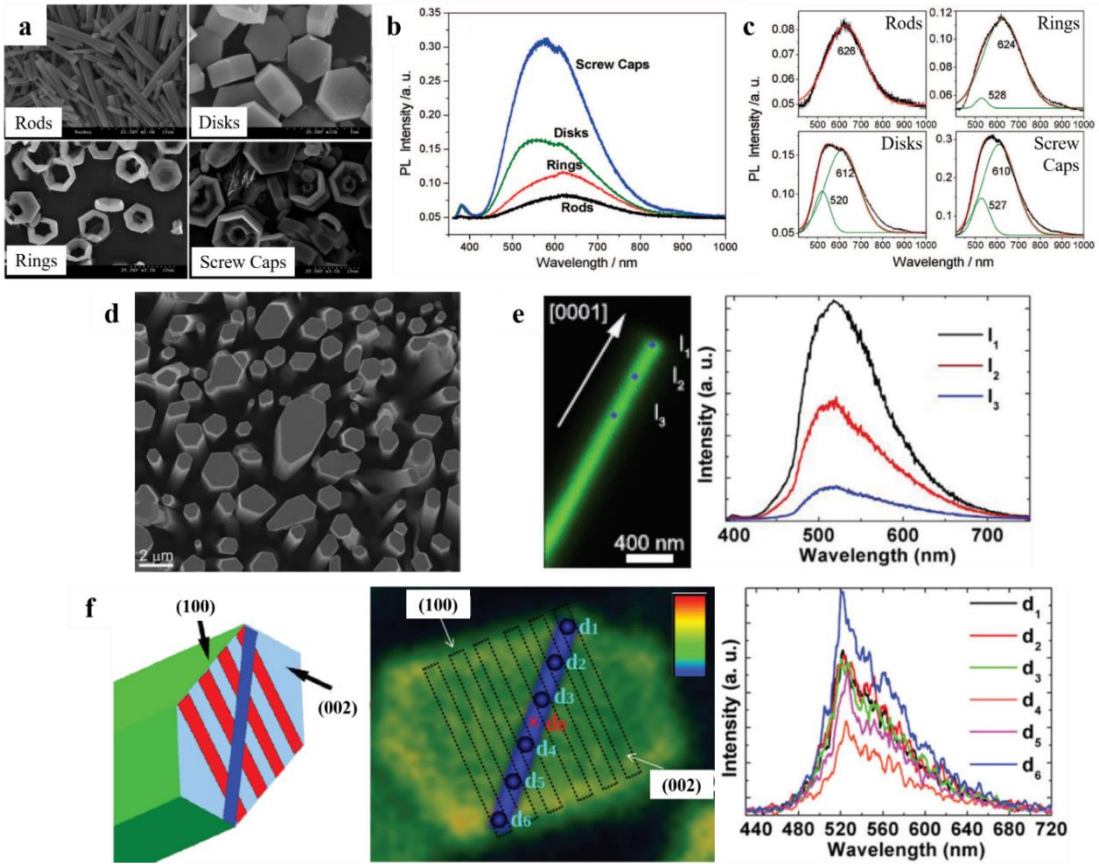

Figure 1-8. (a) SEM images of the synthesized ZnO with various morphologies: rods, disks, rings and screw caps [20]. (b) PL spectra and (c) corresponding Guassian fit results of the 410-1000 nm emissions of the synthesized ZnO with various morphologies [20]. (d) Top SEM view of ZnO nanowire (NW) array [33]. (e) Confocal PL intensity microscope image of a thin ZnO NW lying on its side and corresponding PL spectra at three different spatial locations (I_1 to I_3) along the [0001] direction [33]. (f) Confocal intensity images of an individual ZnO NW on the (002) surface and corresponding PL spectra of the green luminescence taken at six spatial locations (d_1 to d_6) along the blue guide line [33].

As bulk oxygen vacancy ($V_{o\ bulk}$) is linked with the green-yellow luminescence of ZnO, Li et al. first extended such a correlation to the surface oxygen vacancy ($V_{o\ surface}$) concentration on polar ZnO facets monitored by using PL spectroscopy [20]. They compared the facet catalytic activity of ZnO rods, disks, rings, and screw caps **(Figure 1-8a)** with their corresponding PL spectra **(Figure 1-8b)** and found a positive correlation between the PL intensity and the proportion of exposed (002) facet in the order of screw caps > disks > rings > rods. Moreover, as the green emission (~520 nm)

has been reported a good correlation with the $V_{o\ bulk}$ and the yellow emission (~620 nm) could be assigned to the interstitial oxygen, the PL broadband was further divided into two bands in the green and the yellow range **(Figure 1-8c)**. The intensity of the green emission clearly varies with different ZnO morphologies, following the same order as the broadband intensity: screw caps > disks > rings > rods [20]. Also, it is widely accepted that the $V_{o\ surface}$ can act as potential wells to trap either one or two electrons, aiding electron-hole pair separation and thus increasing the photocatalytic activity. Since then, PL has become widely used as one of the major characterizaion techniques to evaluate the $V_{o\ surface}$ concentration of ZnO NPs in photocatalysis [20, 27-30] or optical/electronics [31,32].

Recently, the preferential distribution of $V_{o\ surface}$ on the polar (002) facet of ZnO nanowire (NW) **(Figure 1-8d)** (cf. nonpolar (100) facet) was further demonstrated by Wong et al. using room-temperature confocal microscopy [33]. **Figure 1-8e** shows the confocal PL emission intensity of an individual ZnO NW lying on a side composed of the (100) facet surface and corresponding PL spectra at three different spatial locations (I_1 to I_3) along the [0001] direction. The shape and location of the PL peaks remain unchanged and only the peak intensity increases ($I_1 > I_2 > I_3$) with its location close to the tip of NW (i.e. where polar (002) facet is exposed). Also, **Figure 1-8f** shows the confocal PL spectra at six different spatial locations indicated by the blue line in the top cross-sectional (002) plane of the NWs. The intensity of the green luminescence peak was found strongest at top edge (i.e. d_6 and d_1) where the (002) and (100) surfaces meet each other [33]. Accordingly, their results qualitatively demonstrate the $V_{o\ surface}$ is populated on (002) facet (cf. (100) facet) especially at the interface between (002) and (100) facets.

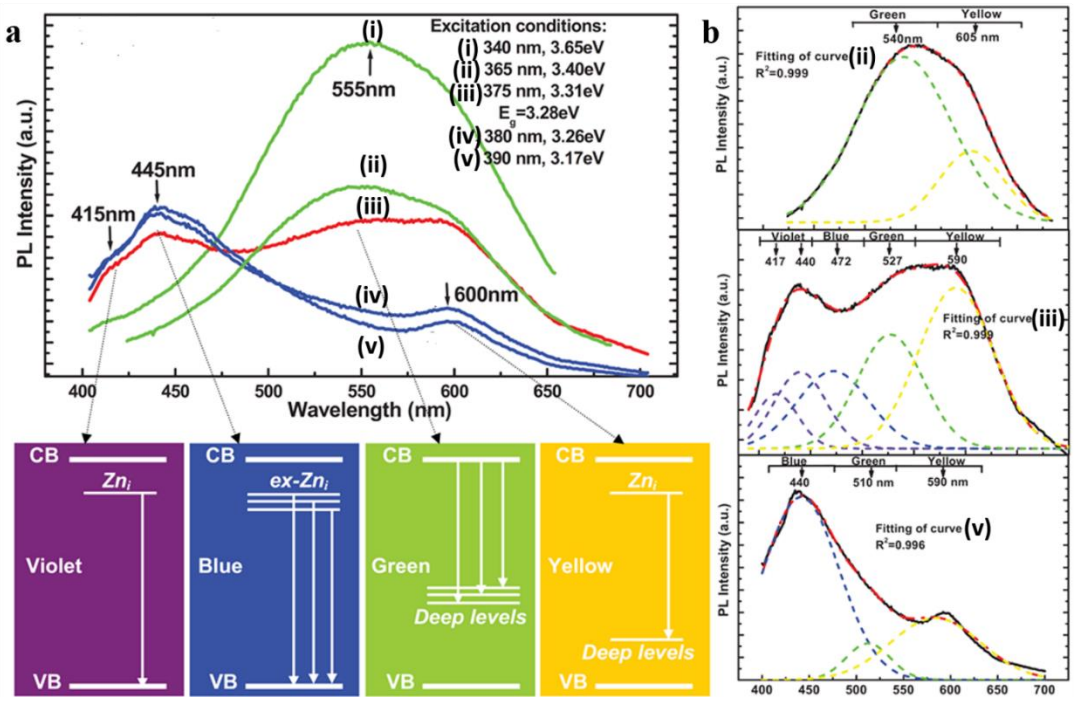

Figure 1-9. (a) PL spectra of ZnO nanoparticle (E_g = 3.28 eV) with various excitation wavelength from (i) 3.65 eV to (v) 3.17 eV. The proposed mechanisms are denoted for violet, blue, green, and yellow emissions, respectively [32]. (b) Spectra deconvolution of (ii), (iii) and (v) based on the proposed mechanism [32].

However, as stated above, PL is not a surface-specific technique and thus fails to deliver precise $V_{o\ surface}$ with interferences from bulk defects (e.g. Zn interstitial). Moreover, as shown by Zeng et al., the PL pattern was found highly dependent on excitation wavelength used no matter the excitation energy is larger (i.e. (i) to (iii)) or smaller (i.e. (iv) and (v)) than the bandgap **(Figure 1-9a)**. Generally, the broad peak with subpeaks at a longer wavelength than the corresponding band gap is because of the various emissions from the defect levels between the bands [32]. According to Zeng et al., the violet (~415 nm) and blue (~445 nm) emissions in **Figure 1-9a** are attributed to the transitions from Zn interstitial-related defects (Zn_i) and extended Zn_i (ex-Zn_i) located slightly below the conduction band edge to the valance band, respectively [32]. Furthermore, the green (~530 nm) and yellow (~600 nm) regions represent the transitions from the conduction band and Zn_i to deep levels ($V_{o\ bulk}$ of ~1 eV above the

valance band), respectively **(Figure 1-9a)**. The Gaussian fitting in **Figure 1-9b** clearly shows that even though curve (ii) and curve (iii) were obtained with the excitation energy larger than the bandgap, both the intensity and position of green emission varies with excitation energy. With the excitation energy decreasing, the green emission weakens but a new emission in violet-blue region emerges and increases. When the excitation energy is near the bandgap (i.e. curve (iii)), a very broad emission can be obtained in which the violet-blue and green emissions have comparable intensity. As the excitation energy decreases below the bandgap (i.e. curve (v)), most of the green emission is quenched except for a weak shoulder at 600 nm. As a result, the spectra are then dominated by the violet-blue emission.

Due to this excitation-dependent property and the interferences from bulk defects especially Zn_i, a single PL determination is therefore not enough to provide concrete reliable correlation between $V_{o\ surface}$ and photocatalytic performance [34]. Often, the comparison of such green emission from $V_{o\ surface}$ is limited to individual studies, as the processing and post-treatment techniques used in the preparation of ZnO NPs vary from group to group [35]. This results in many differences between nanoparticles, in addition to the exposed facet, such as the concentration of bulk defects and the particle size (may affect scattering). Cross-literature comparison of catalysts performance is thus seriously hindered as there is currently no universal technique which can provide quantitative analysis of the concentration/distribution of $V_{o\ surface}$ and the percentage of the desired facet on a given catalyst.

1.4.2. Using EPR as a main facet-characterization technique

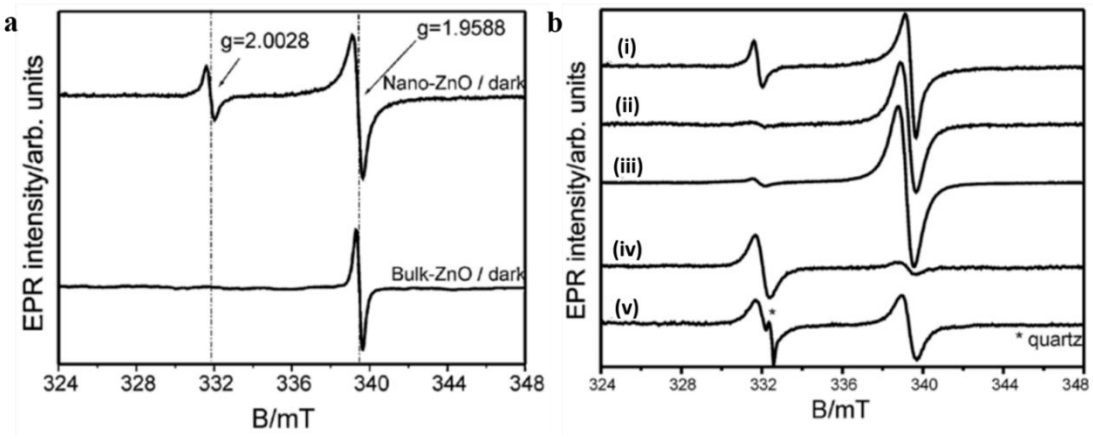

Figure 1-10. (a) X-Band EPR spectra of bulk- and nano-sized ZnO particles [39]. (b) X-Band EPR spectra of nano-sized ZnO as treated in the following sequence: (i) initial, (ii) after exposure to air (adsorption of water molecules), (iii) after irradiation with UV light, (iv) after 5 min heating at 150°C, (v) after UV irradiation. The signal designated by an asterisk (*) is owing to a signal from the EPR quartz tube [39].

EPR spectroscopy is another technique that is widely employed to evaluate the $V_{o\ surface}$ of ZnO NPs through the monitor of the transition of unpaired electron spins [27,28,32,36-41]. As shown in **Figure 1-10a**, both bulk and nano-sized ZnO reveal an intense signal at approximately g=1.96. Its origin is attributed to the unpaired electrons trapped by shallow donors or impurities [39-41]. For nano-sized ZnO, an additional resonance line at approximately g=2.00 is assigned to the unpaired electrons trapped in $V_{o\ surface}$ by adsorbed dioxygen (O_2^-) or other low-coordinate surface defect sites [39-41]. In general, these results are referenced to the bulk-surface (core-shell) model of ZnO that the concentration ratio between core and shell (surface-to-volume ratio) is defined for a given particle size. Accordingly, these two observed unpaired electron spins of the nano-sized ZnO can be realized that the signal at g=1.96 is due to the bulk (core) contribution and the one at g=2.00 originates from the surface (shell) [39]. As a quantitative value [spin counts*g^{-1} of sample] can be obtained by the integration of an EPR signal (i.e. the concentration of trapped unpaired electron), the cross-comparison

of $V_{o\ surface}$ concentration between literatures is thus feasible. On the other hand, the surface EPR signal at g=2.00 was also found strongly dependent upon humidity. As shown in **Figure 1-10b(ii)**, this signal almost disappears while the signal intensity of the bulk signal (i.e. g=1.96) remains unaffected. Comparing to the tiny increase of g=2.00 by UV illumination **(Figure 1-10b(iii))**, a considerable increase of g=2.00 was observed after later thermal treatment at the expense of g=1.96 **(Figure 10b(iv))** due to desorption of water molecule. The intensity of g=1.96 can be increased again after a second illumination with UV light of the heat-treated sample **(Figure 1-10b(v))** [39].

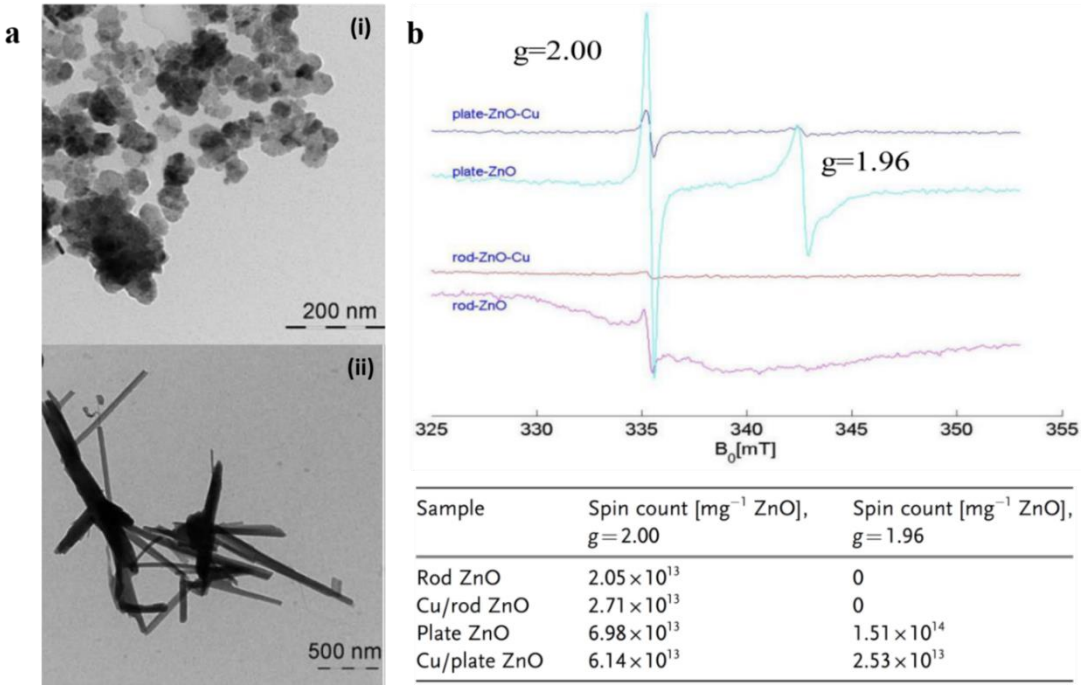

Sample	Spin count [mg^{-1} ZnO], $g=2.00$	Spin count [mg^{-1} ZnO], $g=1.96$
Rod ZnO	2.05×10^{13}	0
Cu/rod ZnO	2.71×10^{13}	0
Plate ZnO	6.98×10^{13}	1.51×10^{14}
Cu/plate ZnO	6.14×10^{13}	2.53×10^{13}

Figure 1-11. (a) TEM images of ZnO (i) nanoplate and (ii) nanorods. (b) EPR spectra of ZnO nanoparticles (plate, rod and their mixtures with copper) and corresponding quantitative table of peaks at g=2.00 and g=1.96 [40].

Similar to the PL observation, a correlation between the intensity of EPR g value at 2 (i.e. $V_{o\ surface}$ concentration) and polar ZnO facets was firstly illustrated by Liao et al [40]. They compared the EPR signals of plate-shape **(Figure 1-11a(i))** and rod-shape **(Figure 1-11a(ii))** ZnO NPs with preferential exposed polar (002) and nonpolar (100)

facets and found a positive correlation of exposed (002) facet and the intensity of g=2.00 in the order of nanoplate ($6.98*10^{13}$ spins/mg) > nanorod ($2.05*10^{13}$ spins/mg) **(Figure 1-11b)**. They also presented the significance of polar ZnO (002) facet on its electronic interaction with copper in the synthesis of methanol from carbon dioxide hydrogenation. The electron transfer from the conduction band of ZnO nanoplate to copper is evident from the decrease of both signal at g=2.00 and g=1.96 after the addition of copper **(Figure 1-11b)** [40]. As illustrated above, this EPR technique seems promising and much precise than previous PL technique since no interference from bulk species and a quantitative result of $V_{o\ surface}$ concentration makes cross-literature comparison feasible.

However, according to Walters et al.'s experiment, the signal at g=2.00 cannot represent the true $V_{o\ surface}$ concentration as only O_2 adsorbed $V_{o\ surface}$ with one ($(V_{o\ surface}^{+})^{-}$) or two ($(V_{o\ surface})^{2-}$) electrons contributes to this signal and no overall signal for $V_{o\ surface}$ with no electron left in its ionic form ($V_{o\ surface}^{2+}$) [36-38]. Also, if we consider the equation $O_2 + V_{o\ surface} + e^{-} \leftrightarrow O_2^{-}(V_{o\ surface})$, not all $(V_{o\ surface}^{+})^{-}$ and $(V_{o\ surface})^{2-}$ sites could take up O_2 due to the equilibrium involved [36-38]. Also, Carter et al. showed that the $O_2^{-}(V_{o\ surface})$ species were the only species exhibiting photochemical reactivity as compared to the other EPR active adsorbed species at surface non-vacancy sites [42,43]. Accordingly, EPR is thus a semi-quantitative technique for $V_{o\ surface}$ and no knowledge of facets and other surface features are actually provided. As PL and EPR are a not truly facet-specific techniques, studies bridging the active facet and catalytic result may sometimes lead to disagreements as no information available on the distribution of surface features (e.g. V_o here) among facets [34].

In addition to PL and EPR, the use of basic probe molecules to assist characterization of material surface such as temperature-programmed desorption (TPD) of ammonia [44] and Fourier-transform infrared spectroscopy (FTIR) of pyridine [45,46] have been attempted for qualitative or semi-quantitative determination of acid properties on the outmost surface of metal oxides. However, still, no information available on the distribution of surface features among facets is available. A universal technique that can provide cross-literature comparison on the distribution/concentration of surface features among various facets is therefore highly desirable. As such, a comprehensive understanding of these acidic properties is crucial for the design, modification and applications of solid acid catalysts.

1.5. Facet-dependent photocatalysis of anatase TiO_2 NPs and characterization

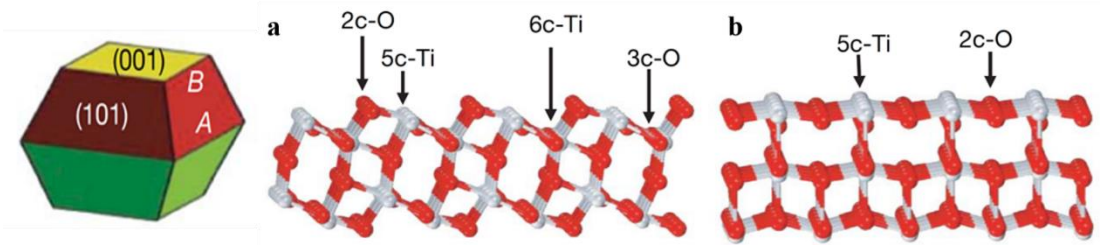

Figure 1-12. Schematic illustration of the truncated octahedral bipyramidal anatase TiO_2 crystal and the two main crystallographic exposed planes (a) (101) and (b) (001). The side lengths labeled A and B are used to define the degree of truncation (B/A) and to estimate the percentage of (001) facets [52].

Titanium dioxide (TiO_2) has been the most intensively investigated binary transition metal oxide due to the wide range of its applications for environmental and energy-related areas, especially for (photo)catalysis, dye-sensitized solar cells (DSSCs), lithium ion batteries, sensors, catalyst supports etc. The unique physical and chemical properties of TiO_2 crystals are affected not only by the intrinsic electronic structure, but also by their size, shape and surface properties [3]. In particular, some physicochemical properties such as molecular adsorption, catalytic reactivity and selectivity depend largely on the surface atomic configuration and the percentage of exposed facets. Accordingly, tailoring TiO_2 crystals exposed with specific facets have been the hottest research topic since the past decades [47-50]. The truncated octahedral bipyramid anatase TiO_2 crystal with eight (101) facets and two (001) facets **(Figure 1-12)** is the most common shape observed in nature. According to Wulff construction, the degree of truncation (B/A) in nature is in the order of 0.3 ~ 0.4, giving less than 10% of the exposed (001) facets [51]. Even though various preparations have been attempted, most synthetic anatase TiO_2 crystals are mostly covered with thermodynamically more stable (101) facets due to its lower surface free energy (0.44 J/m^2) rather than the reactive

high-energy (001) facets (0.90 J/m^2) [51].

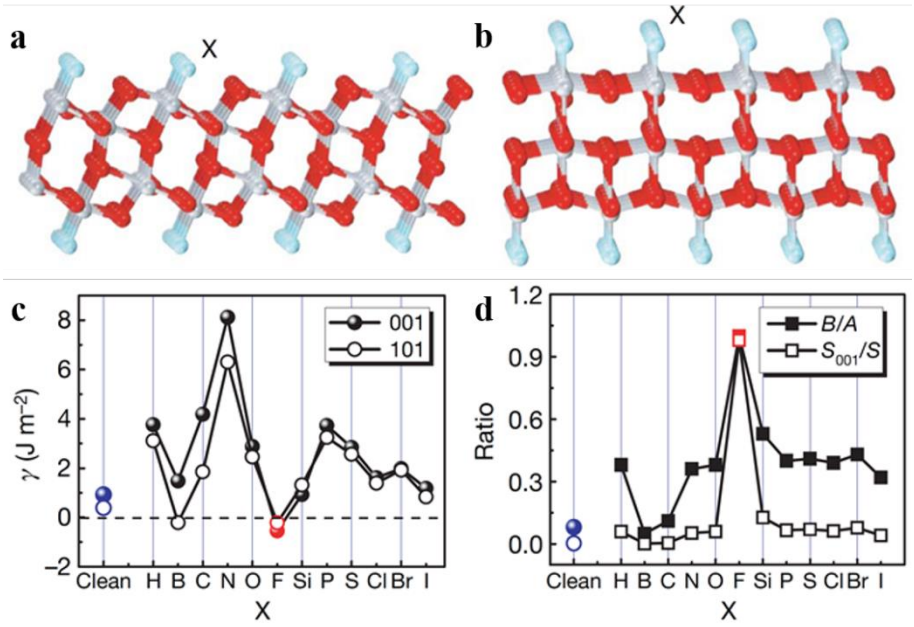

Figure 1-13. Unrelaxed (a) (101) and (b) (001) surfaces surrounded by adsorbate X atoms. (c) Calculated energies of the (001) and (101) surfaces surrounded by X atoms. (d) Plots of the optimized value of B/A and percentage of (001) facets for anatase single crystals with various adsorbate atoms X [52].

To synthesize anatase TiO_2 crystals with dominant high energy (001) facets, the crystal growth should to be confined within the kinetically controlled regime under nonequilibrium conditions. Yang et al. theoretically investigated the effects of 12 nonmetallic atoms (X) as SDS (X = H, B, C, N, O, F, Si, P, S, Cl, Br, or I) on changing the surface energies of anatase (001) and (101) surfaces [52]. As shown in **Figure 1-13a-d**, the adsorption of F reverses the relative order of surface energy and thus the stability of (101) and (001) surfaces, compared to the clean ones. As the growth rate of a crystal facet depends on the surface energy (high-energy facets grow more quickly than low energy facets), this indicates that the formation of F-stabilized (001) facet is now preferable during particle preparation **(Figure 1-13d)**. This prediction has been validated firstly by Yang et al. in their synthesis of micro-sized anatase TiO_2 with 47% (001) facet with the addition of HF during hydrothermal preparation **(Figure 1-14a)**

[52]. Later, Han et al. successfully prepared nano-sized anatase crystal with almost doubled the coverage of (001) facets (up to 89%) by using tetrabutyl titanate, $Ti(OBu)_4$, instead of titanium tetrafluoride (TiF_4) as precursor **(Figure 1-14b)** [53]. Since then, using fluoride as SDS to obtain TiO_2 nanocrystals with different percentage of exposed (001) facet (by tuning HF concentration) **(Figure 1-14c)** for the investigation of facet activity has been well-documented [47-50] in photocatalysis [53-66], methanol conversion [67], solar cell [68-71] and lithium battery [72,73].

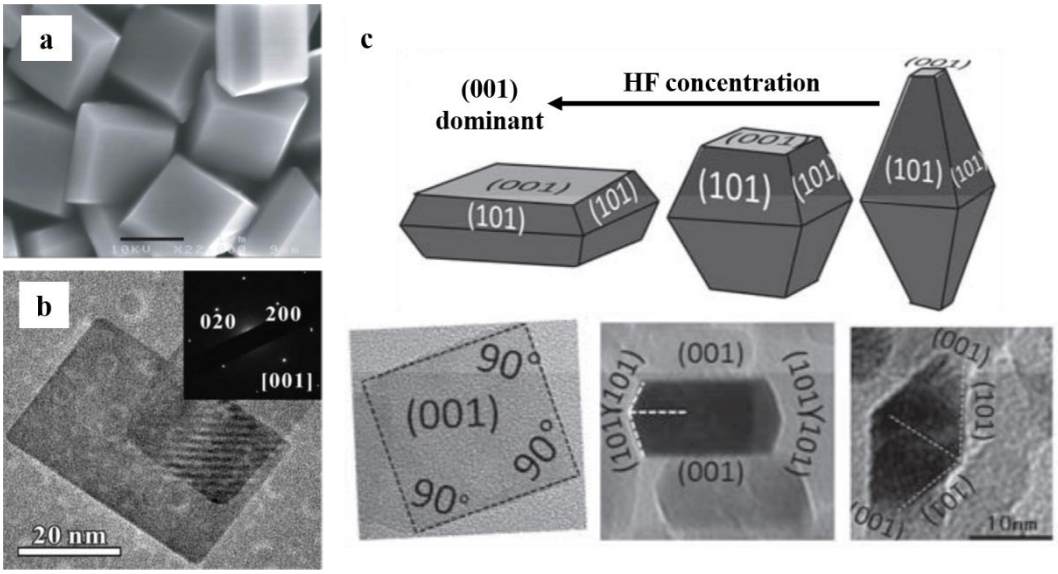

Figure 1-14. (a) SEM image of anatase TiO_2 microsheets with 47% (001) facet (scale bar: 1 μm) [52]. (b) TEM image of anatase TiO_2 nanosheet with 89% (001) facet [53]. (c) Schematic of the correlation between HF concentration and corresponding products with different percentages of exposed (001) facets [69].

In general, the removal of SDS (e.g. fluorine in this case) after the shape control of particle is required to avoid its interfering to the interested properties on facet activity. Particularly, in the field of heterogeneous catalysis involving the bonds breakage and formation at the catalyst surface is closely associated with the coordination environment of the surface active atoms. From the literature, the surface attached F (i.e. F-Ti) can be removed by a simple post-treatment via either calcination at 600 ° C [52,54-56,59,61,63,66-71] or ion exchange with aqueous NaOH [53,55,57-59,64,65] to obtain

a so-called “clean surface”. However, by adopting different removal methods, diverse results have been obtained in literature in various applications which create different interpretations and frequently disagreements amongst researchers [53-73]. Here, we summarize corresponding photocatalysis cases in **Table 1-1**.

Metal oxide	Crystal phase	Post-treatment	Photocatalytic reaction	Activity	Proposed mechanism	Ref.
TiO_2	Anatase	NaOH wash	Degradation of MO	Na-(001) > F-(001)	Density of unsaturated Ti	53
TiO_2	Anatase	Calcination	Hydroxyl radical production	Cal-(001) > F-(001)	Density of unsaturated Ti	54
TiO_2	Anatase	NaOH wash/ Calcination	Degradation of MO & MB	MO: F-(001) > Na-(001) ~ Cal-(001) MB: Na-(001) > Cal-(001) > F-(001)	Selective dye adsorption	55
TiO_2	Anatase	Calcination	Hydroxyl radical production /H_2 evolution from water	Cal-(010) > Cal-(101) > Cal-(001) > F-(010) ~ F-(101) ~ F-(001)	Density of unsaturated Ti /Band structures	56
TiO_2	Anatase	NaOH wash	H_2 evolution from water	Na-(101) > F-(101) > F-(001) > Na-(001)	Density of unsaturated Ti	57
TiO_2	Anatase	NaOH wash	H_2 evolution from water	F-(001) > Na-(001) ~ TiO_2	Enhanced charge separation (ECS) by residual fluorine	58
TiO_2	Anatase	NaOH wash/ Calcination	Degradation of acetone	F-TiO_2 > Cal-TiO_2 ~ Na-TiO_2	Synergetic effect of (001) & (101) facets & ECS	59
TiO_2	Anatase	-	Degradation of acetaldehyde	F-TiO_2 > TiO_2	Concentration of surface hydroxyl group	60
TiO_2	Anatase	Calcination	CO_2-reduction	(001): oxidation (101): reduction	Synergetic effect of (001) & (101) facets	61
TiO_2	Anatase	NaOH & HF wash	Degradation of MB	HF-Na-TiO_2 > Na-TiO_2 > TiO_2	Synergetic effect of two facets & surface defects	64
TiO_2	Anatase	NaOH wash	Degradation of acetaldehyde and phenol	Increases with surface fluorine concentration	Enhanced adsorbed oxygen by residual fluorine	65
TiO_2	Anatase	Calcination	Degradation of MB	Increases with (001) facet for particle with the same size	Density of unsaturated Ti	66

Table 1-1. Facet-controlled F-capped TiO_2 NPs treated with various post-treatments (Na: NaOH wash; Cal: calcination) and their corresponding activities/mechanisms. F-(001) represents as-prepared F-stabilized TiO_2 NP with preferential exposed (001) facet; Na/Cal-(001) represents F-(001) post-treated with NaOH wash/calcination for the removal of surface fluorine.

Notice that all cases in **Table 1-1** are the anatase TiO_2 NPs prepared using fluorine as SDS for the morphology control. Accordingly, the NaOH treated (001) facet (i.e. Na-(001)) showed higher activity in the photocatalytic degradation of methyl orange (MO) dye than the F-capped (001) facet (i.e. F-(001)) [53], while an opposite result was obtained for the same reaction by the other research group [55] **(Table 1-1)**. Moreover, the environment to carry out photocatalysis seems to play a key factor. The treated TiO_2

(i.e. Cal-TiO_2 and Na-TiO_2) gives higher photodegradation activity than F-stabilized TiO_2 toward methyl orange (MO) [53] and methylene blue (MB) [55] in aqueous, while F-stabilized TiO_2 shows higher activity for the degradation of acetone [59] and acetaldehyde [60] in air **(Table 1-1)**. On the other hand, both NaOH and calcination treatment were reported to increase the facet activity of (101) in photocatalytic hydrogen evolution [56,57], while the NaOH treatment was concluded to lower the facet activity of (001) in this reaction by others **(Table 1-1)** [57,58].

It is widely-accepted that any adsorbed molecule on TiO_2 surface can efficiently modulate the surface Ti chemical state, which can deviate largely from that of clean surface. For example, the attachment of PO_4^{3-}/SO_4^{2-} on the TiO_2 surface has been reported to provide extra BA sites and at the same time to increase Lewis acidity (i.e. decrease electron density of surrounding Ti atoms) [74-77]. Also, the chelating of surface COOH-containing dye [78] and electrolyte additive such as 4-*t*-butylpyridine (TBP) [79] have been found to remarkably improve the solar cell performance due to the shift of Ti d-band edge toward negative potentials by adsorption onto the TiO_2 surface. On the other hand, the surface reconstruction of (001) from unstable (1 × 1) to (1 × 4) upon F removal during calcination has been shown to result in significantly different Ti chemical state [80]. Accordingly, those different interpretations made amongst researchers in **Table 1-1** may be arisen from the trace of residue SDS (e.g. F or OH) remained on surface [64,65,80] or surface reconstruction of unstable (001) upon its removal during calcination [81-83], both of each affecting the chemical state of exposed titanium. So far, no proper surface tool can characterize the surface Ti chemical state on either reconstructed facet or facet promoted with various adsorbed molecules for the correlation of facet activities.

1.5.1. Characterization tools employed to correlate facet photoactivity

Metal oxide	TEM/SEM	XPS	Raman	EPR	UV-Vis	AES	NMR	Ref. #
Anatase TiO_2	✓	✓						52
Anatase TiO_2	✓							53
Anatase TiO_2	✓	✓						54
Anatase TiO_2	✓	✓						55
Anatase TiO_2	✓	✓	✓		✓			56
Anatase TiO_2	✓	✓		✓				57
Anatase TiO_2	✓	✓			✓			58
Anatase TiO_2	✓	✓						59
Anatase TiO_2	✓	✓						60
Anatase TiO_2	✓	✓			✓			63
Anatase TiO_2	✓	✓		✓				64
Anatase TiO_2	✓	✓			✓			65
Anatase TiO_2	✓	✓			✓			66
Anatase TiO_2	✓	✓	✓	✓	✓	✓	✓	80

Table 1-2. Summary of techniques used for anatase TiO_2 NPs characterization. Notice that references selected in this table all use F as SDS for their morphology controls (S/TEM: scanning/transmission electron microscopy; XPS: X-ray photoelectron spectroscopy; EPR: electron paramagnetic resonance; UV-Vis: ultraviolet−visible spectroscopy; AES: Auger electron spectroscopy; NMR: nuclear magnetic resonance).

The tools nowadays employed in the characterization of surfaces with respect to TiO_2 facet-dependent photoactivity are summarized in **Table 1-2**. Notice that from this table we only select references using F as SDS for TiO_2 morphology control since the surface properties (e.g. the chemical state of cations) can vary with different SDS. As shown in the **Table 1-2**, the TEM and SEM are the most adopted techniques to identify the preferential exposed facet of a TiO_2 nanocrystal. To further monitor element(s) and their oxidation state(s) on material surface, X-ray photoelectron spectroscopy (XPS) analysis is also carried out. As shown in **Figure 1-15a**, as the used HF concentration rises, the F_{1S} intensity of TiO_2 samples increases, while no apparent chemical shift and change of intensity were observed for both Ti_{2P} **(Figure 1-15b)** and O_{1S} **(Figure 1-15c)** [65].

Similar results were also reported, the removal of fluorine by either calcination or NaOH wash can be evaluated by the intensity of XPS F_{1S} signal **(Figure 1-15d)**, while no observed chemical shift and change of intensity for Ti_{2P} **(Figure 1-15e)** [80]. This might be due to the long electron escaping depth with more than outmost atomic layer (few atoms depth) from sample, which renders the XPS not a truly surface technique (detection limit ~ 0.1% atom). Even though Auger electron spectroscopy (AES) is known to provide higher spatial resolution as the energy of ejected Auger electrons is much sensitive to chemical environment compared to the core-level signals in XPS, no peak shift of Ti_{2P} in the presence of fluorine was observed for five Ti LMM Auger signals (marked by dashed blue line) **(Figure 1-15f)** [80]. This indicates the change of chemical state of the outmost Ti atom is still averaged out during the collection of Auger electrons from the electron escaping depth.

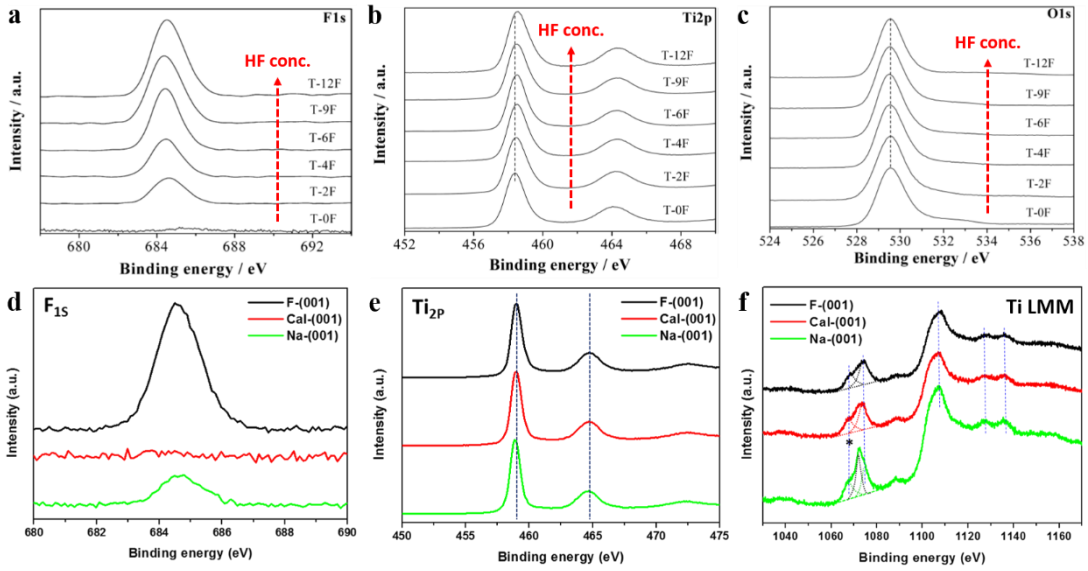

Figure 1-15. a-c) XPS spectra of (a) F_{1S}, (b) Ti_{2P} and (c) O_{1S} of F-stabilized TiO_2 samples prepared with 0 to 1.2 mL of 40% HF [65]. d-f) XPS spectra of (d) F_{1S}, (e) Ti_{2P} and (f) Ti LMM (Auger spectra) of F-stabilized (001) TiO_2 samples with different post-treatments (Cal: calcination and Na: NaOH wash). The peak marked with asterisk "*" in figure (f) is Na_{1S} signal [80].

According to the literature [56,84,85], the removal of surface fluorine can also be monitored by Raman spectroscopy. It has been shown that the surface attached fluorine changes both symmetry of Ti-O-Ti and coordination of surface Ti atom, resulting in the shift of low-frequency E_g and weakening of B_{1g} (cf. A_{1g}) after the fluorine removal **(Figure 1-16a)** [84]. The EPR signal at g ~ 2.0 (unpaired electrons trapped in V_o via adsorbed oxygen species from air (O_2^-)) and g ~ 1.98 (unpaired electrons trapped by surface/subsurface paramagnetic Ti^{3+} center) have been used to evaluate the effect of F attachment, NaOH washing and subsequently HF treatment to the surface **(Figure 1-16b)** [64]. EPR was also adopted by D'Arienzo et al. to investigate the relative contribution of each exposed crystal facets to the photoactivity [62]. The (001) surface was found playing the major role in the photocatalytic process by providing oxidation sites, while the (101) surface was involved as supplier of reductive sites. This synergetic effect of different facets has been shown effectively reduce the electron-hole recombination and further enhance their photocatalytic activity [59,61,63,64]. Pan et al. attributed the photocatalytic performance of facet-controlled TiO_2 to the band gap size of the exposed facets determined by ultraviolet−visible (UV−vis) spectra together with valence band XPS measurement (T010 > T101 > T001) **(Figure 1-16c)** [56]. However, the influence of the particle size on band gap of semiconductor was neglected in their work. To demonstrate this, Wu et al. prepared anatase TiO_2 single crystals with different percentage of (001) facets in uniform size, as well as anatase TiO_2 single crystals with different particles size in same percentage of (001) facets [66]. Their results showed the band gap of anatase TiO_2 crystals is nearly independent with the percentage of different reactive facets, while the band gap will be much narrower with smaller particles size. Therefore, the higher photoreactivity of (101) facet than that of (001) facets in Pan's work [56] could be associated with the much smaller particle size of the sample with high percentage of (101) facets.

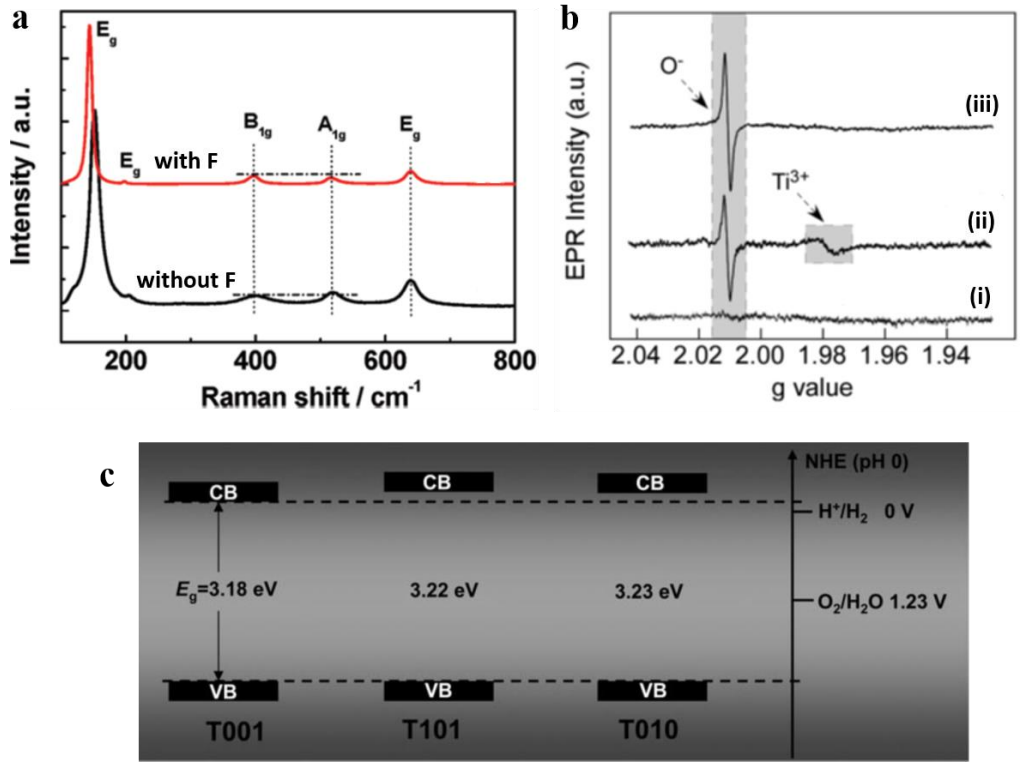

Figure 1-16. (a) Raman spectra of anatase TiO_2 sheets with/without surface F [84]. (b) EPR spectra of (i) as-synthesized F-stabilized TiO_2, (ii) after NaOH wash and subsequently (iii) HF treatment [64]. (c) The determined band-gap size of anatase TiO_2 crystals with preferential exposed (001), (101) and (010) facets [56].

In addition to band structure, the commonly used criteria to explain the photoactivity of TiO_2 facets is the density of surface undercoordinated atoms **(Table 1-1)** [53,54,56,57,66]. Those literatures have assumed they obtained clean surface after F removal and attributed the high photoactivity of (001) facet to the 100% surface unsaturated Ti_{5C} atoms on (001) facets (cf. 50% for the (101) facets) **(Figure 1-12)**. However, as shown above, these surface tools are used mainly for the proof of F removal (i.e. XPS, Raman, and EPR) or electronic structure (i.e. UV-vis and XPS), they are not truly facet specifics. Accordingly, they provide very limited information on the chemical state of surface features (V_o, OH, cations…etc.) and their distribution among facets, causing difficulty to unambiguously correlate facet-dependent results during the past decades.

1.5.2. Treatment-dependent surface features

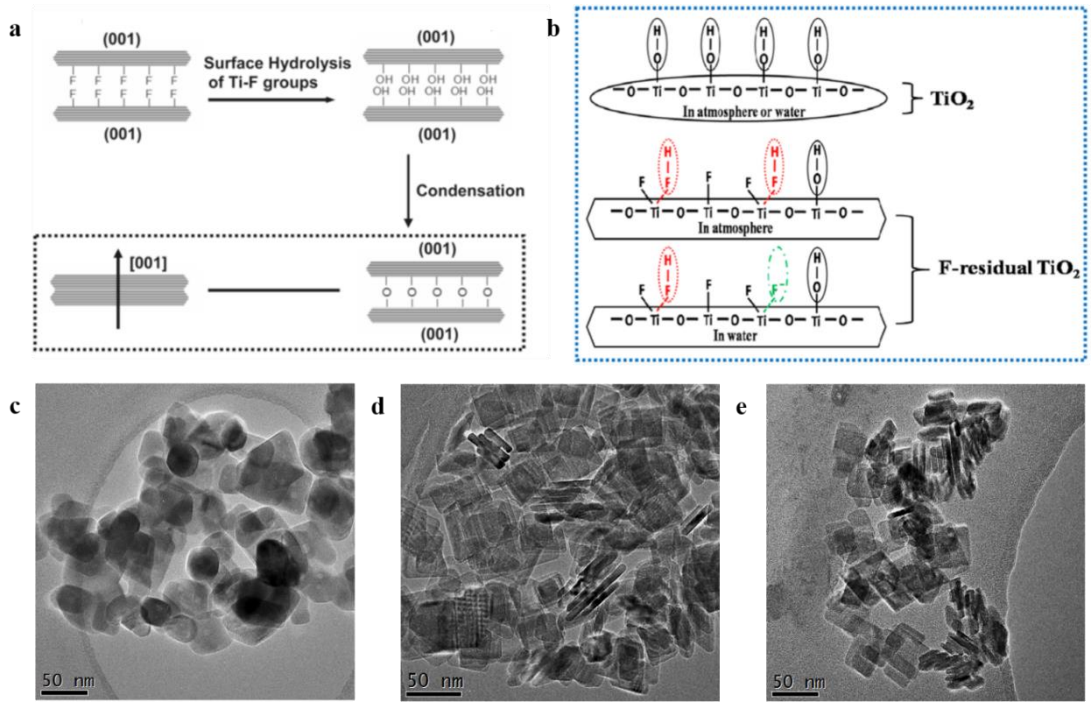

Figure 1-17. (a) Schematic illustration of the stacked anatase TiO_2 nanosheets (aggregation) by calcination treatment [86]. (b) Surface features schematic of TiO_2 and TiO_2 with F residues in atmosphere/water [65]. c-e) TEM images of (c) calcined, (d) NaOH washed and (e) as-prepared TiO_2 nanosheets [80].

In addition to the limitation from technical aspects mentioned above, different post-treatments adopted during the particle preparation (e.g. calcination at 600°C in air/0.1M NaOH wash here) further increase the difficulty in surface characterization. Given that each facet possesses distinctive intrinsic energy, it is understandable that both concentration and chemical state of surface features differ from facet to facet after reaching equilibrium with post-treatments. Recently, the calcination removal of fluorine has been shown to cause stacked TiO_2 nanosheets along particle [001] crystallographic direction, driven by the minimization of surface energy [86,87]. The surface Ti-F groups can be totally hydrolysed by water during calcination in air at high temperature (600°C, endothermic reaction) **(Figure 1-17a)**. In this case, the exposed surfaces of sheet-like anatase TiO_2 are also mainly covered by -OH groups. As (001)

facet has a higher surface energy than (101) facet, the (001) interfaces between adjacent nanosheets would be eliminated through the condensation of Ti-OH groups (formation of Ti-O-Ti linkages) at high temperature and therefore the (101) facet becomes dominant **(Figure 1-17a)**. Also, (001) facet has been recently shown to reconstruct from (1 x 1) to a more stable (1 x 4) surface at high temperature by environmental TEM [82] and in situ STEM [83]. Accordingly, the formation of surface Ti-OH, elimination of (001) facet and reconstruction of the rest (001) facet should be also included for activity consideration by study using calcination as post-treatment. Comparing to calcine-induced aggregation **(Figure 1-17c)**, no apparent morphology change can be observed for NaOH wash at room temperature **(Figure 1-17d)** (cf. F-stabilized TiO_2, **Figure 1-17e**). However, the NaOH wash has been reported to induce changes in the surface morphology, including step density and point defects [64]. Such changes might have an influence on the photoactivity after the NaOH wash. Also, in some cases, the F removal was not complete by NaOH wash (from XPS F_{1S}) [64,65,80] presumably due to ambient reaction temperature, while no F found in all calcined samples (from XPS F_{1S}) [52,54-56,59,63,66-71]. The surface F residue (i.e. Ti-F group) has been shown to act as an electron-trapping site but to reduce interfacial electron transfer rates by tightly holding trapped electrons due to the strong electronegativity of the fluorine [88]. Also, different forms of residue F on TiO_2 surface have been found at ambient and water. As shown by Luan et al., the surface of F-residual TiO_2 possesses −Ti−OH, −Ti−F and −Ti:F−H groups in the air, while −Ti:F− has been found from the dissociation of the −Ti:F−H group in water **(Figure 1-17b)** [65]. They suggest that the −Ti:F−H could greatly enhance O_2 adsorption and thus greatly promote the charge separation and the photocatalytic activity. This finding may explain some controversies in reported literature as different post-treatments (calcination/NaOH wash) and reaction phases (ambient/water) would lead to various −Ti:F−H concentration.

1.6. Probe-assisted NMR as a potential surface technique

Technique	Mechanism	Feature info.	Signal from…
PL	excited electrons trapped by defects	defect	surface/bulk
EPR	unpaired electrons trapped by defects	surface/bulk defect	outmost surface/bulk
XPS	escaping electron from nucleus	surface composition/oxidation state	surface 2~10 atomic layers
NH_3-TPD	adsorption strength of NH_3	Brönsted/Lewis acid site	outmost surface
Pyridine-IR	vibration frequency of pyridine		

Table 1-3. Summary of techniques used for surface feature characterization (TPD: temperature program desorption; IR: infrared spectroscopy).

As discussed and shown above, current techniques used for surface feature characterization have their shortcomings **(Table 1-3)**. PL fails to deliver precise $V_{o\ surface}$ with interferences from bulk defects as both defects give green emission at around 530 nm. While EPR can not only quantify V_o concentration but also distinguish its location between bulk (g=1.9x) and outmost surface (g=2.00) as the unpaired electrons trapped in $V_{o\ surface}$ can be uptake by adsorbed dioxygen (O_2^-). However, no information on other features of outmost surface (e.g. metal cation and hydroxyl group) and their corresponding chemical states can be provided. XPS analysis is a commonly carried out to monitor element(s) and their oxidation state(s) on material surface. However, the long electron escaping depth (usually 2~10 atomic layers) from sample by XPS render it not an ideal technique for the characterization of outmost surface with interference from 2~10 atomic layers below the surface. Since metal ion sites exposed with the introduction of surface by $V_{o\ surface}$ can function as Lewis acid (LA) sites, the use of basic probe molecules to assist characterization of material outmost surface such as temperature-programmed desorption (TPD) of ammonia [44,45] is feasible. Fourier-transform infrared spectroscopy (FTIR) of pyridine [45] is another technique that can employ for qualitative or semi-quantitative determination of acid properties on the outmost surface of metal oxides. However, the probe molecules used in these cases are too basic to distinguish subtle differences between $V_{o\ surface}$ and other Lewis acid sites

in their strength and distribution, leading to simple profiles of an averaged acid strength. Alternatively, probe-assisted nuclear magnetic resonance (NMR) has recently shown its potential in differentiating various micro-environments by corresponding chemical shift. Among NMR-active basic probes (e.g. ^{13}carbon monooxide for ^{13}C, pyridine for ^{15}N, trimethylphosphine (TMP) for ^{31}P…etc.), ^{31}P nucleus with 100% natural abundance and a chemical shift (δ^{31}P) range over 430 ppm has thus preferentially adopted as a potential candidate.

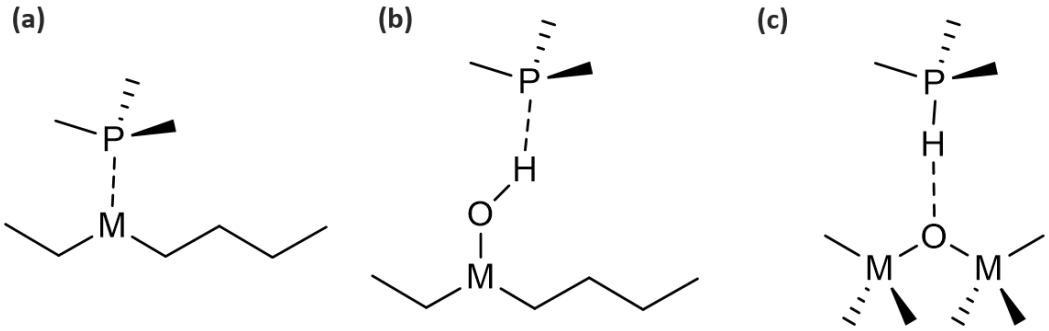

Figure 1-18. Interaction between TMP and metal oxide. TMP molecule interacts (a) with metal cation; (b) with hydroxyl proton (hydrogen bonding interaction); (c) on bridging hydroxyl proton (Brønsted acid, BA) site, the formation of $TMPH^+$ complex).[46]

Pioneered by Lunsford and co-workers, TMP was first adopted as a probe molecule to characterize the acidity of zeolite based on the observed ^{31}P chemical shift (δ^{31}P) [89]. This TMP-assisted probing technique has been shown a sensitive and reliable technique capable of providing qualitative information (the type (Lewis acid, LA or Brønsted acid, BA) and strength of acid sites) and quantitative information (concentration of each site) in various solid acid catalysts such as microporous zeolites, mesoporous molecular sieves, supported/sulfated metal oxide catalyst [46]. **Figure 1-18** shows three scenarios of interactions between TMP and metal oxide: (a) with metal cation LA center; (b) with hydroxyl proton LA center (hydrogen bonding interaction); (c) on bridging hydroxyl

proton (Brønsted acid, BA) site, the formation of $TMPH^+$ complex). The $\delta^{31}P$ of adsorbed TMP spans over a wide range (-20~-58 ppm) when interacting with various metal cations on different solid acids (i.e. case (a)), whereas a $TMPH^+$ ionic complex formed when a TMP molecule adsorbs onto a bridging hydroxyl proton tends to give rise to a ^{31}P resonance in a much narrower range of -2 to -5 ppm (i.e. case (c)). For isolated hydroxyl proton, its interaction with TMP usually gives a signal at higher field (~-61 ppm, i.e. case (b)). Therefore, Lewis acid (electron acceptor), Brønsted acid (proton donor) and physical-adsorbed sites on metal oxide surface can be readily distinguished using TMP by ^{31}P magic angle spinning (MAS) NMR.

Even though above technique can provide the information of BA and LA on metal oxides, the knowledge of the distribution of those sites on various facets, which is the key point to understand the facet-dependent activity, is still deficient. Given that each facet possesses distinctive intrinsic energy, it is understandable that both concentration and chemical state of surface features differ from facet to facet. As the nucleophilic sensitive probe molecule, TMP, can form a stable adduct with the exposed cation (Lewis acid, LA) of metal oxide surface, the formation of a surface TMP-LA complex can be realized by the coordination of the P atom to the surface LA center. As the stronger interaction between TMP and surface LA pushes ^{31}P chemical shift ($\delta^{31}P$) toward downfield (i.e. zero ppm). Accordingly, we expect this TMP-assisted NMR technique should be able to differentiate cations (either proton or cation) with various chemical states on their corresponding host facet by chemical shifts and further quantify them by corresponding peak intensity. In chapter 4 and 5, three morphologies of ZnO nanoparticles with different ratio of exposed (002) and (100) facets were firstly prepared to study the correlation between $\delta^{31}P$ and the adsorption configurations of TMP on various ZnO facets. Qualitative and quantitative information on both chemical

state and distribution of surface cations have been well-resolved achieved. Later, in chapter 6, we further prepared anatase TiO_2 samples with different ratio of exposed (001) and (101) facets promoted with various surface groups (e.g. -O-, -OH, -F and -SO_4). We are, for the first time, able to monitor the electronic effect imposed by different adsorbates during sequential treatments/modifications to particle surface cation.

References:

[1] M. N. Chong, B. Jin, C. W. K. Chow, C. Saint, *Water Research* **2010**, *44*, 2997−3027.

[2] K. M. Lee, C. W. Lai, K. S. Ngai, J. C. Juan, *Water Research* **2016**, *88*, 428−448.

[3] J. Schneider, M. Matsuoka, M. Takeuchi, J. Zhang, Y. Horiuchi, M. Anpo, D. W. Bahnemann, *Chem. Rev.* **2014**, *114*, 9919−9986.

[4] B.-G. Zhai, Y. M. Huang, *Optoelectron. Mater.* **2016**, *1*, 22–36.

[5] S. Bai, L. Wang, Z. Li, Y. Xiong, *Adv. Sci.* **2017**, *4*, 1600216.

[6] M. R. Hoffmann, S. T. Martin, W. Choi, D. W. Bahnemann, *Chem. Rev.* **1995**, *95*, 69–96.

[7] Ohtani, B. *Catalysts* **2013**, *3*, 942–953.

[8] H. S. Fogler, in: Elements of Chemical Reaction Engineering, Chapter 10: Catalysis and Catalytic Reactors. Prentice-Hall PTR Inc, 1991, pp. 581-685.

[9] K. Vinodgopal, P. V. Kamat, *J. Phys. Chem.* **1992**, *96*, 5053–5059.

[10] G. Liu, J. C. Yu, G. Q. Lu, H. M. Cheng, *Chem. Commun.* **2011**, *47*, 6763–6783.

[11] K. Zhou, Y. Li, *Angew. Chem. Int. Ed.* **2012**, *51*, 602–613.

[12] H. Xu, P. Reunchan, S. Ouyang, H. Tong, N. Umezawa, T. Kako, J. Ye, *Chem. Mater.* **2013**, *25*, 405–411.

[13] J. Jiang, K. Zhao, X. Xiao, L. Zhang, *J. Am. Chem. Soc.* **2012**, *134*, 4473–4476.

[14] N. Wu, J. Wang, D. N. Tafen, H. Wang, J. G. Zheng, J. P. Lewis, X. Liu, S. S. Leonard, A. Manivannan, *J. Am. Chem. Soc.* **2010**, *132*, 6679–6685.

[15] R. Li, F. Zhang, D. Wang, J. Yang, M. Li, J. Zhu, X. Zhou, H. Fan, C. Li, *Nat. Commun.* **2013**, *4*, 1432

[16] Y. Yin, A. P. Alivisatos, *Nature* **2005**, *437*, 664–670.

[17] M. A. Boles, D. Ling, T. Hyeon, D. V. Talapin, *Nat. Mater.* **2016**, *15*, 141–153.

[18] C. Wöll, *Prog. Surf. Sci.* **2007**, *82*, 55–120.

[19] E. S. Jang, J. H. Won, S.-J. Hwang, J. H. Choy, *Adv. Mater.* **2006**, *18*, 3309−3312.

[20] G. R. Li, T. Hu, G. L. Pan, T. Y. Yan, X. P. Gao, H. Y. Zhu, *J. Phys. Chem. C* **2008**, *112*, 11859−11864.

[21] A. McLaren, T. Valdes-Solis, G. Li, S. C. Tsang, *J. Am. Chem. Soc.* **2009**, *131*, 12540−12541.

[22] F. Liao, Y. Huang, J. Ge, W. Zheng, K. Tedsree, P. Collier, X. Hong, S. C. Tsang, *Angew. Chem., Int. Ed.* **2011**, *50*, 2162−2165.

[23] M. Behrens, F. Studt, I. Kasatkin, S. Kühl, M. Hävecker, F. Abild-Pedersen, S. Zander, F. Girgsdies, P. Kurr, B.-L. Kniep, M. Tovar, R. W. Fischer, J. K. Nørskov, R. Schlögl, *Science* **2012**, *336*, 893−897.

[24] Y. Qin, X. Wang, Z. L. Wang, *Nature* **2008**, *451*, 809−813.

[25] L. Wang, Y. Kang, X. Liu, S. Zhang, W. Huang, S. Wang, *Sens. Actuators, B* **2012**, *162*, 237−243.

[26] U. Diebold, L. V. Koplitz, O. Dulub, *Appl. Surf. Sci.* **2004**, *237*, 336−342.

[27] S. A. Ansari, M. M. Khan, S. Kalathil, A. Nisar, J. Lee, M. H. Cho, Nanoscale **2013**, *5*, 9238–9246.

[28] Y. Lv, W. Yao, X. Ma, C. Pan, R. Zong, Y. Zhu, *Catal. Sci. Technol.* **2013**, *3*, 136–3146.

[29] F. Kayaci, S. Vempati, I. Donmez, N. Biyikli, T. Uyar, *Nanoscale* **2014**, *6*, 10224–10234.

[30] X. Zhang, J. Qin, Y. Xue, P. Yu, B. Zhang, L. Wang, R. Liu, *Sci. Rep.* **2014**, *4*, 4596.

[31] T. Andelman, Y. Gong, M. Polking, M. Yin, I. Kuskovsky, G. Neumark, S. O'Brien, *J. Phys. Chem. B* **2005**, *109*, 14314–14318.

[32] H. Zeng, G. Duan, Y. Li, S. Yang, X. Xu, W. Cai, *Adv. Funct. Mater.* **2010**, *20*, 561–572.

[33] K. M. Wong, S. M. Alay-e-Abbas, Y. Fang, A. Shaukat, Y. Lei, *J. Appl. Phys.* **2013**, *114*, 034901.

[34] Y.-K. Peng, Y. Fu, L. Zhang, I. F. Teixeira, L. Ye, H. He, S. C. E. Tsang, *ChemCatChem* **2017**, *9*, 155–160.

[35] Y. K. Peng, L. Ye, J. Qu, L. Zhang, Y. Fu, I. F. Teixeira, I. J. McPherson, H. He, S. C. E. Tsang, *J. Am. Chem. Soc.* **2016**, *138*, 2225 –2234.

[36] B. Yu, C. Zhu, F. Gan, Y. Huang, *Mater. Lett.* **1998**, *33*, 247–250.

[37] L. Jing, Z. Xu, J. Shang, X. Sun, W. Cai, H. Guo, *Mater. Sci. Eng. A* **2002**, *332*, 356–361.

[38] S. Polarz, J. Strunk, V. Ischenko, M. W. E. van den Berg, O. Hinrichsen, M. Muhler, M. Driess, *Angew. Chem. Int. Ed.* **2006**, *45*, 2965–2969.

[39] J. J. Schneider, R. C. Hoffmann, J. Engstler, S. Dilfer, A. Klyszcz, E. Erdem, P. Jakes, R. A. Eichel, *J. Mater. Chem.* **2009**, *19*, 1449–1457.

[40] F. Liao, Y. Huang, J. Ge, W. Zheng, K. Tedsree, P. Collier, X. Hong, S. C. Tsang, *Angew. Chem. Int. Ed.* **2011**, *52*, 2162–2165.

[41] V. Ischenko, S. Polarz, D. Grote, V. Stavarache, K. Fink, M. Driess, *Adv. Funct. Mater.* **2005**, *15*, 1945–1954.

[42] E. Carter, A. F. Carley, D. M. Murphy, *ChemPhysChem* **2007**, *8*, 113–123.

[43] E. Carter, A. F. Carley, D. M. Murphy, *J. Phys. Chem. C* **2007**, *111*, 10630 –10638.

[44] A. Corma, *Chem. Rev.* **1995**, *95*, 559–614.

[45] A. Bhan, A. Allian, G. Sunley, D. Law, E. Iglesia, *J. Am. Chem. Soc.* **2007**, *129*, 4919–4924.

[46] A. Zheng, S.-J. Huang, S.-B. Liu, F. Deng, *Phys. Chem. Chem. Phys.* **2011**, *13*, 14889–14901.

[47] W. Q. Fang, X.-Q. Gong, H. G. Yang, *J. Phys. Chem. Lett.* **2011**, *2*, 725–734.

[48] S. Liu, J. Yu, M. Jaroniec, *Chem. Mater.* **2011**, *23*, 4085–4093.

[49] M. V. Dozzi, E. Selli, *Catalysts* **2013**, *3*, 455–485.

[50] G. Liu, H. G. Yang, J. Pan, Y. Q. Yang, G. Q. Lu, H.-M. Cheng, *Chem. Rev.* **2014**, *114*, 9559−9612.

[51] A. Selloni, *Nat. Mater.* **2008**, *7*, 613–615.

[52] H. G. Yang, C. H. Sun, S. Z. Qiao, J. Zou, G. Liu, S. C. Smith, H. M. Cheng, G. Q. Lu, *Nature* **2008**, *453*, 638−642.

[53] X. Han, Q. Kuang, M. Jin, Z. Xie, L. Zheng, *J. Am. Chem. Soc.* **2009**, *131*, 3152–3153.

[54] H. G. Yang, G. Liu, S. Z. Qiao, C. H. Sun, Y. G. Jin, S. C. Smith, J. Zou, H. M.

Cheng, G. Q. Lu, *J. Am. Chem. Soc.* **2009**, *131*, 4078–4083.

[55] S. Liu, J. Yu, M. Jaroniec, *J. Am. Chem. Soc.* **2010**, *132*, 11914–11916.

[56] J. Pan, G. Liu, G. Q. Lu, H.-M. Cheng, *Angew. Chem. Int. Ed.* **2011**, *50*, 2133–2137.

[57] T. R. Gordon, M. Cargnello, T. Paik, F. Mangolini, R. T. Weber, P. Fornasiero, C. B. Murray, *J. Am. Chem. Soc.* **2012**, *134*, 6751−6761.

[58] J. Yu, L. Qi, M. Jaroniec, *J. Phys. Chem. C* **2010**, *114*, 13118–13125.

[59] Q. Xiang, K. Lv, J. Yua, *Appl Catal B.* **2010**, *95*, 557–564.

[60] Y. Jiang, J. Scott, R. Amal, *Appl Catal B.* **2012**, *126*, 290–297.

[61] T. Tachikawa, S. Yamashita, T. Majima, *J. Am. Chem. Soc.* **2011**, *133*, 7197–7204.

[62] M. D'Arienzo, J. Carbajo, A. Bahamonde, M. Crippa, S. Polizzi, R. Scotti, L. Wahba, F. Morazzoni, *J. Am. Chem. Soc.* **2011**, *133*, 17652–17661.

[63] J. Yu, J. Low, W. Xiao, P. Zhou, M. Jaroniec, *J. Am. Chem. Soc.* **2014**, *136*, 8839−8842.

[64] X. Yu, B. Jeon, Y. K. Kim, *ACS Catal.* **2015**, *5*, 3316−3322.

[65] Y. Luan, L. Jing, Y. Xie, X. Sun, Y. Feng, H. Fu, ACS Catal. **2013**, 3, 1378−1385.

[66] Q. Wu, M. Liu, Z. Wu, Y. Li, L. Piao, *J. Phys. Chem. C* **2012**, *16*, 26800−26804.

[67] F. Xiong, Y.-Y. Yu, Z. Wu, G. Sun, L. Ding, Y. Jin, X.-Q. Gong, W. Huang, *Angew. Chem. Int. Ed.* **2016**, *55*, 623–628.

[68] J. Yu, J. Fan, K. Lv, *Nanoscale* **2010**, *2*, 2144–2149.

[69] X. Wu, Z. Chen, G. Q. Lu, L. Wang, *Adv. Funct. Mater.* **2011**, *21*, 4167–4172.

[70] F. Hao, X. Wang, C. Zhou, X. Jiao, X. Li, J. Li, H. Lin, *J. Phys. Chem. C* **2012**, *116*, 19164−19172.

[71] L. Chu, Z. Qin, J. Yang, X. Li, *Sci. Rep.* **2015**, *5,* 12143.

[72] J. S. Chen, Y. L. Tan, C. M. Li, Y. L. Cheah, D. Luan, S. Madhavi, F. Y. C. Boey, L. A. Archer, X. W. Lou, *J. Am. Chem. Soc.* **2010**, *132,* 6124–6130.

[73] X.-L. Cheng, M. Hu, R. Huang, J.-S. Jiang, *ACS Appl. Mater. Interfaces* **2014**, *6*, 19176−19183.

[74] L. Atanda, S. Mukundan, A. Shrotri, Q. Ma, J. Beltramini, *ChemCatChem* **2015**, *7*, 781–790.

[75] L. Atanda, A. Shrotri, S. Mukundan, Q. Ma, M. Konarova, J. Beltramini, *ChemSusChem* **2015**, *8*, 2907–2916.

[76] X. C. Wang, J. C. Yu, P. Liu, X. X. Wang, W. Y. Su, X. Z. Fu, *J. Photochem. Photobiol. A* **2006**, *179*, 339−347.

[77] H. Zhang, H. Yu, A. Zheng, S. Li, W. Shen, F. Deng, *Environ. Sci. Technol.* **2008**, *42*, 5316–5321.

[78] B. E. Hardin, H. J. Snaith, M. D. McGehee, *Nat. Photonics* **2012**, *6*, 162–169.

[79] H. Kusama, H. Orita, H. Sugihara, *Langmuir* **2008**, *24*, 4411–4419.

[80] Y.-K. Peng, Y. Hu, H.-L. Chou, Y. Fu, I. F. Teixeira, L. Zhang, H. He, S. C. E. Tsang, *Nat. Commun.* accepted.

[81] S. Selçuk, A. Selloni, *J. Phys. Chem. C* **2013**, *117*, 6358−6362.

[82] W. Yuan, Y. Wang, H. Li, H. Wu, Z. Zhang, A. Selloni, C. Sun, *Nano Lett.* **2016**, *16*, 132–137.

[83] W. Yuan, H. Wu, H. Li, Z. Dai, Z. Zhang, C. Sun, Y. Wang, *Chem. Mater.* **2017**, *29*, 3189–3194.

[84] G. Liu, H. G. Yang, X. Wang, L. Cheng, H. Lu, L. Wang, G. Q. Lu, H.-M. Cheng, *J. Phys. Chem. C* **2009**, *113*, 21784–21788.

[85] W. Wei, N. Yaru, L. Chunhua, X. Zhongzi, *RSC Adv.* **2012**, *2*, 8286–8288.

[86] X. H. Yang, Z. Li, C. Sun, H. G. Yang, C. Li, *Chem. Mater.* **2011**, *23*, 3486–3494.

[87] K. Lv, Q. Xiang, J. Yua, *Appl Catal B.* **2011**, *104*, 275–281.

[88] H. Park, W. Choi, *J. Phys. Chem. B* **2004**, *108*, 4086-4093.

[89] W. P. Rothwell, W. Shen, J. H. Lunsford, *J. Am. Chem. Soc.* **1984**, *106*, 2452–2453.

Chapter 2 Analytical Techniques

2.1. Chapter overview

The aim of this chapter is to present and briefly introduce the background of analytical techniques used in this thesis for the surface characterization of ZnO (chapter 4 and chapter 5) and TiO_2 (chapter 6 and chapter 7) nanoparticles. Corresponding results will be discussed in following chapters. In particular, focus will be on nuclear magnetic resonance (NMR) and its application as an advanced tool for surface characterization.

2.2. X-ray Diffraction (XRD)

X-ray diffraction is one of the commonly employed techniques in crystallographic characterization which provides information on crystalline phase, lattice unit cell parameters and crystallite size by examining the diffraction pattern of a material. In general, this technique is based on the constructive interference of X-rays scattered by interactions with atoms in a periodic lattice. The diffraction patterns are related not only to the spacing between atomic planes but also the size of the crystallite. Accordingly, XRD is used here for the identification of both crystalline and size of the material. XRD spectra are obtained by the introducing an X-ray source towards a crystalline sample at different angles **(Figure 2-1)** [1]. As X-rays can interact with electron clouds of atoms in the sample and then elastically scatter, the periodic arrangement of atoms in crystalline sample results in the constructive interference of scattered X-rays when the scattering angle θ (between the incoming X-rays and the reflecting lattice plane), wavelength of the source λ and the lattice spacing of the sample d satisfy Bragg's Law **(Equation 2-1)**.

$$n\lambda = 2d \sin\theta;\ n = 1, 2\ldots. \quad \textbf{(Equation 2-1)}$$

where n is the integer corresponds to the order of reflection; conventional lab use λ= 0.154 nm.

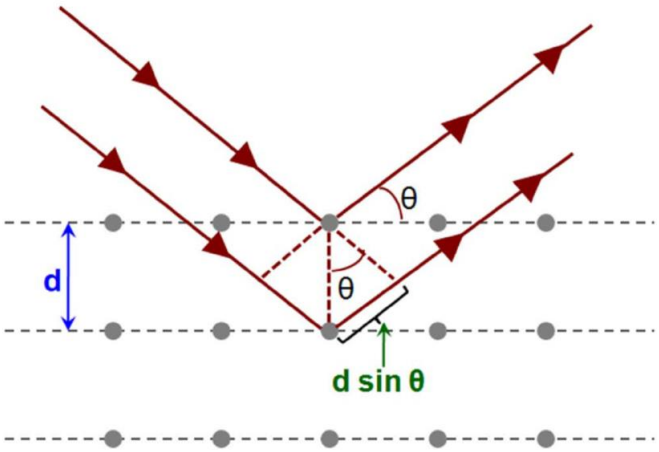

Figure 2-1. Diffraction of X-rays from crystal lattice planes illustrating Bragg's law [1].

During XRD measurement, powder crystallites are oriented in any possible direction relative to the beam of radiation. Accordingly, samples show diffracted rays corresponding to all sets of planes in the crystal. A preferred stacking orientation of crystalline particles on the sample holder may lead to the amplification of a particular X-ray signal compared to others in the compound. The lattice parameters can be calculated based on the peak positions and the corresponding full width half maximum (FWHM). For example, the orthogonal crystal system can be described by:

$$1/d^2=h^2/a^2+k^2/b^2+l^2/c^2 \quad \textbf{(Equation 2-2)}$$

where h, k and l are the Miller indices; a, b, c are the lattice parameters; d is the spacing between planes.

On the other hand, the peak broadening has been demonstrated related to the decrease of crystallite size due to the incomplete destructive interference where the X-rays are

out of phase. Accordingly, the particle size can be calculated from the width of diffraction peak using the Scherrer equation:

$$L = K\lambda/\beta\cos\theta \quad \textbf{(Equation 2-3)}$$

where L is the is the averaged diameter of the particles; λ is the wavelength of the incident X-ray; β is the width of a diffraction peak at half the maximum (FWHM) in radians; θ is the Bragg angle; K is a constant in the range of 0.87-1.00 (it is usually assumed to be 1).

2.3. X-ray Photoelectron Spectroscopy (XPS)

XPS is currently the most surface sensitive technique providing information about element composition and corresponding oxidation state near the sample surface. As shown in **Figure 2-2**, a valence or a core electron of the targeting atom can be ejected by absorbing X-ray from the nucleus with a kinetic energy (E_k).

$$E_k = h\upsilon - E_B - \varphi \quad \textbf{(Equation 2-4)}$$

where E_k is the kinetic energy of the ejected electron; h is Planck's constant; υ is the frequency of the incident X-ray; E_B is the binding energy of the ejected electron; φ is the work function of the spectrometer.

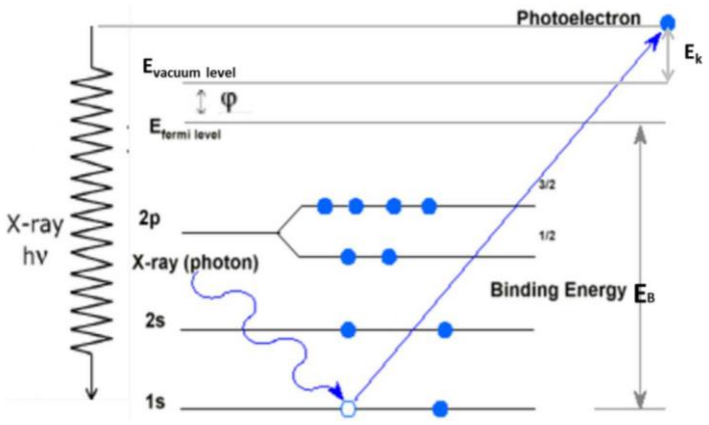

Figure 2-2. Illustration of photoelectron emission stimulated by X-ray absorption [2].

The binding energy of the electron (E_B) can reflect the host element of the electron and the corresponding oxidation state as well [2]. As the kinetic energy (E_k) of ejected electron detected by spectrometer is related to E_B **(Equation 2-4)**, the element composition(s) and corresponding oxidation state(s) can therefore be determined. The XPS signal is usually used to quantitatively analyze surface chemical composition by the integration of area below. However, as X-ray can go deeply into the material, only a small fraction of surface photoelectrons can escape from the material and be detected by the spectrometer. Therefore, extra caution is needed while dealing with quantitative data.

2.4. Transmission Electron Microscopy (TEM)

TEM is a very useful analytical technique for the study of materials with various morphologies on the nanoscale. It provides information about the finest details of the internal structure of the material and the size and shape of nanomaterials. The principle of TEM is similar to that of an optical microscope that electrons instead of photons are used as source. Also, electromagnetic lenses instead of optical lenses are used to focus electron beam. **Figure 2-3** shows the structure and cross-section of a typical TEM. Electrons are generated either by a tungsten filament, LaB_6 crystal or field emission gun. They are then being accelerated to an energy with wavelength much smaller than typical interatomic spacing and focused to specimen by a series of magnetic lenses [3]. For electrons to go through the specimen, samples must be thinner than 100 nm. This can be achieved by dispersing the sample in a volatile solvent before loading the sample on TEM grid. The transmitted electron beam (through the sample) is then refocused through sets of lenses and projected onto a phosphor screen. Images of the sample are captured using a charge coupled device (CCD) camera or film. As the resolution of TEM depends on the wavelength of electron, typical operating voltage of a TEM instrument are 100 ~

200 keV (λ = 2.5 to 3.7 pm) under 10^{-6} mbar vacuum, corresponding to a resolution of 0.3 nm.

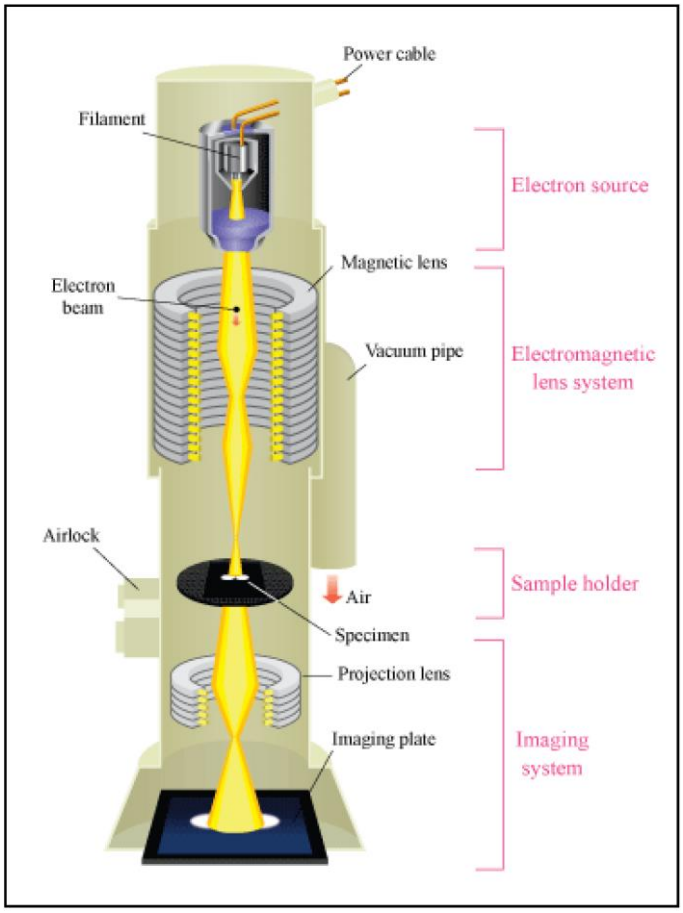

Figure 2-3. The structure and cross-section of a typical TEM [3].

2.5. Ultraviolet-visible (UV-vis) absorption spectroscopy

Ultraviolet-visible (UV-vis) absorption spectroscopy is a widely applied analytical technique to characterize the absorption of sample as a function of wavelength in the UV-vis spectral region. In this region, atoms, molecules, dispersed colloidal semiconductor and metal nanocrystals undergo electronic transitions from the ground state to the excited state. By comparing the intensity of light at a wavelength before and after passing through a sample, Beer noticed that the attenuation of intensity is related to the concentration of the sample. Such relationship is then formulated as the Lambert-Beer law as below:

$$A = -\log_{10}(I/I_0) = \varepsilon lc \quad \textbf{(Equation 2-5)}$$

where A is the absorbance (Absorbance Units (AU)), I and I_0 are is the intensity of the incident light and transmitted light at a given wavelength, l is the path length of light through the sample, and c is the concentration of the sample, ε is the extinction coefficient for each species and wavelength (constant).

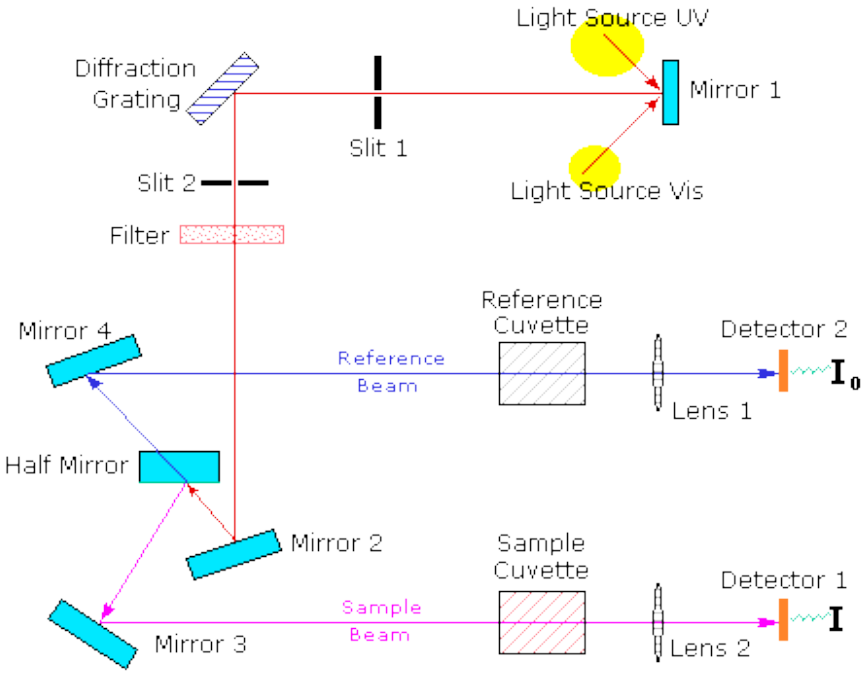

Figure 2-4. Setup of the double beam UV-vis spectroscopy [4].

Figure 2-4 shows the setup of the double beam UV-vis spectroscopy. The UV-vis light is usually generated by a tungsten lamp (320 nm to 3500 nm), while deuterium lamp is usually employed to generate shorter wavelength UV light from 160 nm to 360 nm. Light dispersing elements such as prisms or diffraction gratings are used for wavelength scanning. Detectors are usually photomultipliers consisting of diodes for the detection of a wide range of wavelengths.

2.6. Photoluminescence (PL) emission spectroscopy

Photoluminescence (PL) is a term that includes both fluorescence (fast emission, ~ nanosecond scale) and phosphorescence emission (slow emission, ~microsecond scale) from a molecule or semiconductor solids. For semiconductor solids, the excitation state is characterized by the existence of an exciton, which is produced by the excitation of a valence band electron to the conduction band. As PL spectroscopy measurements can either be time-resolved or steady-state, it is a useful technique for studying exciton behavior. Only steady-state measurements are used in this thesis. Steady-state PL involves the sample excitation at a single wavelength and the detection of emission intensity (perpendicular to excitation) over a range of wavelengths.

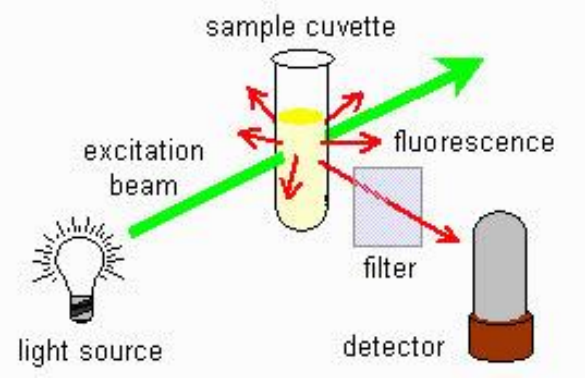

Figure 2-5. Typical setup of a steady-state fluorescence spectrometer [5].

Steady state PL spectra are recorded on detectors that collect emission perpendicular to the direction of sample excitation **(Figure 2-5)**. The light source scans wavelengths between 200~800 nm. An excitation monochromator is equipped to select the wavelength for excitation, which is larger than the bandgap of semiconductor solids. An emission monochromator is then used for the recording of emission as a function of wavelength.

2.7. Electron Paramagnetic Resonance (EPR)

EPR is a technique for studying materials with unpaired electrons. As an electron has a spin quantum number s = 1/2, with magnetic components m_s = +1/2 and m_s = −1/2. Without external magnetic field, electrons in the two separated energy levels follow the Boltzmann distribution and are degenerated. However, when they are exposed to an external magnetic field, the splitting of energy level will be governed by the parallel or antiparallel alignment of electron magnetic moment to the field:

$$E=m_s g_e \mu_B B_0 \quad \textbf{(Equation 2-6)}$$

where E is the energy level of the unpaired electron, B_0 is the strength of magnetic field, μ_B is the Bohr magneton, g_e is so called g-factor. The gap between two states for unpaired free electrons is proportional to the strength of magnetic field (i.e. $\Delta E = g_e \mu_B B_0$) **(Figure 2-6)**.

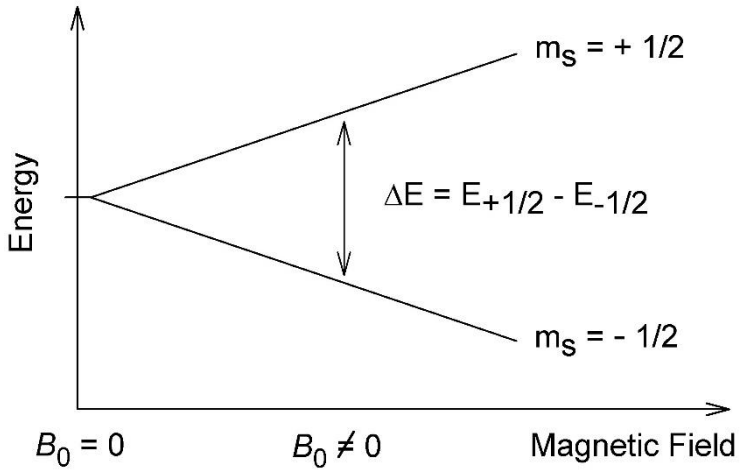

Figure 2-6. Illustration of energy splitting of unpaired electron with stimulation of external magnetic field [6].

When exposed to microwaves with energy equals to ΔE, the unpaired electrons can be excited from lower to higher energy level by absorbing photons. According to the position (frequency) of the absorption signal, g factor can be calculated. For a free electron, g_e equals to 2.00. However, for an unpaired electron sitting on a radicals or

defects, the effective field strength (B_{eff}) experienced by the target unpaired electron is affected by its surrounding atoms (cf. B_0). The relation between B_{eff} and B_0 can be written as:

$$B_{eff}=(1-\sigma)B_0 \quad \textbf{(Equation 2-7)}$$

where σ is the total effect of all the surrounding atoms and the EPR signal should be observed at:

$$h\nu = g_e \mu_B B_0(1-\sigma) \quad \textbf{(Equation 2-8)}$$

The shift of g value indicates the change of the chemical environment of the unpaired electron. Therefore, EPR is a very sensitive technique for the detection and identification of free radicals or paramagnetic centers. In this study, EPR was used as a characterization tool to evaluate the defects of semiconductor solids. It is well-known that the valence electrons of semiconductor materials can be excited to conduction band easily by heat or light. However, those excited electrons can recombine with holes immediately unless they are trapped by defects and thus prolong the life time. For a material in nanosize, many defects and interstitial sites inside or on the surface are introduced. These sites can trap the excited electrons long enough to be observed in the EPR spectra.

2.8. Nuclear Magnetic Resonance (NMR)

When nuclear magnetic moment associated with a nuclear spin (I) is placed under external magnetic field, the different spin states split and give different nuclear spin states. Under external static magnetic field (spin polarization), a radio frequency signal of the proper frequency can generate a transition between these spin states. This "spin flip" generates some spins in their higher energy states. When the radio frequency signal is turned off, the relaxation of the spins returns to the lower state and produces

corresponding resonant frequency. This process is called Nuclear Magnetic Resonance (NMR). NMR is thus a physical phenomenon in which nuclei interact with external magnetic field then absorbs radiation at a specific frequency. This frequency depends on both the strength of the magnetic field and the magnetic properties of the isotope of the atoms. As NMR can provide a wealth of information about electronic interaction between atoms either in solution or in solid form, it has been widely applied to study molecular physics, crystals and non-crystalline materials nowadays.

2.8.1. The nucleus in a magnetic field

The basic concepts of nuclear magnetic resonance (NMR) are similar to those of EPR mentioned above, but the spins of atomic nuclei are excited instead of the electron spins. However, NMR is more complicated in this case that only certain nuclei respond to an external magnetic field and some of them with more than two spin states (I > 1/2) will give multi-transitions between states. Some rules to predict whether or not a given nucleus/isotope has NMR signal are listed below (also see **Table 2-1**):

Nucleus	I	Number of states	m values
^{11}B	$\frac{3}{2}$	4	$-\frac{3}{2}, -\frac{1}{2}, \frac{1}{2}, \frac{3}{2}$
^{12}C	0	1	0
^{14}N	1	3	$-1, 0, 1$
^{17}O	$\frac{5}{2}$	6	$-\frac{5}{2}, -\frac{3}{2}, -\frac{1}{2}, \frac{1}{2}, \frac{3}{2}, \frac{5}{2}$
^{31}P	$\frac{1}{2}$	2	$-\frac{1}{2}, \frac{1}{2}$

Table 2-1. Examples of nucleus with different nuclear spin [7].

1. A nucleus or isotope with even atomic mass (A), atomic number (Z) and neutron number (N) will give zero nuclear spin (I = 0) and thus no NMR signal (e.g. ^{12}C, ^{16}O, ^{18}O and ^{32}S).
2. While a nucleus/isotope with even A but odd both Z and N will give integer I and be detectable by NMR (e.g. ^{2}H (I = 1), ^{10}B(I=3) and ^{14}N(I=1)).

3. For a nucleus/isotope with odd A (either odd Z and even N or even Z and odd N), the spin states can be expressed as n/2 (n is an odd integer) and also be detectable by NMR (e.g. ^{1}H (I = 1/2), ^{11}B (I = 3/2), ^{13}C (I = 1/2), ^{14}N (I = 1/2), ^{17}O (I = 5/2), ^{31}P (I = 1/2))

2.8.2. Nuclear Zeeman effect and Larmor frequency

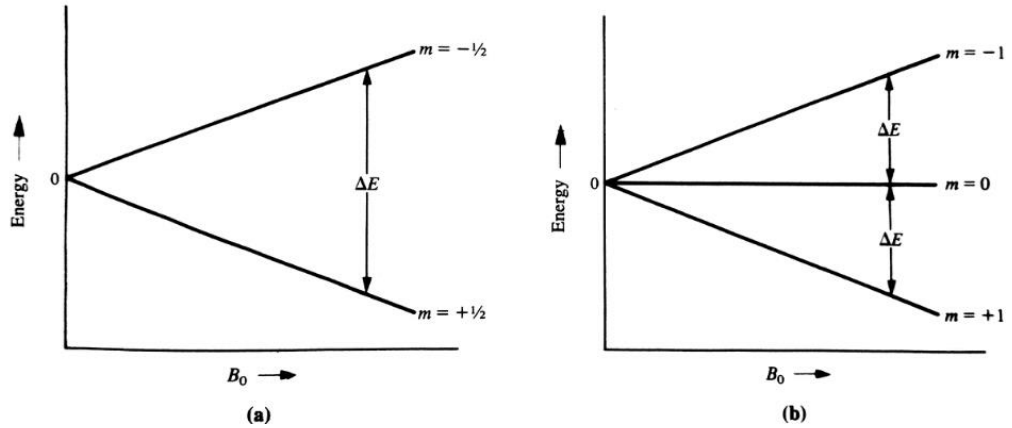

Figure 2-7. Illustration of energy splitting of the nuclear Zeeman effect. (a) Nucleus with (a) I = 1/2 and (b) I = 1 [7].

The spin state energy expressed below is proportional to nuclear spin number (m_i) and the strength of external magnetic field (B_0):

$$E_i = -m_i B_0 (rh/2\pi) \quad \textbf{(Equation 2-9)}$$

Where h is Planck's constant and r is the magnetogyric ratio (a constant characteristic of the nucleus being examined). For a nucleus with I = 1/2 **(Figure 2-7a)**, the difference between states is $\Delta E = B_0(rh/2\pi)$. When this energy gap matches the energy of absorbed photon, the proton will undergo precession with a characteristic angular frequency (i.e. Lamor frequency, ω):

$$E_{photon} = h\nu_{photon} = \Delta E = B_0(rh/2\pi) = h\nu_{precession} = (h/2\pi)\omega_{precession} \quad \textbf{(Equation 2-10)}$$

Classically, the Larmor frequency is the precession of the magnetic moment around the magnetic field. Here, it is used to visualize the quantum energy of transition between the two possible spin states for spin 1/2.

Table 2-2 listed some of common isotopes with their nuclear constants. It is clear that proton has the largest r value, while larger nuclei have lower value. Relative sensitivity is also compared with the strength of signal of ^{1}H. According to natural abundance and sensitivity, ^{1}H, ^{19}F and ^{31}P are the most easily studied nuclei.

TABLE 2-1 Nuclear Properties of Selected Isotopes[1]

Isotope	Relative natural abundance (%)	Z	N	A	I	$\gamma/10^6$ (rad T^{-1} s^{-1})	ν (MHz at 1 T)	Relative sensitivity[2]
^{1}H	99.985	1	0	1	$\frac{1}{2}$	267.512	42.5759	1.00
^{2}H	0.015	1	1	2	$\frac{1}{2}$	41.0648	6.53566	9.65×10^{-3}
^{7}Li	92.58	3	4	7	$\frac{3}{2}$	103.96	16.546	0.293
^{10}B	19.58	5	5	10	3	28.748	4.5754	1.99×10^{-2}
^{11}B	80.42	5	6	11	$\frac{3}{2}$	85.828	13.660	0.165
^{13}C	1.108	6	7	13	$\frac{1}{2}$	67.2640	10.7054	1.59×10^{-2}
^{14}N	99.63	7	7	14	1	19.325	3.0756	1.01×10^{-3}
^{15}N	0.37	7	8	15	$\frac{1}{2}$	27.107	4.3142	1.04×10^{-3}
^{17}O	0.037	8	9	17	$\frac{5}{2}$	36.27	5.772	2.91×10^{-2}
^{19}F	100	9	10	19	$\frac{1}{2}$	251.667	40.0541	0.833
^{23}Na	100	11	12	23	$\frac{3}{2}$	70.761	11.262	9.25×10^{-2}
^{27}Al	100	13	14	27	$\frac{5}{2}$	69.706	11.094	0.206
^{29}Si	4.70	14	15	29	$\frac{1}{2}$	53.142	8.4578	7.84×10^{-3}
^{31}P	100	15	16	31	$\frac{1}{2}$	108.29	17.235	6.63×10^{-2}
^{33}S	0.76	16	17	33	$\frac{3}{2}$	20.517	3.2654	2.26×10^{-3}
^{35}Cl	75.53	17	18	35	$\frac{3}{2}$	26.212	4.1717	4.70×10^{-3}
^{37}Cl	24.47	17	20	37	$\frac{3}{2}$	21.82	3.472	2.71×10^{-3}

Table 2-2. Nuclear properties of selected isotopes [7].

2.8.3. Boltzman distribution

In quantum mechanics, for net absorption to occur, there must be more particles in the lower-energy state than in the higher one. When no net absorption absorption is possible, this condition called saturation. For any system at thermal equilibrium, the population of lower states is always larger than that of higher states. Boltzmann distribution is the equation describing the relationship between energy gap and relative numbers of particles in those states:

$$P_{m=-1/2}/P_{m=+1/2}=e^{-\Delta E/kT}$$ **(Equation 2-11)**

Where P is the fraction of the nuclei in -1/2 and +1/2 states, T is the absolute

temperature and K is the Boltzmann constant of $1.381*10^{-28}$ J•K^{-1}. For 1H nuclei under 2.35T at 298 K, the fraction for $P_{-1/2}$ is 0.4999959 and $P_{+1/2}$ is 0.5000041. Even though the difference is extremely small, it is enough for the generation of NMR signal. According to Equation 2-11, anything to increase the difference in population can give rise to a more intense NMR signal (e.g. increase the strength of NMR).

2.8.4. Experimetal setup of NMR

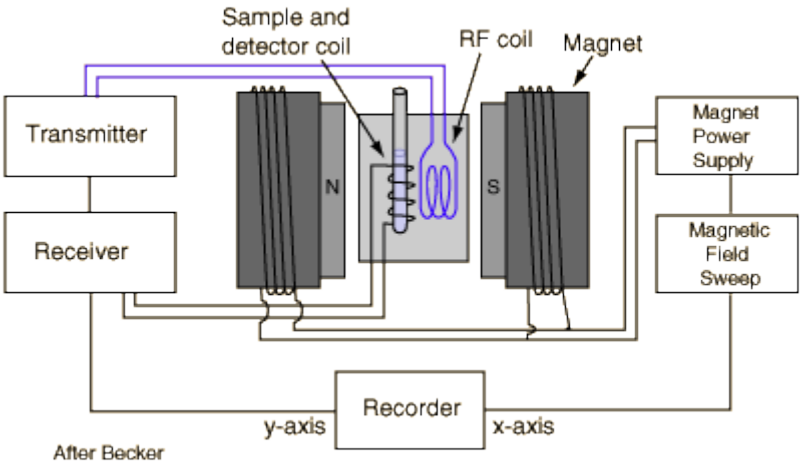

Figure 2-8. The experimental setup of NMR [8].

Figure 2-8 shows a practical NMR instrument. Take proton NMR as an example, a sample containing protons (hydrogen nuclei) is positioned under a strong magnetic field to generate polarization of the protons. A field in the range of radio frequency (RF) is then introduced on the sample to excite the nuclear spins into their higher energy state (i.e. from $E_{m = +1/2}$ to $E_{m = -1/2}$). When this RF is switched off, the spins will return to their lower state and at the same time generate a small amount of radiation at the Larmor frequency. This emission is associated with the "spin relaxation" of the protons from their excited state and the strength of field. It can be detected by the detector coil which is amplified to display the NMR signal.

References:

[1] W. Clegg, A. J. Blake, R. O. Gould, *Main crystal structure analysis: principles and practice*, Oxford Science Publication, Chester, **2001**.

[2] J. W. Niemantsverdriet, *Spectroscopy in catalysis: an introduction, 3rd completely revised and enlarged edn.,* Wiley-VCH, Weinheim, **2007**.

[3] The source of image: http://www.hk-phy.org

[4] The source of image: https://www.chemistry.msu.edu

[5] The source of image: http://www.chromedia.org

[6] A. Schweiger, G. Jeschke, *Principles of Pulse Electron Paramagnetic Resonance. Oxford University Press*, **2001**.

[7] R. S. Macomber, *NMR spectroscopy: essential theory and practice*, Harcourt Brace Jovanovich, **1988**.

[8] The source of image: http://hyperphysics.phy-astr.gsu.edu

Chapter 3 Experimental Methods

3.1. Synthesis procedure

3.1.1. ZnO: single-crystalline nanoplate

ZnO nanoplates were synthesized according to the procedure reported by McLaren et al. [1]. 6.0 g zinc acetate dihydrate ($Zn(Ac)_2 \cdot 2H_2O$) and 3.84g hexamethylenetetramine (HMT, $C_6H_{12}N_4$) were dissolved in 48 mL deionized water. After a stirring of 10 min, the solution was transferred into a 100 mL Teflon-lined autoclave and maintained at 99 °C for 24 h. Then it was cooled to room temperature naturally. The white precipitate was collected by centrifugation at 5000 rpm for 10 min, after which the supernatant was decanted and discarded. The solid was washed repeatedly with ethanol and water to remove excess precursor. All ZnO nanoplate was dried in oven (100 °C) for 12 h and then calcined at 450 °C for 2 h (remove surfactant) with a heating rate of 10 °C/min in an air atmosphere.

3.1.2. ZnO: single-crystalline nanorod

ZnO nanorods were synthesized according to the procedure reported by Liao et al. [2]. 1.487 g zinc nitrate hexahydrate ($Zn(NO_3)_2 \cdot 6H_2O$) and 6 g NaOH were dissolved in 10 mL deionized water (the molar ratio of Zn^{2+} to OH^- was 1:30). 100 mL ethanol was added to the Zn precursor solution. Five mL 1,2-ethanediamine (EDA) was also put into the mixture and then transferred to a covered plastic container with a volume capacity of 250 mL. The reaction container was kept at room temperature under constant stirring about 3 days. After the synthesis, a white crystalline product was centrifuged and washed with deionized water and pure ethanol repeatedly. All ZnO nanorod was dried in oven (100 °C) for 12 h and then calcined at 450 °C for 2 h (remove surfactant) with a heating rate of 10 °C/min in an air atmosphere.

3.1.3. ZnO: poly-crystalline nanopowder

The preparation of ZnO nanopowder is similar to a method introduced by Tian et al. [3]. The evaporating dish with 28g of $Zn(Ac)_2 \cdot 2H_2O$ solid was placed into a furnace, for which the temperature was increased from room temperature to 450 °C with a heating rate of 10 °C/min in an air atmosphere and kept at the maximum temperature for 120 min. After naturally cooling to room temperature, the white powder was collected.

3.1.4. TiO_2: anatase nanocrystal with different morphologies

The preparation of anatase TiO_2 nanocrystals with different ratio of exposed (001) and (101) facets is referred to the procedure reported by Han et al. [4]. 5.0 mL of $Ti(OC_4H_9)_4$ was mixed with a certain amount of hydrofluoric acid (40~48 wt.%) in a Teflon-lined autoclave with a capacity of 40 ml and subsequently heated to 180 °C at a ramp rate of $2°C \cdot min^{-1}$. The temperature was kept at 180 °C for 24 h. After hydrothermal reaction, the white precipitate was collected, washed with ethanol and distilled water three times, and then dried in an oven at 80 °C overnight. 0.6 mL hydrofluoric acid (HF) was added for F-(001) and 0.2 mL HF/0.4 mL H_2O was added for F-(101), respectively, while, instead of HF, 0.6 mL of H_2O was employed for powder (PD) sample.

3.1.5. TiO_2: treatments for F removal and subsequent sulfation

NaOH removal of surface fluorine. The NaOH wash was employed in this study according to previous literature [4]. 1.0 g of as-prepared TiO_2 sample was treated in 50.0 mL of 0.1 M NaOH solution under magnetic stirring for 10 h (0.05 M and 0.5 M NaOH were also adopted for comparison). The solid sample was then washed with distilled water several times until neutral. After centrifugation, the solid was dried at 80

°C overnight. TiO_2 samples (i.e. PD, F-(101) and F-(001)) obtained after receiving 0.1M NaOH wash were denoted as Na-PD, Na-(101) and Na-(001).

Calcination removal of surface fluorine. The calcination treatment was also carried out according to previous report [5]. 1.0 g of as-prepared TiO_2 sample was calcined at 600ºC for 90 min (ramping rate: 5ºC/min). We denoted TiO_2 samples after receiving this treatment as Cal-PD, Cal-(101) and Cal-(001).

Sulfation. To obtain the sulfated TiO_2, ammonium sulphate ($(NH_4)_2SO_4$) was utilized as the precursor of sulfate in the catalyst preparation [6]. For example, 1.0 g of Na-PD/Cal-PD sample was added into 10.0 mL of 1 mol•L^{-1} $(NH_4)_2SO_4$ solution to stir for 8 h and then collected by centrifugation. The solid was then calcined at 450 °C for 4 h. We denoted Na-PD and Cal-PD sample after sulfation as S-Na-PD and S-Cal-PD. Same treatments were also employed to the other two morphologies.

3.1.6. Trimethylphosphine(TMP)-adsorbed sample for ^{13}P MAS NMR

About 150 mg of ZnO or TiO_2 sample was placed in a home-made glass tube and activated at 150 ºC for 2 h under vacuum (10^{-1} Pa) to ensure maximum adsorption of TMP molecules. After cooling down to room temperature, the system **(Figure 3-1)** connecting TMP tube and sample tube was isolated from the left part of vacuum system before the introduction of TMP molecules. 300 μmol/catalyst g (calculated by the pressure and volume of isolated system) of TMP was then introduced into this system. Wait for ~10 min until the pressure of this isolated system reach a plateau, which means the equilibrium between TMP and catalyst surface has been achieved. The tap to TMP and sample tubes were then closed before the removal of extra TMP molecules by left vacuum system. These steps were repeated three times to ensure the fully adsorption of TMP on catalyst surface. The sample tube was then flame sealed for storage and

transferred to Bruker 4 mm ZrO_2 rotor with a Kel-F endcap in a glove box under nitrogen atmosphere before NMR measurement.

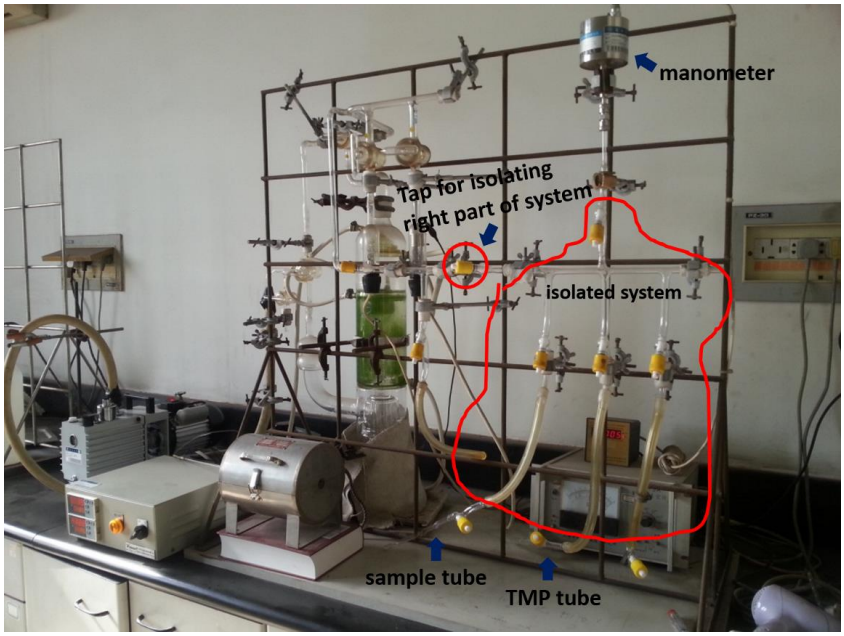

Figure 3-1 The system setup for TMP-adsorption.

3.2. Catalytic testing

3.2.1. Photocatalytic activity testing of ZnO nanoparticles

Comparative catalytic testing was conducted at room temperature, with constant magnetic stirring to ensure full suspension of the particles throughout. An aqueous methylene blue (MB) stock solution (11.2 mg/L) was used for all photoreactions. 2.5 mg of ZnO sample was dispersed in 20 mL dye stock solution (11.2 mg/L catalyst concentration) and stirred for 30 min in the dark to allow dye adsorption/desorption to equilibrate. The reaction mixture was then exposed to irradiation with constant stirring in a Luzchem photoreactor fitted with 8 UVA lamps with nonmonochromatic irradiation centered at 350 nm. 1.5 mL samples of catalyst/dye solution were extracted at 5−10 min intervals and centrifuged at 4000 rpm for 5 min. Dye concentration was determined by tracking dye absorption at 664.5 nm using a PerkinElmer LAMBDA 750S UV/vis/NIR spectrophotometer after centrifuging each sample at 5000 rpm for 10

min to remove the suspended photocatalysts from solution. The decomposition of the dye over time was fitted to a pseudo-first-order rate equation $C = C_0e^{-kt}$, where C = concentration at time t, C_0 = concentration at time t = 0, k = apparent rate constant (k_{app}) and t = irradiation time. Plotting $-\ln(C/C_0)$ vs irradiation time (t) results in a straight line with slope equal to k_{app}, which is a comparative measure of activity (kinetic efficiency) of the photoreaction.

3.2.2. Photocatalytic activity testing of TiO_2 nanoparticles

Comparative catalytic testing was conducted at room temperature, with a constant magnetic stirring to ensure full suspension of the particles. An aqueous MalachiteGreen (MG) stock solution (15 mg/L) was used for all photoreactions. 20 mg of TiO_2 sample was dispersed in 100 mL dye stock solution and stirred for 30 min in the dark to allow dye adsorption/desorption to equilibrate (this experiment was carried out by collaborators at Fudan University, China).

3.2.3. Catalytic Pechmann condensation of TiO_2 nanoparticles

The catalytic activities of TiO_2 samples were studied for the synthesis of 5,7-dihydroxy-4-methyl coumarin from phloroglucinol and ethyl acetoacetate under solvent free condition. 5 mmol of phloroglucinol was reacted with 10 mmol of ethyl acetoacetate in the presence of 0.1 g of catalyst. The reaction mixture was kept at 130 °C under reflux for 2 hr. On completion of the reaction, the mixture was allowed to cool down to the room temperature followed by the addition of ethanol. The reaction mixture was filtered to separate the catalyst and the filtrate was analysed by liquid chromatography (DIONEX U3000). The yield of 5,7-dihydroxy-4-methyl coumarin was calculated as: Yield (%) = (Obtained weight of product)/ (Theoretical weight of product) × 100. (this experiment was carried out by collaborators at Fudan University, China).

3.3. Characterization procedures

3.3.1. XRD

XRD spectra were collected using a Philips PW1729 diffractometer, operating in Bragg-Brentano focusing geometry and using Cu Kα radiation (λ = 1.5418 Å) **(Figure 3-2)**. Samples were prepared a layer of dry powdered sample onto a flat glass holder.

Figure 3-2. The PANalytical X'Pert Pro X-ray diffractometer in Inorganic Chemistry Laboratory building (Department of Chemistry, University of Oxford).

3.3.2. XPS

Samples were measured with a VG Escalab II spectrometer equipped with Al X-ray source (1486.3 eV) in Chemistry Research Laboratory building (Department of Chemistry, University of Oxford). A hemispherical analyzer was employed for the detection of electrons. Charge neutralization was applied using a combined low energy/ion flood source. The resulting spectra were analysed using CasaXPS peak fitting software and sample charging corrected using C 1s at 285.00 eV as a reference setting. All XPS measurements in this thesis were carried out by surface analysis staff.

3.3.3. TEM

TEM images were obtained using a JEOL 2010 microscope with a high-resolution pole piece in Begbroke science park (Department of Materials, University of Oxford). The samples were prepared by placing the powder of nanoparticles onto a carbon-coated copper grid. All TEM images in this thesis were taken by a colleague in Tsang's group.

3.3.4. UV-Vis absorption

Both liquid and solid-state samples were measured using a Perkin-Elmer LAMBDA 750S UV/Vis/NIR spectrometer **(Figure 3-3)**. For liquid state analysis: absorption spectra were then recorded in absorption mode after a 100% transmission baseline had been collected with the sample cuvettes removed. Aqueous methylene blue samples from photocatalytic testing were recorded in absorption mode after a 100% transmission baseline had been collected with only water in cuvettes. For solid-state analysis: the sample was compressed into a sample disk (diameter = 13 mm, thickness = ~3 mm) using an applied force of 10 tons for 60 seconds. The sample disk was placed into the beam path in the integrating sphere compartment of the spectrometer. Spectra were recorded in absorption mode and referenced to the standard Teflon reflecting disks.

Figure 3-3. The Perkin-Elmer LAMBDA 750S UV/Vis/NIR spectrometer in Inorganic Chemistry Laboratory building (Department of Chemistry, University of Oxford).

3.3.5. PL Emission

Emission spectra of powder samples were recorded using a Varian Cary Eclipse Fluorescence Spectrophotometer in emission mode. Excitation and emission slits were set to 5 nm and both filters were set to auto (this experiment was carried out by collaborators at Fudan University, China).

3.3.6. EPR

The EPR spectra were obtained by X-band CW EPR spectrometer (Bruker EMX) **(Figure 3-4)**. Sample powder with known weight was loaded into EPR tube for quantitative analysis. The signal intensity versus electron spin number was obtained from the double integral of the spectrum based on a reference powder of Cu(II)TPP with 1 spin per molecule. The quantitative result can be obtained by dividing electron spin number by sample weight.

Figure 3-4. The X-band CW EPR spectrometer in Inorganic Chemistry Laboratory building (Department of Chemistry, University of Oxford).

3.3.7. TMP-assisted Quantitative ^{31}P MAS NMR

Figure 3-6. The Bruker AVIII 400 (solids) NMR spectrometer in Chemistry Research Laboratory building (Department of Chemistry, University of Oxford).

Solid state magic angle spinning (MAS) NMR measurements were carried out using a Bruker AVIII 400 spectrometer at room temperature **(Figure 3-6)**. To remove the effect of proton spins on ^{31}P spectra, a strong radio frequency field (B) is usually applied in a pulsed at the resonance frequency of the non-observed abundant spins (^{1}H herein) which contribute to the coupling of both spin species. If B is strong such that spins of ^{1}H is flipped rapidly compared with the spin-spin interactions, the interaction is averaged to zero and consequently the excess broadening is zero. The high power decoupling (HPDEC) was thus used for the quantitative ^{31}P analysis. Considering the long relaxation time of ^{31}P nuclei in NMR experiment, we used 30° pulse with the width of 1.20 μs, 15 s delay time. The radiofrequency for decoupling was 59 kHz. The spectral width was 400 ppm, from 200 to −200 ppm. The number of scanning was 800. The ^{31}P chemical shifts were reported relative to 85% aqueous solution of H_3PO_4, with $NH_4H_2PO_4$ as a secondary standard (0.81 ppm). The quantitative analysis of adsorbed TMP molecules was calculated according to the calibration line established by running

standard samples with various adsorbed TMP concentration.

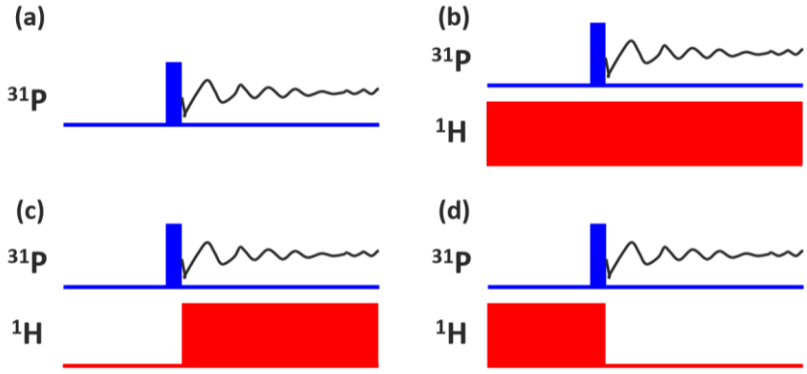

Figure 3-7. (a) One-pulse sequence (no decoupling), (b) 100% duty cycle proton decoupling (for proton decoupling and nuclear overhauser effect (NOE) enhancement), (c) inverse gated proton decoupling (no NOE but proton decoupling) and (d) gated proton decoupling (proton coupling and NOE enhancement).

A simple one-pulse sequence as shown in **Figure 3-7a** may generally be used to quantify ^{31}P from the signal intensity in solid-state NMR. However, this application strongly subjects to the environment of ^{31}P nucleus used. Regarding to the probe molecule, the trimethylphosphine (TMP), three ^{1}H are close to ^{31}P in space causing a strong heteronuclear dipole-dipole coupling interaction. This dipole-dipole coupling interaction is much stronger than the J-coupling interaction normally observed in liquid NMR. Thus, the former leads to severe broadening of the ^{31}P peaks in TMP study. Therefore, it results serious overlapping of neighboring peaks and increases the difficulties in the peak assignments. This dipole-dipole interaction can be efficiently removed by introducing the second frequency for ^{1}H decoupling. However, if the ^{1}H decoupling is applied during the entire duration of the experiment (recycle delay and data acquisition) **(Figure 3-7b)**, the nuclear overhauser effect (NOE) will enhance the signals from certain phosphorus disproportionately, leading to non-quantitative spectra. To remove the interference of NOE from quantitative analysis, we adopted the inverse gated decoupling **(Figure 3-7c)**: the decoupling is on only during the acquisition period,

to suppress NOE and obtain a quantitative result. Compared with one-pulse ^{31}P MAS NMR experiment, a continuous irradiation is applied to the ^{1}H channel during the acquisition time in our HPDEC (high power decoupling) MAS NMR experiment.

Mixture	The weight percent of $NH_4H_2PO_4$	The total weight of measured sample (mg)	The relative number of ^{31}P	The relative area of ^{31}P signal
A	100.0	115.1	100	100
B	74.6	115.4	75	77
C	48.8	122.7	52	53

Table 3-1. Mixtures of $NH_4H_2PO_4$ and $NaNO_3$ with different ^{31}P concentration and their corresponding quantitative ^{31}P NMR results.

As this HPDEC sequence can efficiently eliminate the influence of dipole-diploe coupling interactions from ^{1}H and NOE effect, it has actually been widely employed in MAS NMR measurements, e.g. for the quantitative evaluations of Brönsted/Lewis acid sites on TMP adsorbed microporous zeolites reported in literature (H-mordenite [7], H-ZSM-5 [8]), mesoporous molecular sieves (SBA-15 and MCM-41 [9]) and metal oxide nanoparticles (TiO_2 [10], Niobates [11], ZnO [12]). To further demonstrate the HPDEC sequence in our study can be used quantitatively, $NH_4H_2PO_4$ and $NaNO_3$ were physically mixed with three different weight percents (i.e. 100%, 74.6% and 48.8% for $NH_4H_2PO_4$, **Table 3-1**). Corresponding ^{31}P HPDEC MAS NMR results are also summarized in the Table. By normalizing the number of the ^{31}P nuclei in pure $NH_4H_2PO_4$ (i.e. mixture A) and its NMR peak intensity as 100, the relative ^{31}P peak areas of their mixture B and C were found to match very well with the numbers of ^{31}P nuclei in each mixture.

Although cross polarization (CP) technique has been widely employed in solid-state NMR to enhance the signal of nuclei with low gyromagnetic ratio or long T_1 relaxation.

For the case of TMP, the abundant nucleus is ^{1}H and the observed nucleus is ^{31}P. If the abundant ^{1}H is excited, and its energy is transferred to the observed ^{31}P by using a CP on both channels **(Figure 3-8)**. The ^{31}P signal intensity can thus be enhanced by exploiting the polarization of the nearby proton nuclei. Since this process involves transfer from ^{1}H to ^{31}P in the solid state, the number and distance of proton nearby could significantly vary ^{31}P signal intensity. However, as the surface probe molecule for solid metal oxide, the number and distance of proton around ^{31}P (TMP) vary with its interactions with different surface features. As shown in **Figure 3-5**, the TMP molecule can bind to (a) metal cation, (b) isolated and (c) bridging hydroxyl proton. Both (b) and (c) cases (especially for case (c) with chemical bond formation between ^{1}H and ^{31}P) can give stronger ^{31}P intensity as an additional proton in a close proximity (cf. case (a)). As CP could lead to variation in signal intensities with multiple ^{31}P environments, we thus adopted HPDEC rather than CP in this paper for the quantification of various surface features.

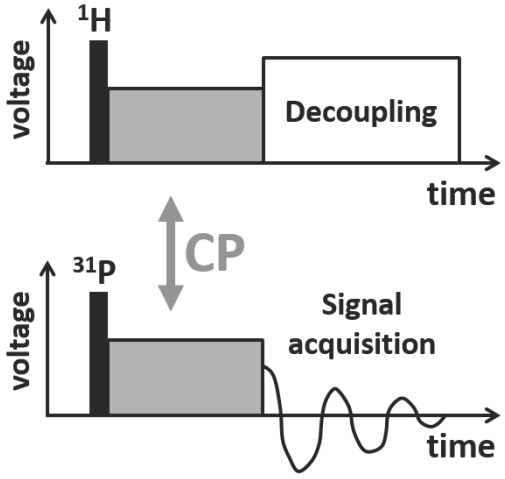

Figure 3-8. Pulse sequence of $^{1}H \rightarrow ^{31}P$ cross polarization MAS solid-state NMR.

As we know, the T_1 for adsorbed TMP should be shorter than pure TMP as a result of the additional interactions between adsorbed TMP and solid adsorbent. Under the same

acquisition parameters, if a delay time is sufficiently long enough for pure TMP sample, it will be enough for bound TMP on adsorbents and can be employed for the ^{31}P MAS NMR experiments in this paper. To shorten the delay time and obtain a better signal-to-noise ratio in a given time, we have used 30^{o} pulse with a pulse width of 1.2 μs in the ^{31}P MAS NMR experiments for both the pure TMP and also the adsorbed TMP in this study. First, we introduced a fixed quantity of TMP into a home-made glass tube, which fitted into a 4 mm Bruker zirconia rotor, with the help of liquid nitrogen in a vacuum line. Then, we chose 12, 15 and 20 s as the delay times while keeping other parameters unchanged. ^{31}P MAS NMR spectra were recorded accordingly and can be seen in **Figure 3-9**. We defined the peak area in ^{31}P MAS NMR spectrum obtained at a delay time of 12 s as 100, the peak area in the other two spectra obtained at a delay time of 15 s and 20 s, was found to be 99 and 100, respectively. So, a delay time of 15 s was sufficiently long enough for pure TMP in the present acquisition conditions, and was therefore chosen for the ^{31}P MAS NMR experiments in this study.

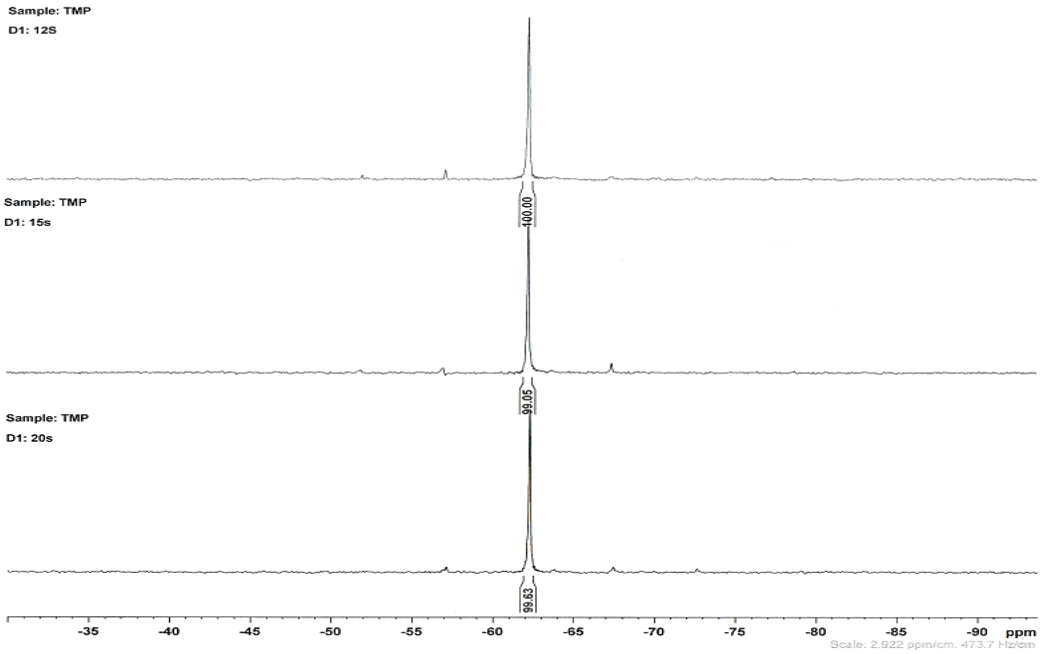

Figure 3-9. ^{31}P MAS NMR spectra of pure TMP obtained at various delay time (12, 15 and 20 s).

3.3.8. NMR spectrum deconvolution

All raw TMP NMR spectra were deconvoluted using the software 'peakfit v4.12'. "Gauss area" and fixed peak position have been used for peak deconvolution while the peak height and width were allowed to vary. Notice that the raw spectra data of samples with the same treatment/modification show a standard deviation of ±1 ppm in chemical shift position and with R^2 value > 0.98. For ZnO case, we have fixed all four positions (i.e., −43, −48, −55, and −61 ppm) for all three morphologies (plate, rod and powder) within ±1 ppm uncertainty during the spectral deconvolution. **Table 3-2** summarizes the positions fixed for TiO_2 spectra deconvolution in Lewis acid region (−20 to −58 ppm). For example, during the spectral deconvolution of F-(101) and F-(001), we have fixed two positions of Ti_5c(101) and Ti_5c(001) at −31 and −22.5 ppm within ±1 ppm uncertainty. Also, for S-Na-PD, S-Na-(101) and S-Na-(001), the position of Ti_5c(101) and Ti_5c(001) were fixed at −25.5 and −34 ppm within ±1 ppm uncertainty.

Positions fixed in for deconvolution		
Peak 1	Peak 2	Peak 3
F-(001) & F-(101)		
-22.5	-31	-42.5
Na-(001) & Na-(101)		
-28	-36.5	-41
Cal-(001) & Cal-PD		
-35	-41	-50
S-Na-(001) & S-Na-(101) & S-Na-PD		
-25.5	-34	-

Table 3-2. Summary of the positions fixed for TiO_2 spectra deconvolution in LA region (-20 ppm to -58 ppm).

References:

[1] A. McLaren, T. Valdes-Solis, G. Li, S. C. Tsang, *J. Am. Chem. Soc.* **2009**, *131*, 12540–12541.

[2] F. Liao, Y. Huang, J. Ge, W. Zheng, K. Tedsree, P. Collier, X. Hong, S. C. Tsang, *Angew. Chem. Int. Ed.* **2011**, *50*, 2162–2165.

[3] C. Tian, Q. Zhang, A. Wu, M. Jiang, Z. Liang, B. Jiang, H. Fu, *Chem. Commun.* **2012**, *48*, 2858–2860

[4] X. Han, Q. Kuang, M. Jin, Z. Xie, L. Zheng, *J. Am. Chem. Soc.* **2009**, *131*, 3152–3153.

[5] H. G. Yang, C. H. Sun, S. Z. Qiao, J. Zou, G. Liu, S. C. Smith, H. M. Cheng, G. Q. Lu, *Nature* **2008**, *453*, 638−641.

[6] Y. Hu, B. Guo, Y. Fu, Y. Ren, G. Tang, X. Chen, B. Yue, H. He, *Chem. Commun.* **2015**, *51*, 14219–14222.

[7] H.-M. Kao, C.-Y. Yu, M.-C. Yeh, *Micropor. Mesoporo. Mater.* **2002**, *53*, 1–12.

[8] Q. Zhao, W.-H. Chen, S.-J. Huang, Y.-C. Wu, H.-K. Lee, S.-B. Liu, *J. Phys. Chem. B* **2002**, *106*, 4462–4469.

[9] Q. Luo, F. Deng, Z. Yuan, J. Yang, M. Zhang, Y. Yue, C. Ye, *J. Phys. Chem. B* **2003**, *107*, 2435–2442.

[10] H. Zhang, H. Yu, A. Zheng, S. Li, W. Shen, F. Deng, *Environ. Sci. Technol.* **2008**, *42*, 5316–5321.

[11] H. T. Kreissl, K. Nakagawa, Y.-K. Peng, Y. Koito, J. Zheng, S. C. E. Tsang, *J. Catal.* **2016**, *338*, 329–339.

[12] Y.-K. Peng, L. Ye, J. Qu, L. Zhang, Y. Fu, I. F. Teixeira, I. J. McPherson, H. He, S. C. E. Tsang, *J. Am. Chem. Soc.* **2016**, *138*, 2225–2234.

Chapter 4 ZnO: Trimethylphosphine-assisted surface fingerprinting by ^{31}P MAS NMR

4.1. Chapter overview

Nano metal oxides are becoming widely used in industrial, commercial and personal products (semiconductors, optics, solar cells, catalysts, paints, cosmetics, sun-cream lotions, etc.). However, the relationship of surface features (exposed planes, defects and chemical functionalities) with physiochemical properties is not well studied primarily due to lack of a simple technique for their characterization. In this chapter, solid state ^{31}P MAS NMR is used to map surfaces on various ZnO samples with the assistance of trimethylphosphine (TMP) as a chemical probe. As similar to XRD giving structural information on a crystal, it is demonstrated that this new surface-fingerprint technique not only provides qualitative (chemical shift) but also quantitative (peak intensity) information on the concentration and distribution of cations and anions, oxygen vacancies and hydroxyl groups on various facets from a single deconvoluted ^{31}P NMR spectrum.

4.2. Introduction

Single-crystalline nanoparticles (NPs) with tailored facets show different physiochemical properties from their polycrystalline counterparts and have recently attracted much research interest [1−9]. Over the past decade, the variety of these materials has been actively expanded as their performance in fields such as optics [1,2], electronic devices [3,4], solar cells [5,6], and heterogeneous catalysis [7-9] is found to be greatly improved with the exposure of a specific facet. In particular, in the field of

heterogeneous catalysis, which intrinsically involves the breakage and formation of chemical bonds between reactant and product at the catalyst surface, is closely associated with the coordination environment of the surface active atoms. The crystal facets exposed at the surface are, in turn, predominantly determined by the shape of the catalyst particle. For example, Pt (111) facets show much better methanol oxidation reactivity in fuel cell tests [7], tetrahexahedral platinum NPs give superior electro-oxidation activity [8], and the MgO (100) face plays a critical role in providing appropriate adsorption, molecular trafficking, and desorption during the benzylation of aromatics [9]. Since the active sites can be enriched and tuned by controlling particle morphology, the design and fabrication of singlecrystalline NPs exposing a large fraction of targeted facets has been intensively pursued using a wide range of processing techniques, such as hydrolysis [10], hydrothermal processing [11], microemulsion [12], and thermal evaporation [13]. Ideally, the continuing development of these nanocatalysts with morphology-dependent activity would not only deepen understanding of the structural sensitivity of such catalysts, by correlating their reaction performance with their dominant crystal facet, but also bridge the gap between the model catalysts used in surface science and the real catalysts found in practical applications.

Often, however, comparison of such morphology-dependence is limited to individual studies, as the processing and posttreatment techniques used in the preparation of catalysts varies from group to group. This results in many differences between nanoparticles, in addition to the exposed facet, such as in the particle size distribution, extent of surface hydroxylation and particle homogeneity. Cross-literature comparison of NP catalysts is thus seriously hindered as there is currently no universal technique which can provide quantitative analysis of the concentration/distribution of surface

features and the percentage of the desired facet on a given sample. For example, the tailoring of ZnO NPs to expose specific facets has been receiving increasing attention due to superior performances in solar cells and photocatalysis [14-16], methanol synthesis [17,18], optoelectronics [19] and gas sensing [20], which were all attributed to increased concentration of oxygen vacancies (V_O) on polar surface. However, there is currently no method to reliably characterize the facets, nor the V_O for a given ZnO crystallite. Photoluminescence (PL) and electron paramagnetic resonance (EPR) are the techniques most commonly used to reflect differences in V_O between samples, but they are not truly surface specific and are incapable of providing the concentration/distribution of V_O on specific facets. In fact, there have been disagreements between PL [21,22] and EPR [23,24] data in the literature.

Nuclear magnetic resonance (NMR) is a powerful technique that has been widely applied to study molecular physics, crystals and noncrystalline materials by providing a wealth of information about electronic interaction between atoms either in solution or in solid form. In general, solution NMR techniques offer higher resolution than those of solid state NMR, due to the absence of field inhomogeneity for species in solution. For example, characterization of metal colloid surfaces has recently been achieved by liquid phase ^{13}C NMR using formic acid as a chemical probe, although this method is restricted to some polymer stabilized metals which show fast tumbling motion in solution [25]. On the other hand, the use of probe molecules (e.g., ^{13}C-acetone for ^{13}C, trimethylphosphine (TMP) and trialkylphosphine oxides (R_3PO) for ^{31}P) in solid-state NMR has also been widely employed for the characterization of electronic interactions in solid structures as they can report on various microenvironments of solid surfaces [26-28]. In particular, the use of ^{31}P nucleus, with its 100% natural abundance and wide chemical shift range over 430 ppm, has been shown to be a sensitive and reliable

technique capable of providing qualitative (type and strength) and quantitative (concentration) information on the discrete acid sites in various acid catalysts [26]. Even though this method is able to provide information on the active sites of working catalysts, knowledge of the distribution of these sites on various facets, which is key to understanding facet-dependent properties, is still lacking.

Herein, using ZnO as a model material, we report TMP-assisted surface mapping of oxide nanoparticles and crystallites using ^{31}P solid-state NMR and show that it can provide comprehensive information (both qualitative and quantitative) on the surface features of various facets. As TMP, an electron donor molecule (Lewis base, LB), can form a stable adduct with the exposed cation of an oxide surface (Lewis acid, LA), the formation of a surface TMP-LA complex may be realized via coordination of the P atom to the LA center. It is shown that the ^{31}P chemical shift (δ^{31}P) of the surface TMP-LA complex is able to differentiate between surface cations (Zn^{2+} or H^{+}) on facets at high resolution, with various Lewis acidities, surface energies and steric arrangements due to the stronger surface LA site pushing δ^{31}P to downfield. Single-crystalline plate- and rod-shaped ZnO nanoparticles containing preferentially exposed (002) and (100) facets, respectively and polycrystalline ZnO powder, were prepared to study the correlation between δ^{31}P and the adsorption configurations of TMP on various ZnO facets. Information such as the nature, binding strength and concentration of active sites on the various facets can thus be extracted from a single ^{31}P solid-state NMR spectrum. As a result, this technique, together with the as-built up ZnO facet fingerprint, not only provides quantitative information on surface features but also guides the rational design of facet-dependent nanocatalysis for a given sample.

4.3. Results and discussion

4.3.1. Characterization of ZnO nanoparticles

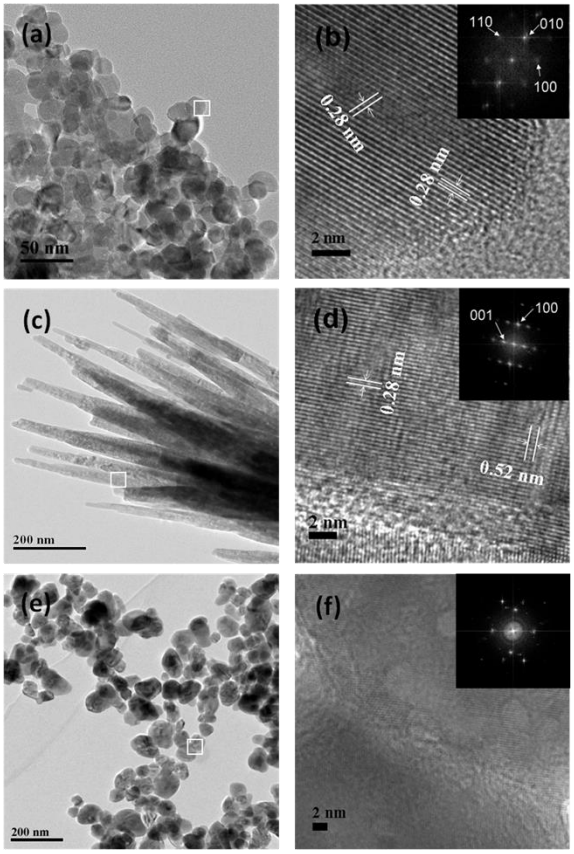

Figure 4-1. TEM and HRTEM images of ZnO a, b) plate; c, d) rod and e, f) powder. Inset: corresponding electron diffraction (ED) pattern of ZnO plate, rod and powder.

The syntheses of high quality ZnO nanocrystals with different morphologies are well documented in literature. Herein, we use single crystalline plate and rod ZnO NPs synthesized according to a reported procedure [17] and polycrystalline powder ZnO NPs prepared by the calcination of $Zn(Ac)_2 \bullet 2H_2O$ at 450°C for 2 h [29]. **Figure 4-1** shows transmission electron microscopy (TEM) images and electron diffraction (ED) patterns of as-prepared ZnO samples. The TEM image in **Figure 4-1a** reveals plate-shaped ZnO with diameters of 20-30 nm, and **Figure 4-1c** shows rod-shaped ZnO 600-800 nm long with diameters of 15-20 nm. In contrast, the powder sample **Figure 4-1e** shows irregular shapes with diameters in a wide range from 35 to 150 nm. According

to the high-resolution TEM (HRTEM) image **(Figure 4-1f)** and the ED pattern **(Figure 4-1f inset)**, the powder sample reveals polycrystallinity which is in stark contrast to the well-defined single crystalline structure of the plate **(Figure 4-1b)** and rod **(Figure 4-1d)**. As evidenced by HRTEM measurements of the plate and rod, the lattice spacing a and c is calculated to be 0.28 nm and 0.52 nm, respectively, both matching literature values [30]. For the plate, the two dominant surfaces are terminated by the (002) crystal plane but for rod the preferentially exposed surface is (100).

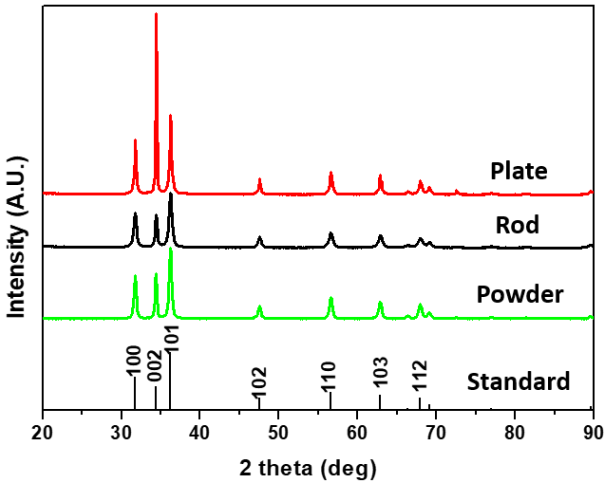

Figure 4-2. XRD spectra of ZnO plate, rod and powder.

As shown in **Figure 4-2**, XRD analysis confirms that the three ZnO samples all show the wurtzite crystal structure (JCPDF 89-0511). The intensity of the (002) peak in the plates is higher than in the other morphologies, with this predominantly polar (002) facet covering the structure, whereas both rod and powder samples show relatively higher proportions of the nonpolar (100) and (101) planes. For single crystalline ZnO, it has been shown that a change in the relative intensity of the (100) and (002) peaks in the XRD patterns of the materials corresponds to a change in particle shape [16]. An intense (100) peak (corresponding to a small (002)/(100) ratio) indicates the formation of rod oriented along the c axis. Conversely, a high (002)/(100) ratio is indicative of

shortening along the c axis and the presence of a large fraction of polar planes. Even though the XRD pattern of the powder sample is similar to that of the rod, as the powder sample was prepared without surfactant, its morphology is irregular and sphere-like owing to thermodynamic stability [31].

It is widely accepted that the growth of nanoparticle with no strong surface ligation will produce larger particle of low aspect ratios (spherical shape) due to thermodynamic driven stability (minimization of surface energy). On the other hand, a structural directing agent plays a critical role in shape control of colloidal nanoparticles since anisotropic shapes have larger surface area (cf. spherical shape), which renders them metastable, high-energy forms. Therefore, the formation of metastable shaped nanoparticles requires a kinetic growth control via chelation of structural directing agent. As the growth rate of a crystal facet depends on the surface energy (high-energy facets grow more quickly than low-energy facets), different morphologies of nanoparticle could thus be prepared by using various structural directing agents. For example, in this study, hexamethylenetetramine ($C_6H_{12}N_4$) and 1,2-ethanediamine (EDA) were employed respectively in the preparation of nanoplate and nanorod.

4.3.2. ^{31}P MAS NMR result of TMP-adsorbed ZnO nanoparticles

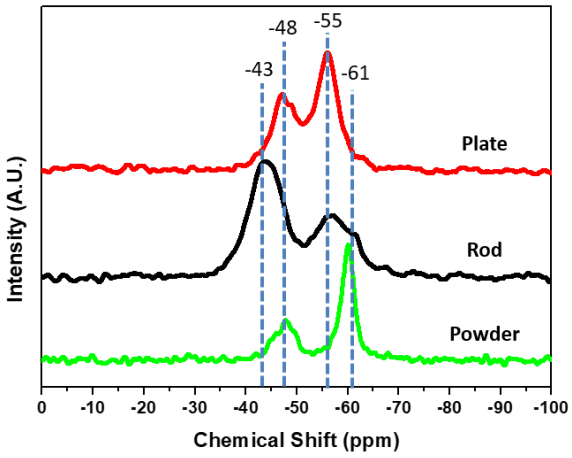

Figure 4-3. ^{31}P MAS NMR spectra of TMP-adsorbed ZnO plate, rod and powder.

Figure 4-3 shows the ^{31}P MAS NMR spectra of TMP adsorbed on ZnO plate, rod and powder. In general, a stronger interaction of the surface acidic site with the basic TMP molecule gives a more positive δ^{31}P shift in the NMR spectrum, the magnitude of the shift depending on the adsorption energy and adsorption geometry on a particular facet (vide infra). It is interesting to note from **Figure 4-3** that each sample reveals two large distinct ^{31}P resonances (-48 and -55 ppm for plate, -43 and -55 ppm for rod, -48 and -61 ppm for powder) in the range from -30 to -70 ppm. Generally, adsorbed TMP molecules can react with Brønsted Acid (BA) sites to form $TMPH^+$, giving rise to a δ^{31}P from -2 to -5 ppm, while TMP molecules bound to LA sites result in a δ^{31}P in the range from ca. -20 to -58 ppm (please refer to Chapter 3: 3.3.7) [26]. Since -61 ppm is the signal of TMP on isolated hydroxyl proton [26] and no signal of $TMPH^+$ is detected (-2 to -5 ppm) in all the three ZnO samples, the peaks at -43, -48 and -55 ppm can be initially assigned as the interactions between TMP and surface LA sites. The formation of a TMP-LA complex can be realized by the coordination of the P atom to a LA center, therefore, the lower the electron density on a LA site, the stronger the binding energy between TMP and LA site.

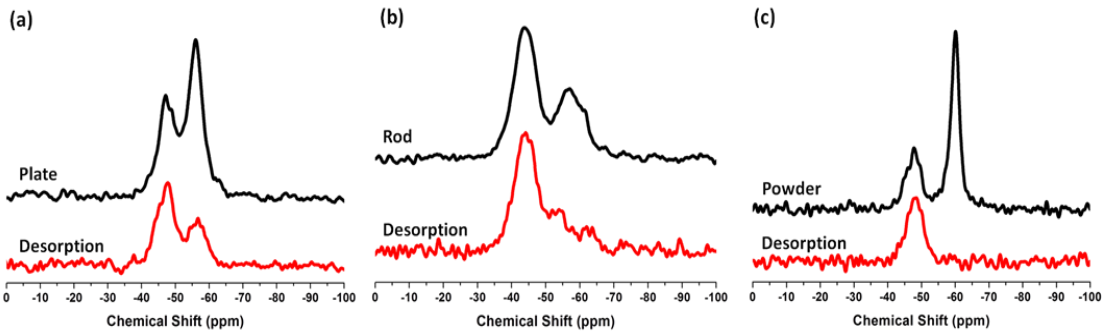

Figure 4-4. Solid-state ^{31}P MAS NMR spectra of TMP-adsorbed ZnO (a) plate, (b) rod and (c) powder with/without desorption process.

Notice that the separated desorption experiments were attempted on TMP-adsorbed plate **(Figure 4-4a)** and rod **(Figure 4-4b)** samples to determine the relative strengths

of interaction with different TMP peaks. The intensity of the peak at -55 ppm was shown to decrease pronouncedly compared to the peak at -48 ppm (plate) and -43 ppm (rod), suggesting a weaker interaction with the TMP molecule under high vaccum (<0.1 Pa). Also, the peak at -61 ppm can be disappeared after the desorption at 20°C under prolonged desorption time on the high vaccum **(Figure 4-4c)**, suggesting that this signal came from the most weakest adsorbed TMP on a surface isolated hydroxyl group (OH) [26].

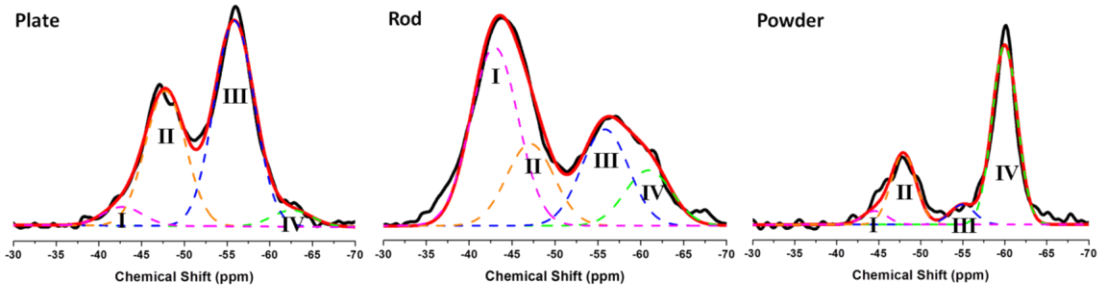

ZnO	Site I (-43 ppm)			Site II (-48 ppm)			Site III (-55 ppm)			Site IV (-61 ppm)			total coverage of OH
	ppm	Area(%)	TMP*	ppm	Area(%)	TMP*	ppm	Area(%)	TMP*	ppm	Area(%)	TMP*	
Plate	-42.8	5.2	1.83	-47.8	38.2	13.45	-55.6	52.3	18.41	-61.9	4.3	1.51	19.92
Rod	-42.9	43.8	16.01	-47.1	19.9	7.27	-55.5	23.2	8.48	-60.9	13.1	4.79	13.27
Powder	-44.1	4.6	1.62	-47.9	24.2	8.53	-54.9	6.8	2.4	-60.1	64.4	22.69	25.09

Figure 4-5. Spectral deconvolution of **Figure 4-3** and the corresponding data for each peak. *Adsorbed TMP molecules in μmol/g. The total coverage of OH on the surface was calculated from Site III and Site IV.

The spectrum of each ZnO sample is thus deconvoluted into four components, namely Site I (-43 ppm), Site II (-48 ppm), Site III (-55 ppm) and Site IV (-61 ppm) and the concentration of adsorbed TMP on each site is calculated according to the corresponding peak area **(Figure 4-5)**. Noted that the raw spectra data of all three samples show a standard deviation of around ±0.5~1 ppm in chemical shift position. Accordingly, during the spectral deconvolution, we fixed all four positions (i.e. -43, -48, -55 and -61 ppm) for all three samples within ±1 ppm uncertainty.

4.3.3. Calculation-assisted NMR peak assignment

Bader charge	Zn_{3C}	Zn_{4C}
(100) facet	10.84	10.80
(002) facet	11.03	10.70

Figure 4-6. DFT calculation of the Bader charge of surface Zn_{3C}/Zn_{4C} on (100) and (002) facets. Zn-/O-terminated (002) denoted as Zn-/O-(002) (carried out by Dr. Jin Qu).

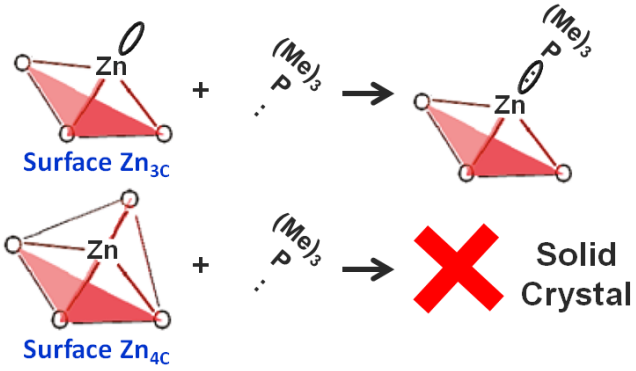

Figure 4-7. Schematic illustration of the interaction between TMP and surface Zn_{3C} and Zn_{4C} atoms.

To rationalize the nature of interactions giving rise to these peaks, adsorption energies/configurations of the basic TMP molecule on the acidic sites on each crystal facet are considered. Density function theory (DFT) calculation of Bader charge shows that Zn_{4C} sites, in which Zn^{2+} is coordinated to 4 [O] atoms, possess the highest acidity (lowest electron density) on both the (100) and (002) facets **(Figure 4-6)** (calculated by Jin Qu, East China University of Science & Technology). However, the lack of vacant sp^3 orbitals to bind the TMP, and the high energy required for transformation from tetrahedral sp^3 to trigonal bipyramidal dsp^3 geometry **(Figure 4-7)**, means the formation of adduct bond (i.e. TMP-Zn) with Zn_{4C} sites is unlikely.

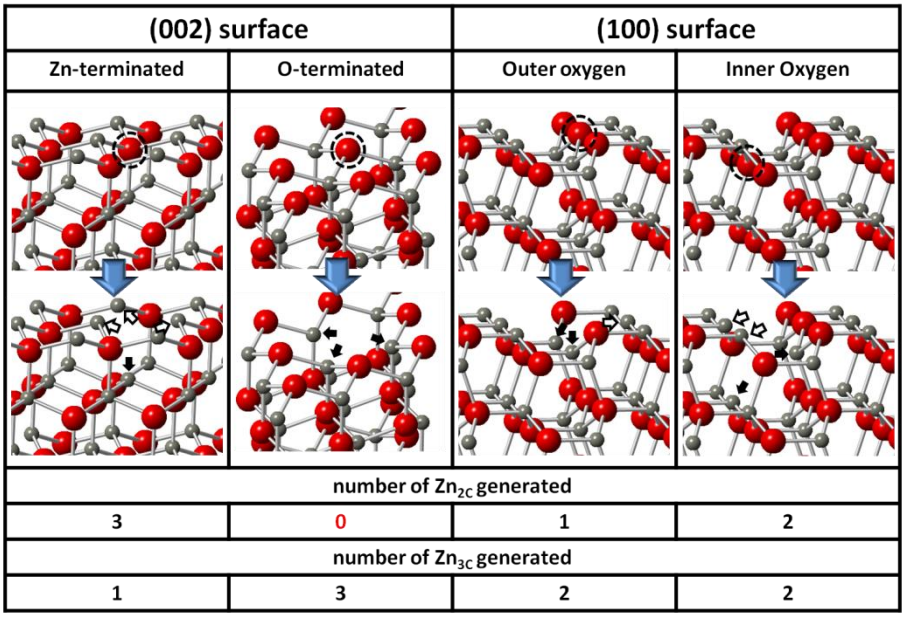

Figure 4-8. Schematic illustration of the formation of a V_o on (100), Zn-(002) and O-(002) surfaces.

facet	E_{Vo} (eV)
(100)	2.74
Zn-terminated (002)	2.85
O-terminated (002)	0.53

Table 4-1. The calculation of the formation energy of V_o on ZnO (100) and (002) surfaces (carried out by Dr. Jin Qu).

Apart from surface Zn_{4C} and Zn_{3C}, exposed Zn ions with lower coordination number ($\leqq 3$) generated during the formation of V_o were also considered. **Figure 4-8** summarizes the number of Zn_{2C}/Zn_{3C} generated during the formation of V_o on (100) and (002) surfaces. Compared to the generation of Zn_{3C} on various surfaces, the generation of Zn_{2C} is very thermodynamically unfavorable upon the formation of V_o. The formation energy of a V_o (E_{Vo}) on various facets is thus in the order of Zn-terminated (002) > (100) > O-terminated (002) (denoted as Zn-(002) and O-(002)). The theoretical calculation of E_{Vo} on (100) and (002) **(Table 4-1)** also shows the same trend: Zn-(002) > (100) >> O-(002). As the E_{Vo} of O-(002) is much lower than (100) and Zn-(002), V_o on this facet is the most favorable and should contribute mainly to the overall

V_o concentration. However, the TMP cannot bind to Zn_{3C} generated during V_o formation on O-(002) due to the direction of sp^3 orbitals **(Figure 4-9)**. Accordingly, only Zn_{3C} on the outmost surface of (100) and Zn-(002) can form chemical bond with TMP and thus give chemical shift in ^{31}P NMR measurement.

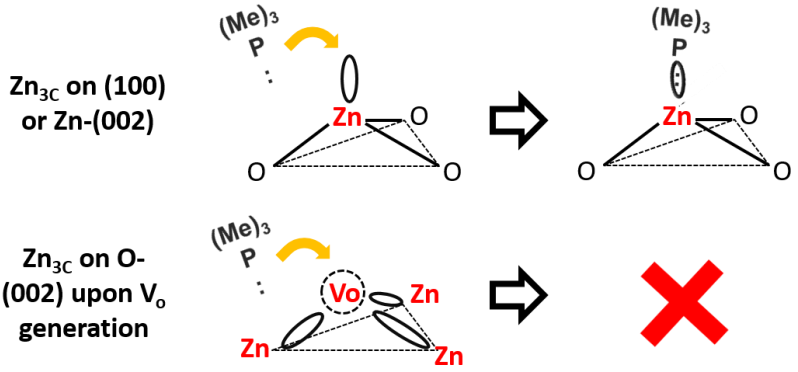

Figure 4-9. Schematic illustration of the interaction between TMP and surface Zn_{3C} on (100), Zn-(002) and O-(002).

Structure	$E_{adsorption}$ (eV) calc.	$\delta^{31}P$ (ppm) calc.	$\delta^{31}P$ (ppm)
(100)Zn_{3C}	-1.15	-41.97	-42.9
(100)Zn-OH	-0.01	-60.54	-60.9
Zn-(002)Zn_{3C}	-0.86	-	-47.8
Zn-(002)Zn-OH	-0.45	-	-55.6 (-55.1*)
O-(002)Zn-OH	-0.57	-	-55.6 (-53.0*)

Table 4-2. Calculated adsorption energy and chemical shift of TMP adsorbed on various acidic surface features of ZnO; (100)Zn_{3C}: Zn_{3C} on (100) facet; (100)Zn-OH: hydroxyl group on (100) facet; Zn-(002)Zn_{3C}: Zn_{3C} on Zn-terminated (002) facet; Zn-(002)Zn-OH and O-(002)Zn-OH: hydroxyl group on Zn-/O-terminated (002) facet, respectively *calculated from linear regression of adsorption energy **(Figure 4-10)**. (-the calculation for $\delta^{31}P$ was not reliable due to the effect of charge on the polar surfaces)

As seen from **Table 4-2**, the DFT calculations of TMP adsorption energy and chemical shift of phosphorus on anticipated acidic surface sites (Zn_{3C} and OH) and facets were carried out and are summarized therein (calculated by Jin Qu, East China University of Science & Technology). It has been observed that both binding energy [32] and adsorption energy [25] of TMP molecule on Lewis acid site of ZnO show a strong

correlation with its NMR chemical shift value. Indeed, our calculation of adsorption energy displays a linear relationship with the calculated chemical shift **(Figure 4-10)**.

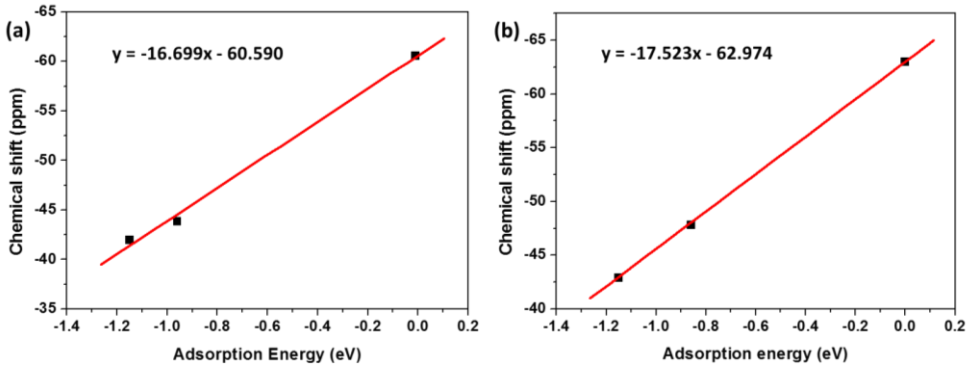

Structure	$E_{adsorption}$ (eV) cal.	$\delta^{31}P$ (ppm) cal.
$(100)Zn_{3C}$	-1.15	-41.97
$(100)Zn_{Vo(2C)}$	-0.96	-43.86
(100)Zn-OH	-0.01	-60.54

Structure	$E_{adsorption}$ (eV) cal.	$\delta^{31}P$ (ppm)
$(100)Zn_{3C}$	-1.15	-42.9
Zn-$(002)Zn_{3C}$	-0.86	-47.8
TMP molecule	0	-63

Figure 4-10. Linear regression plot by a) using calculated chemical shift and calculated adsorption energy of TMP on (100). b) Using experimental $\delta^{31}P$ and calculated adsorption energy.

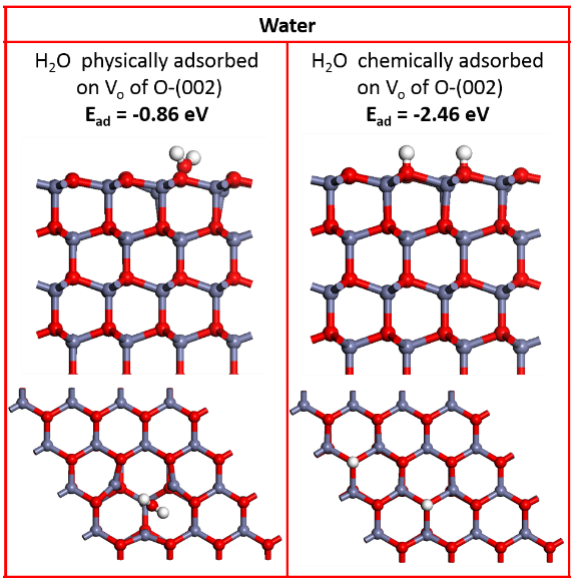

Figure 4-11. DFT calculations of water configurations and corresponding adsorption energy on O-$(002)Zn_{Vo(3C)}$ (carried out by Dr. Jin Qu).

Notice that the calculated chemical shift of TMP on $(100)Zn_{3C}$ (-41.97 ppm) matches well with experimental data from the rod sample with preferentially exposed (100) facets (-42.9 ppm). As (002) polar facets dominate in the plate sample and the

population of O-(002)$Zn_{Vo(3C)}$ is minor (as it is mostly converted into O-(002)Zn-OH with strongest E_{ad} = -2.46 eV, **Figure 4-11**), the experimentally observed resonance at around -48 ppm (Site II) can be attributed to the interaction between TMP and Zn-(002)Zn_{3C} according to the corresponding calculated adsorption energy. The signal at -55 ppm of Site III is assigned to the adsorption of TMP on Zn-(002)Zn-OH and O-(002)Zn-OH which show comparable adsorption energies. The signal at -61 ppm of Site IV can be assigned to weak adsorption of TMP on non-polar (100)Zn-OH or related surfaces [26].

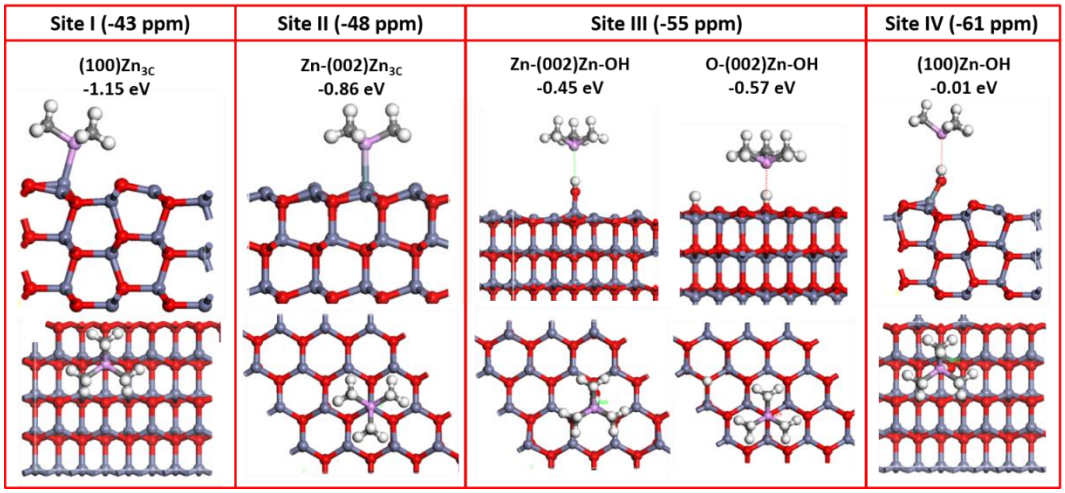

Figure 4-12. Schematic illustrations of molecular interaction and calculated adsorption energy between TMP and various surface features: (100)Zn_{3C}, Zn-(002)Zn_{3C}, Zn/O-(002)Zn-OH and (100)Zn-OH (carried out by Dr. Jin Qu).

Schematic illustrations of molecular interaction of these four sites (i.e. Site I, II, III and IV) are summarized in **Figure 4-12**. It is noted that the calculated adsorption energy of TMP on nonpolar (100)Zn-OH is only -0.01 eV, while this energy becomes 50 times higher (~0.5 eV) when the TMP interacts with a hydroxyl group on polar surface (compare Zn-(002)Zn-OH (-0.45 eV) and O-(002)Zn-OH (-0.57 eV)). According to both experimental and theoretical data, the interaction between hydroxyl protons and TMP seems highly dependent on the surface polarity of the ZnO facet. This preferential

adsorption of molecules on a specific facet has been observed and is attributed to the difference in surface energy and surface atomic arrangement between facets [31,33].

4.3.4. ^{1}H MAS NMR study of proton on polar and nonpolar surface

Solid-state ^{1}H MAS NMR was used to probe the electron density of the hydroxyl protons. As shown in **Figure 4-13**, both plate and rod samples show a resonance peak at 4.8 ppm and two signals at smaller shift values between 0-2 ppm. Probing hydrogen in ZnO nanorods using solid-state ^{1}H MAS NMR, Wang et al. assigned the peak at 4.8 ppm to a strongly bonded proton in defect sites, as it was observed even after heating to 773 K, while the multiple chemical shifts between 0-2 ppm were assigned to water or surface hydroxyl groups, since they could be mostly removed upon heating to 573 K. removed upon heating [34]. Accordingly, our chemical shift at 4.8 ppm comes from a hydroxyl proton on a polar surface, while the other two signals arise either from hydroxyl protons on nonpolar surface or physisorbed water **(Figure 4-13)**. The simultaneous decrease in relative intensity of the peak at 4.8 ppm and increase of the peak between 0-2 ppm suggests an increase in the nonpolar surface at the expense of polar surface when the morphology is changed from plate to rod, which is in good agreement with the results obtained from ^{31}P MAS NMR.

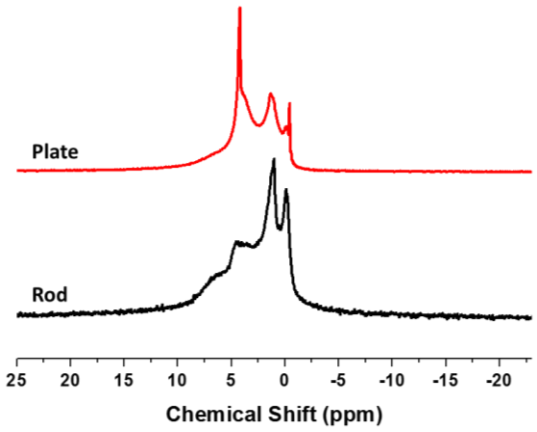

Figure 4-13. Solid-state ^{1}H MAS NMR spectra of ZnO plate and rod.

4.3.5. The relation between surface features and the configuration of adsorbed-TMP

By combining the information from **Figure 4-5** and **Figure 4-12**, the relation between surface features and the configuration of adsorbed-TMP can be determined and several remarks made: (1) The TMP molecule binds to the (100) facet of the rod sample, giving a dominant chemical shift at -43 ppm (Site I); (2) For TMP adsorption on ZnO crystallites (i.e. plate or rod in this study), Site II (-48 ppm, Zn-(002)Zn_{3C}) appears to link with Site III (-55 ppm, Zn-(002)Zn-OH and O-(002)Zn-OH) with an area/intensity ratio of 1.3, indicating they come from the exposure of both Zn-/O-terminated polar surfaces; (3) For the polycrystalline powder, Site II (-48 ppm) comes from the adsorption of the TMP molecule on fully exposed Zn ions at particle edges or corners, and is similar to the exposed zinc ion on polar Zn-(002)Zn_{3C} sites **(Figure 4-12)**. However, the peak intensity of Site III is remarkably low with an area/intensity ratio of 0.3, indicating TMP adsorption in this case does not adsorb on a polar surface. Compared to the low intensity of Site III (-55 ppm), the strong signal at Site IV (-61 ppm) in the powder sample also supports our discovery that the interaction between hydroxyl protons and TMP is affected by surface polarity; (4) For single-crystalline ZnO, the ratio of the peak area of Site II (-48 ppm) and Site I (-43 ppm) can act as an index to evaluate the percentage of exposed polar surface of the sample. For instance, the ratio for the plate sample is 7.25, which is 15 times more than that of rod sample (only 0.45). According to points (1) to (4), this technique (i.e. using TMP to probe crystal facets) can thus be a potential surface probe that not only provides quantitative information of acid sites, but is also as a powerful tool to evaluate their distribution on various exposed oxide facets.

4.3.6. Calculation of V_o concentration on ZnO O-(002) facet

To estimate the V_o concentration on the surface of these nanosize ZnO samples, we have to invoke some fundamental data derived from previous studies on the ZnO O-(002) facet. The high affinity of protons for 3-fold coordinated oxygen on the ZnO O-(002) surface has been reported by Diebold et al. [35]. By using STM and scanning tunneling spectroscopy (STS), they found that this surface is always saturated with hydrogen even under UHV conditions due to absence of metallization of this surface. On the other hand, Wöll's group studied the saturation coverage of protons as a function of temperature on ZnO O-(002) by Helium atom scattering (HAS) using "H_2O adsorption probability measurement" [36]. They showed that the saturation coverage of protons on O-(002) at 300 K is around 0.8 ML (full saturation of protons is equal to 1 ML at temperatures below 200 K), while this value decreases to 0.2 ML when the temperature increases to 600 K. The decrease of the saturation coverage of protons was attributed to the generation of V_o by recombination of H-atoms with OH-species (i.e. thermal desorption of water). Accordingly, we can therefore calculate the V_o concentration on the plate O-(002) at room temperature by using the amount of OH on the polar surfaces determined from the NMR data.

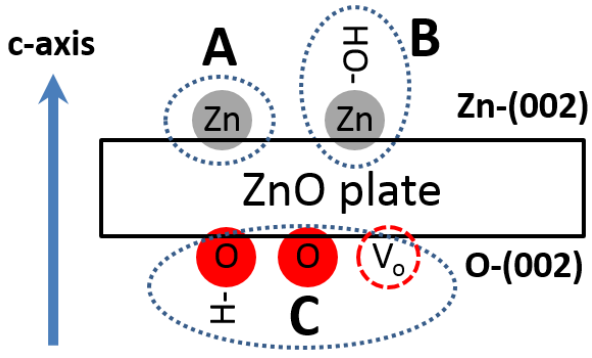

Figure 4-14. Schematic illustration of surface features on Zn-/O-(002) facets.

The saturation coverage of protons (1 ML) on plate O-(002) was firstly calculated. We

assume the number of exposed Zinc ion and the number of Zn-OH group on Zn-(002) are A and B. Accordingly, the total number of Zinc ion on Zn-(002) facet is A + B and this number is independent of temperature and moisture. For a perfect plate, the number of oxygen site on O-(002) facet (denoted as C) should equal to A + B. Since Wöll's group [36] showed that the saturation coverage of proton on O-(002) at 300 K is around 0.8 ML, the total number of hydroxyl group on both surfaces is therefore: B + 0.8C. From solid-state ^{31}P MAS NMR spectra measured at room temperature **(Figure 4-5)**, A can be obtained from the number of TMP-Zn adduct formed at Site II (-48 ppm) (i.e. 13.45 μmol of adsorbed TMP/g) and the total number of hydroxyl group on polar surfaces (B + 0.8C) can be obtained from Site III (- 55 ppm) (i.e. 18.41 μmol of adsorbed TMP/g). The corresponding equations are shown below (*adsorbed TMP molecules in μmol/g):

Number of exposed Zinc ion on Zn-(002): A

Number of Zn-OH group on Zn-(002): B

Total number of Zinc site on Zn-(002): A + B

Total number of Oxygen site on O-(002): C

For plate sample (BET surface area: 11.93 m^2/g):
*adsorbed TMP molecules in μmol/g from **Figure 4-5**
A = 13.45* (~ 8.07×10^{18} counts/g or 6.76×10^{17} counts/m^2)
A + B = C (for a perfect plate) - (1)
B + 0.8C = 18.41* - (2)
by solving equation (1) & (2)
B = 4.25* (~ 2.55×10^{18} counts/g or 2.14×10^{17} counts/m^2)
C (1 ML) = 17.7* (~ 1.06×10^{19} counts/g or 8.89×10^{17} counts/m^2)
Therefore, at 300 K on O-(002) surface:
[O] & [V_o] (0.1ML): 1.06×10^{18} counts/g or 8.89×10^{16} counts/m^2
We can also derive the concentration of OH group on Zn-(002) and O-(002) at 300 K:
O-(002)Zn-OH: 8.48×10^{18} counts/g (77% of peak -55 ppm, 0.8ML)
Zn-(002)Zn-OH: 2.55×10^{18} counts/g (23% of peak -55 ppm)

For rod sample (BET surface area: 9.73 m^2/g):

A = 7.27* (~ 4.36×10^{18} counts/g or 4.48×10^{17} counts/m^2)

B + 0.8C = 18.41*

Since A + B = C

B = 1.48* (~ 8.9×10^{17} counts/g or 9.15×10^{16} counts/m^2)

C = 8.75* (~ 5.25×10^{18} counts/g or 5.40×10^{17} counts/m^2)

Therefore, at 300 K on O-(002) surface:

[OH] (0.8C): 4.20×10^{18} counts/g or 4.32×10^{17} counts/m^2

[O]& [V_o] (0.1C): 5.25×10^{17} counts/g or 5.40×10^{16} counts/m^2

For powder sample (BET surface area: 5.36 m^2/g):

A = 1.85* (~ 1.11×10^{18} counts/g or 2.07×10^{17} counts/m^2, calculated using Site III/Site II = 1.3)

B + 0.8C = 2.4*

Since A + B = C

B = 0.48* (~ 2.9×10^{17} counts/g or 5.41×10^{16} counts/m^2)

C = 2.33* (~ 1.4×10^{18} counts/g or 2.61×10^{17} counts/m^2)

Therefore, at 300 K on O-(002) surface:

[OH] (0.8C): 1.12×10^{18} counts/g or 2.09×10^{17} counts/m^2

[O]& [V_o] (0.1C): 1.4×10^{17} counts/g or 2.61×10^{16} counts/m^2

The [O] and Zn_{4c} of both polar and non-polar surfaces can be calculated based on surface stiochiometry.

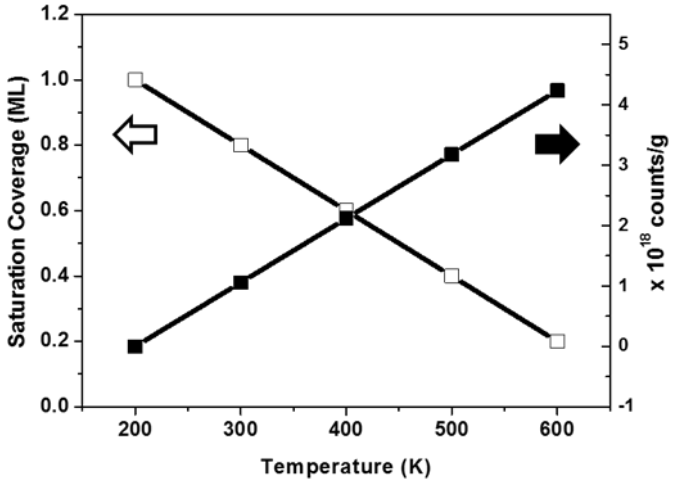

Figure 4-15. The saturation coverage of proton (monolayer, ML) on O-(002) surface from literature [36] and the calculated V_o concentration on plate O-(002) surface in this study in counts per gram as a function of temperature from 200 K to 600 K.

	saturation coverage of H_2O (ML)	V_o on plate O-(002) (counts/g)
200 K	1.0	0
300 K	0.8	1.06×10^{18} (0.1 ML)
400 K	0.6	2.12×10^{18} (0.2 ML)
500 K	0.4	3.18×10^{18} (0.3 ML)
600 K	0.2	4.24×10^{18} (0.4 ML)

Table 4-3. The saturation coverage of H_2O (monolayer, ML) on O-(002) surface from literature [36] and the calculated V_o on plate O-(002) surface in this study in counts per gram as a function of temperature from 200 K to 600 K.

Since the coverage of OH is inversely proportional to the temperature [36] **(Figure 4-15)** and the generation of V_o is accompanied by thermal desorption of water, the V_o concentration on O-(002) can thus be calculated as a function of temperature. As shown in **Table 4-3**, the V_o concentration on plate O-(002) at room temperature was determined to be 1.06×10^{18} counts/g and this value increases to 4.24×10^{18} counts/g when the temperature is raised to 600 K. It should be noted that this is the first time the concentration of V_o at room temperature on a specific facet of ZnO has been derived from this new mapping technique. We can also calculate the number of TMP molecules adsorbed on Zn-(002)Zn-OH (2.55×10^{18} counts/g, 23%) and O-(002)Zn-OH (8.48×10^{18} counts/g, 77%), both of which contribute to the intensity of the peak at -55 ppm **(Figure 4-5)**. The quantification and the distribution of various surface features on different facets of ZnO plate and rod at 300 K are summarized in **Figure 4-16**.

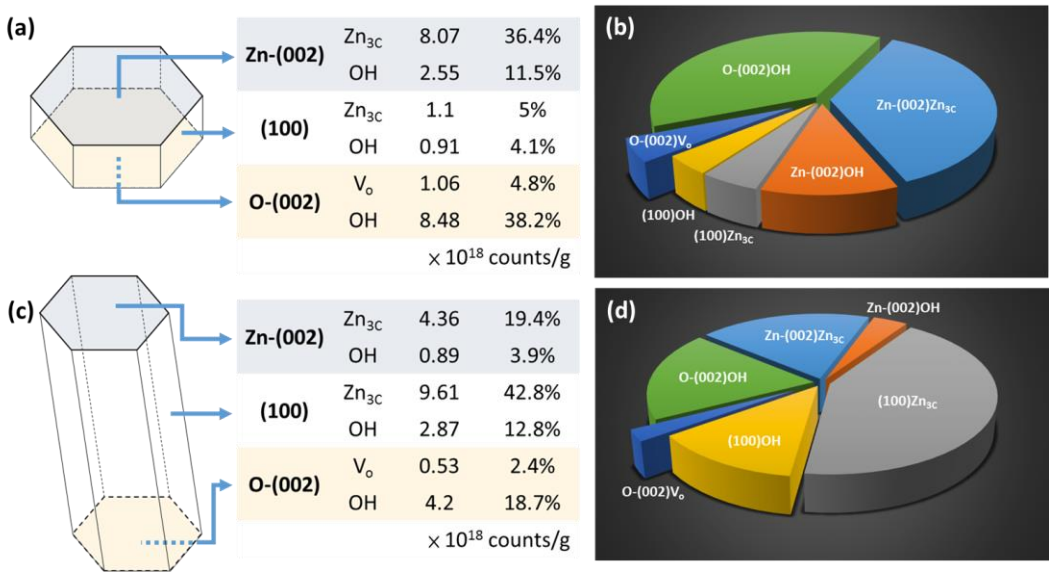

Figure 4-16. The distribution, concentration and percentage of surface features of NMR detected species on various ZnO facets of a, b) plate and c, d) rod. The concentrations of Zn_{4C} and [O] were not included.

4.3.7. Applicability of surface fingerprint to other nano-ZnO samples

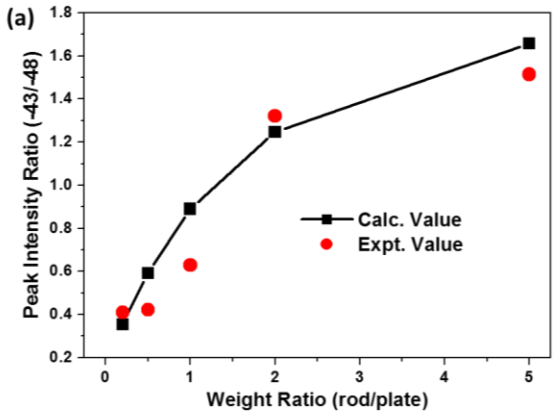

Mixture	Rod (mg)	Plate (mg)	Weight % (Rod/Plate)	Calc. Int. Ratio (-43/-48)	Expt. Int. Ratio (-43/-48)
I	25	125	0.2	0.355	0.409
II	50	100	0.5	0.5925	0.422
III	75	75	1	0.89	0.628
IV	100	50	2	1.248	1.32
V	125	25	5	1.658	1.514

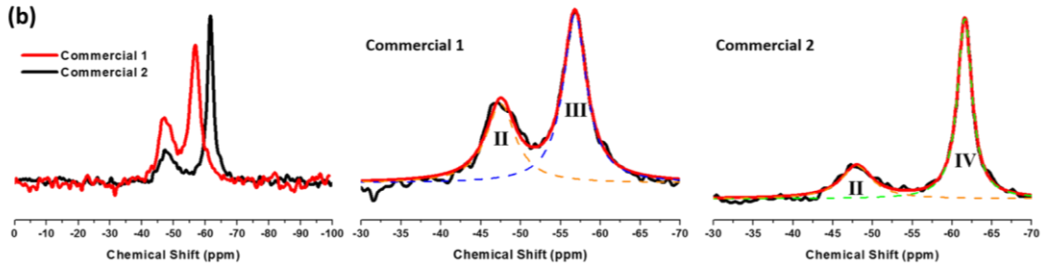

ZnO	Site II			Site III			Site IV		
	ppm	Area(%)	TMP*	ppm	Area(%)	TMP*	ppm	Area(%)	TMP*
Commercial 1	-48.2	35.8%	24	-56.6	64.2%	43	-	-	-
Commerical 2	-47.3	26.3%	5	-	-	-	-61.6	73.7%	14

Figure 4-17. a) The mixtures of plate/rod and the corresponding intensity ratio of peak -43 ppm and -48 ppm. Calc. value: using as-measured intensity ratio (-43/-48) of single

component-plate/-rod sample to predict the signal intensity of their mixtures; Expt. value: the intensity ratio obtained from ^{31}P NMR spectrum of TMP-adsorbed mixture. b) ^{31}P MAS NMR spectra of two ZnO commercial samples (TMP adsorbed) and the corresponding data of each deconvoluted peak. *Adsorbed TMP molecules in μmol/g.

In order to verify whether this surface fingerprint can be used to assess the degree of exposed facets for a given ZnO sample, we prepared several mixtures with different ratios of the rod and the plate samples and analyzed them using the ratio of intensities at -43 ppm and -48 ppm. As shown in **Figure 4-17a**, except a small deviation in mixture II and III, the experimental data match the calculated values very well. The ZnO facet fingerprint developed here is also found to be applicable to commercially available nano-ZnO samples. The deconvoluted ^{31}P MAS NMR spectra of two such commercially available ZnO samples following TMP-adsorption are shown in **Figure 4-17b**. From the spectra it can be seen that commercial sample 1 is similar to ZnO plate **(Figure 4-5)** with a high Site III/Site II ratio (~1.8), indicating crystalline particles with a significant amount of exposed Zn-/O-terminated polar surfaces. Commercial sample 2, on the other hand, has a dominant ^{31}P resonance at -61 ppm similar to our powder sample and is expected to be polycrystalline with a high coverage of hydroxyl groups. The large degree of difference in crystallinity of the two commercial samples is further supported by HRTEM and electron diffraction studies **(Figure 4-18)**.

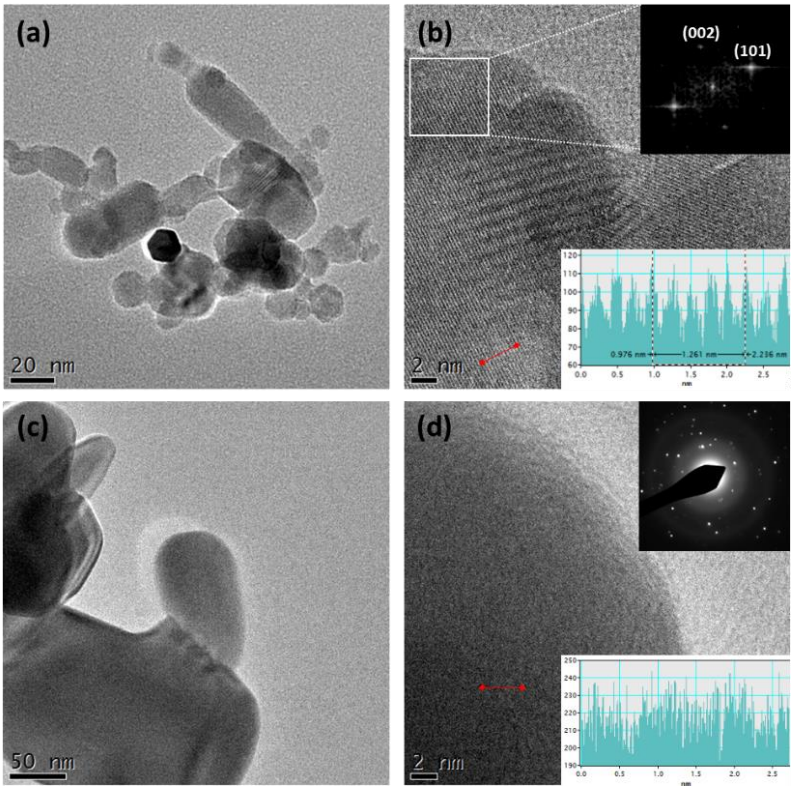

Figure 4-18. TEM and HRTEM images of two commercial ZnO samples a, b) commercial 1 and c, d) commercial 2. Inset: corresponding electron diffraction (ED) pattern. Five lattice fringes of commercial 1 ZnO NP were measured to be 1.261 nm in length **(Figure 4-18b inset)**. The lattice spacing was calculated to be 0.252 nm, which corresponds to the (101) plane of ZnO structure. However, for commercial 2 ZnO NP, no periodic lattice fringe was observed **(Figure 4-18d inset)**.

4.4. Chapter conclusion

Herein, using ZnO as a model material, we report TMP-assisted surface mapping of oxide nanoparticles and crystallites using ^{31}P solid-state NMR and show that it can provide comprehensive information (both qualitative and quantitative) on the surface features of various facets. Given that each facet possesses distinctive intrinsic energy, both concentration and chemical state of surface cations (Zn_{3C}, H) differ from facet to facet. As TMP, an electron donor molecule (Lewis base, LB), can form a stable TMP-LA complex with the exposed cation (Lewis acid, LA), coordination of the P atom to the LA centers from different host facets is expected to give different strengths and thus different NMR chemical shifts. The stronger interaction between TMP and surface LA pushes ^{31}P chemical shift ($\delta^{31}P$) toward downfield (i.e. zero ppm). To this end, single-crystalline plate- and rod-shaped ZnO nanoparticles containing preferentially exposed (002) and (100) facets, respectively and polycrystalline ZnO powder, were prepared to study the correlation between $\delta^{31}P$ and the adsorption configurations of TMP on various ZnO facets.

By combining both NMR and DFT calculation results, the relation between surface cations and the TMP adsorption configuration can then be determined. Several remarks have been made: (1) A TMP molecule needs to tilt an angle to bind to Zn_{3C} on the (100) facet giving the most positive chemical shift at -43 ppm (Site I); (2) A slightly negative chemical shift (-48 ppm, Site II) was obtained for a TMP molecule head-to-head binds to Zn_{3C} on the Zn-(002) facet; (3) 6 ppm difference in chemical shift was found for the adsorption of TMP on hydroxyl proton between polar (-55 ppm, Site III) and nonpolar (-61 ppm, Site IV) surface; (4) The area/intensity ratio of Site III to Site II can be used to evaluate the crystallinity of ZnO particles. This ratio is always larger than 1 for single-crystalline ZnO (~1.3 in this study) suggesting the exposure of both Zn-/O-

terminated polar surfaces, while this ratio is far below 1 for polycrystalline ZnO (~0.3 in this study) with no exposure of high energy polar surface. (5) For single-crystalline ZnO, the ratio of the peak area of Site II and Site I can work as an index to evaluate the percentage of exposed polar surface of the sample. For instance, the ratio for the plate sample is 7.25, which is 15 times more than that of rod sample (only 0.45). According to points (1) to (5), this technique (i.e. using TMP to probe crystal facets) can thus be a potential surface probe that not only provides quantitative information of acid sites, but is also as a powerful tool to evaluate their distribution on various exposed oxide facets.

As like XRD giving structural fingerprint on crystal materials, this technique has been demonstrated capable of providing unprecedented information surface fingerprint from a single deconvoluted ^{31}P NMR spectrum. Information such as the nature, binding strength and concentration of active sites on the various facets can be further extracted. As a result, this technique, together with the as-built up ZnO facet fingerprint, not only provides quantitative information on surface features but also guides the rational design of facet-dependent nanocatalysis for a given sample.

References:

[1] M. H. Huang, S. Rej, C.-Y. Chiu, *Small* **2015**, *11*, 2716−2726.

[2] S. Rej, H.-J. Wang, M.-X. Huang, S.-C. Hsu, C.-S. Tan, F.-C. Lin, J.-S. Huang, M. H. Huang, *Nanoscale* **2015**, *7*, 11135−11141.

[3] H. Dixit, W. Zhou, J. C. Idrobo, J. Nanda, V. R. Cooper, *ACS Nano* **2014**, *8*, 12710−12716.

[4] C.-S. Tan, S.-C. Hsu, W.-H. Ke, L.-J. Chen, M.-H. Huang, *Nano Lett.* **2015**, *15*, 2155−2160.

[5] B. Zhang, D. Wang, Y. Hou, S. Yang, X. H. Yang, J. H. Zhong, J. Liu, H. F. Wang, P. Hu, H. Y. Zhao, H. G. Yang, *Sci. Rep*. **2013**, *3*, 1836−1843.

[6] C. Li, C. Koenigsmann, W. Ding, B. Rudshteyn, K. R. Yang, K. P. Regan, S. J. Konezny, V. S. Batista, G. W. Brudvig, C. A. Schmuttenmaer, J.-H. Kim, *J. Am. Chem. Soc.* **2015**, *137*, 1520−1529.

[7] W. Chrzanowski, A. Wieckowski, *Langmuir* **1998**, *14*, 1967−1970.

[8] N. Tian, Z. Y. Zhou, S. G. Sun, Y. Ding, Z. L. Wang, *Science* **2007**, *316*, 732−735.

[9] B. M. Choudary, R. S. Mulukutla, K. J. Klabunde, *J. Am. Chem. Soc.* **2003**, *125*, 2020−2021.

[10] D. Jézéquel, J. Guenot, N. Jouini, F. Fiévet, *J. Mater. Res.* **1995**, *10*, 77–83.

[11] J. Zhang, L. Sun, J. Yin, H. Su, C. Liao, C. Yan, *Chem. Mater.* **2002**, *14*, 4172–4177.

[12] L. Guo, Y. L. Ji, H. Xu, P. Simon, Z. Wu, *J. Am. Chem. Soc.* **2002**, *124*, 14864–14865.

[13] Z. W. Pan, Z. R. Dai, Z. L. Wang, *Science* **2001**, *291*, 1947–1949.

[14] E. S. Jang, J. H. Won, S.-J. Hwang, J. H. Choy, *Adv. Mater.* **2006**, *18*, 3309–3312.

[15] G. R. Li, T. Hu, G. L. Pan, T. Y. Yan, X. P. Gao, H. Y. Zhu, *J. Phys. Chem. C* **2008**, *112*, 11859–11864.

[16] A. McLaren, T. Valdes-Solis, G. Li, S. C. Tsang, *J. Am. Chem. Soc.* **2009**, *131*, 12540–12541.

[17] F. Liao, Y. Huang, J. Ge, W. Zheng, K. Tedsree, P. Collier, X. Hong, S. C. Tsang, *Angew. Chem. Int. Ed.* **2011**, *50*, 2162–2165.

[18] M. Behrens, F. Studt, I. Kasatkin, S. Kühl, M. Hävecker, F. Abild-Pedersen, S. Zander, F. Girgsdies, P. Kurr, B.-L. Kniep, M. Tovar, R. W. Fischer, J. K. Nørskov, R. Schlögl, *Science* **2012**, *336*, 893–897.

[19] Y. Qin, X. Wang, Z. L. Wang, *Nature* **2008**, *451*, 809–813.

[20] L. Wang, Y. Kang, X. Liu, S. Zhang, W. Huang, S. Wang, *Sensor Actuat B-Chem.* **2012**, *162*, 237–243.

[21] S. B. Zhang, S. H. Wei, A. Zunger, *Phys. Rev. B* **2001**, *63*, 075205.

[22] J. Q. Hu, Y. Bando, *Appl. Phys. Lett.* **2003**, *82*, 1401–1403.

[23] N. Y. Garces, N. C. Giles, L. E. Halliburton, G. Cantwell, D. B. Eason, D. C. Reynolds, D. C. Look, *Appl. Phys. Lett.* **2002**, *80*, 1334–1341.

[24] A. B. Djurišić, W. C. H. Choy, V. A. L. Roy, Y. H. Leung, C. Y. Kwong, K. W. Cheah, T. K. G. Rao, W. K. Chan, H. F. Lui, C. Surya, *Adv. Funct. Mater.* **2004**, *14*, 856–864.

[25] K. Tedsree, C. W. A. Chan, S. Jones, Q. Cuan, W.-K. Li, X.-Q. Gong, S. C. E. Tsang, *Science* **2011**, *332*, 224–228.

[26] A. Zheng, S.-J. Huang, S.-B. Liu, F. Deng, *Phys. Chem. Chem. Phys.* **2011**, *13*, 14889–14901.

[27] A. Zheng, S.-J. Huang, Q. Wang, H. Zhang, F. Deng, S.-B. Liu, *Chinese J. Catal.* **2013**, *34*, 436–491.

[28] A. Zheng, F. Deng, S.-B. Liu, Acidity Characterization of Solid Acid Catalysts by Solid-State 31P NMR of Adsorbed Phosphorus-Containing Probe Molecules. *Annual reports on NMR Spectroscopy*; Elsevier 2014; 81, 47–108.

[29] C. Tian, Q. Zhang, A. Wu, M. Jiang, Z. Liang, B. Jiang, H. Fu, *Chem. Commun.* **2012**, *48*, 2858–2860.

[30] A. B. Djurišić, X. Chen, Y. H. Leung, A. M. C. Ng, A. M. C. *J. Mater. Chem.* **2012**, *22*, 6526–6535.

[31] Y. Yin, A. P. Alivisatos, *Nature*, **2005**, *437*, 664–670.

[32] Y. Chu, Z. Yu, A. Zheng, H. Fang, H. Zhang, S.-J. Huang, S.-B. Liu, F. Deng, F. *J. Phys. Chem. C* **2011**, *115*, 7660–7667.

[33] H. Zhang, J. Sun, V. L. Dagle, B. Halevi, A. K. Datye, Y. Wang, *ACS Catal.* **2014**, *4*, 2379−2386.

[34] L.-Q. Wang, G. J. Exarhos, C. F. Windisch, C. Yao, L. R. Pederson, X.-D. Zhou, *Appl. Phys. Lett.* **2007**, *90*, 173115.

[35] U. Diebold, L. V. Koplitz, O. Dulub, *Appl. Surf. Sci.* **2004**, *237*, 336–342.

[36] M. Kunat, S. G. Girol, U. Burghaus, C. Wöll, *J. Phys. Chem. B* **2003**, *107*, 14350–14356.

Chapter 5 ZnO: Comparing chemical probe-assisted NMR with both PL and EPR as a characterization tool in facet-specific photocatalysis

5.1. Chapter overview

Photoluminescence (PL) and electron paramagnetic resonance (EPR) are the two most commonly used techniques to evaluate surface oxygen vacancy ($V_{o\ surface}$) on photo-active transition metal oxides. However, it is demonstrated that there are shortcomings of them in characterizing facet-dependent catalysis. Here, by using chemical adsorption probe of ^{31}P-containing molecule, the distribution/concentration of $V_{o\ surface}$ as well as other surface features (hydroxyl groups) of ZnO can be obtained by ^{31}P MAS NMR. This facet-specific technique not only makes cross-literature comparison feasible but also provides more comprehensive information to lead to further understanding of photocatalytic mechanism. Based on this technique a new mechanism for photocatalytic •OH radical generation from direct surface-OH oxidation is revealed, which has important implications regarding the safety of using nano oxides in personal care products.

5.2. Introduction

Over the past decade, single-crystalline transition metal oxide nanoparticles have been widely employed in fields such as optics [1,2], electronic devices [3,4], solar cell [5,6] and heterogeneous catalysis [7-9] due to the enhanced performance with preferential exposure of a specific crystal facet. In particular, in the field of heterogeneous catalysis, which involves the breakage/formation of chemical bonds between reactant and product,

is highly related to the coordination environment of the surface active atoms. It is therefore generally accepted that catalysis can take place differently not only on chemical composition and size of catalyst but on different crystallographic faces; hence many reactions are sensitive to the surface structure of nanocatalyst [10]. These considerations add exciting variables in tailoring the properties of nanocatalysts for a wide range of catalytic reactions. For example, tailoring ZnO NPs for shape and size has been receiving a considerable attention because of superior performance in photocatalysis [11-17], methanol formation [18,19], optoelectronics [20-22] and gas sensing [23], etc. A correlation of these properties to the surface concentration of oxygen vacancy ($V_{o\ surface}$) is envisaged but no universal accepted technique for the defect measurement is available.

To probe the bulk defect sites, photoluminescence spectroscopy (PL) at short excitation wavelength has been attempted. Transition metal oxide semiconductors including ZnO can capture the photons from the excitation source with energy equal to or greater than their band gap energy. The photons are then absorbed by the oxide semiconductor nanocrystal causing the generation of photo-excited electrons and holes in the conduction and valence bands, respectively. The excited electron-hole pairs, known as excitons, are then subject to recombination in particular on the defect centers to give trap-state luminescence. As $V_{o\ bulk}$ is linked with the green-yellow luminescence of ZnO, Li *et al.* firstly extended such correlation to $V_{o\ surface}$ concentration on polar ZnO facet monitored by the PL spectroscopy [13]. Since then, PL has become commonly used to evaluate the exposure of polar surface/$V_{o\ surface}$ concentration of ZnO NPs. The comparison of their PL or corresponding deconvoluted PL signal have also been adopted to study the role of $V_{o\ surface}$ in photocatalysis [13-17] or optical/electronics [21,22].

Electron paramagnetic resonance (EPR) is the other technique widely adopted to evaluate $V_{o\ surface}$ of ZnO NPs by monitoring the transition of unpaired electron spins [14,15,22,24-26]. Its signal at about g=2.00 has been commonly assigned to the unpaired electrons trapped in $V_{o\ surface}$ via adsorbed dioxygen (O_2^-) or other low coordinated defect sites. As a quantitative value (spin counts/gram of sample) is obtainable by the integration of this signal, the concentration of trapped unpaired electron can be used to gauge the $V_{o\ surface}$ concentration of an oxide crystallite.

Very recently, by monitoring the nuclear spins, solid state ^{31}P MAS NMR can be used to map different surfaces on ZnO samples with the assistance of trimethylphosphine (TMP) as a chemical probe [27]. It is demonstrated for the first time that the chemical shift values of adsorbed TMP molecule can reflect the concentration and distribution of V_o and OH group on various facets from a single deconvoluted ^{31}P NMR spectrum.

Here we report the direct comparison of the three above techniques (PL, EPR and NMR) in correlating the photocatalytic decomposition activity of methylene blue of ZnO NPs for the study of facet-specific photocatalysis. We have showed that the commonly used PL and EPR techniques can only generate limited information but with a number of shortcomings. Despite the current wide use of the two techniques, it alerts a great caution in the information obtained. In contrast, the NMR technique in combination of chemical probe could generate more comprehensive information for facet-dependent photocatalysis over the oxide materials.

5.3. Results and discussion

5.3.1. TMP-assisted surface fingerprinting of ZnO by ^{31}P MAS NMR

In previous chapter NMR-active probe TMP was introduced to ZnO samples with different morphologies for the study of the distribution/concentration of surface features on various facets. As TMP, an electron donor molecule (Lewis base, LB), can form a stable adduct with the exposed cation of an oxide surface (Lewis acid, LA), the formation of a surface TMP-LA complex may be realized via coordination of the P atom to the LA center. It is shown that the ^{31}P chemical shift (δ^{31}P) of the surface TMP-LA complex is able to differentiate between surface cations (Zn^{2+} or H^{+}) on facets at high resolution, with various Lewis acidities, surface energies and steric arrangements due to the stronger surface LA site pushing δ^{31}P to downfield. As surface V_o [13-17] and OH [11,12] were regarded as the key parameters towards understanding of facet-specific catalysis, the concentrations derived from TMP-adsorbed ^{31}P NMR over ZnO plate, rod and powder are summarized in **Table 5-1** for the comparison with PL and EPR results. Notice that the OH concentrations on both polar and nonpolar surfaces of ZnO were directly measured from NMR spectra data as they exhibit different chemical shifts towards TMP molecule and the V_o values were derived from surface stoichiometry [27]. According to **Table 5-1**, the plate sample with preferential exposure of polar surface, as expected, gives the highest $V_{o\ surface}$ concentration which is two and seven times higher than rod and powder samples, respectively. This is attributed to higher surface area of plate to rod and powder **(Table 5-1)** and higher degree of V_o formation from intrinsic unstable oxygen repulsion of the O-terminated (002) [O-(002)] polar surface. As shown in previous chapter, the formation energy of $V_{o\ surface}$ is the lowest and hence $V_{o\ surface}$ is mostly populated on O-(002) among three facets.

Sample	BET (m^2/g)	Zn-(002)	O-(002)		[OH]* on nonpolar surface or coner/edge	[OH]* in total
		[OH]*	[OH]*	[$V_{o\ surface}$]*		
Plate	11.93	2.55	8.48	1.06	0.91	11.94
Rod	9.73	0.89	4.2	0.53	2.87	7.96
Powder	5.36	0.29	1.12	0.14	13.6	15.01

Table 5-1. The quantification and the distribution of OH and $V_{o\ surface}$ of ZnO plate, rod and powder at 300 K; Zn-(002): Zn-terminated (002) facet; O-(002): O-terminated (002) facet. *concentration in $\times 10^{18}$ counts/g

Around ~13% $V_{o\ surface}$ (cf. OH groups) on the O-(002) facet was measured under ambient conditions for both the single-crystalline plates and rods samples **(Table 5-1)** because of the high affinity of water molecules to $V_{o\ surface}$ sites with dissociative adsorption energy of -2.46 eV **(Figure 5-1)**, ~84% of O atoms on this facet are terminated with OH groups. However, defect regions such as surface steps, corners, edges, and ridges in polycrystalline powder also comprise many coordinatively unsaturated atoms but at even higher energies. These defect sites can be hydrolyzed more readily in the presence of water molecules, which results in the highest coverage of OH concentration on the powder despite its low surface area.

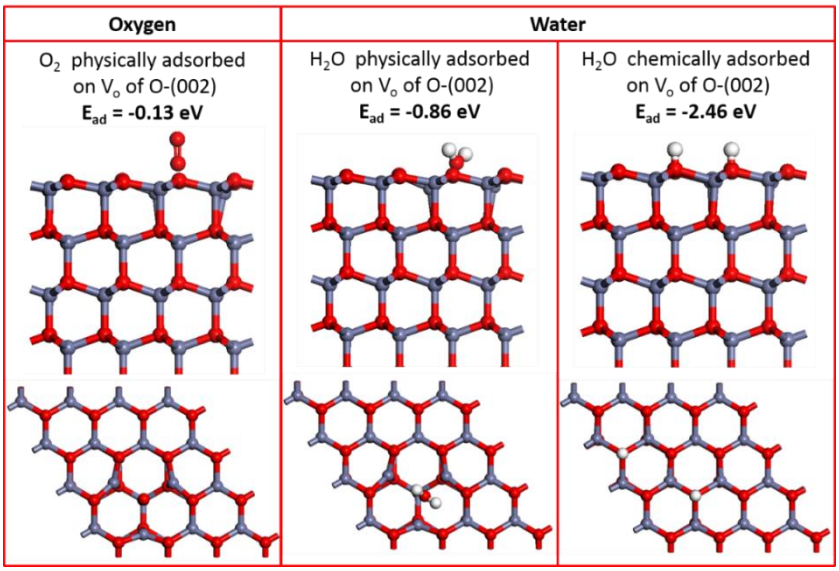

Figure 5-1. DFT calculations of oxygen/water configurations and corresponding adsorption energy on $V_{o\ surface}$ of O-(002) (carried out by Dr. Jin Qu).

5.3.2. PL study of ZnO with different morphologies

As PL emission is concerned with the emission from the recombination of excitons carriers, it has been commonly used to investigate the fate of photogenerated electrons and holes in semiconductor at the bulk level. The PL peaks of these three samples were acquired by this technique and are shown in **Figure 5-2a**. All three samples reveal a peak in UV region at 397 nm which corresponds to the band gap emission of ZnO. According to molecular bonding model, the conduction band is mainly composed of unfilled d-band of Zn^{2+} (four coordinated Zn_{4C} sites) and the valance band of filled p-band of O^{2-} [28,29]. The general broad peak with subpeaks at longer wavelength than corresponding band gap of 397 nm is due to the various emissions from the defect levels between the both bands. For classical assignment of bulk defects, the violet (421 nm) and blue (468 nm) emissions are attributed to the transitions from Zn_i and extended Zn_i (ex-Zn_i) (Zn interstitial-related defects) locating slightly below the conduction band-edge to the valance band, respectively [22]. While, the green (561 nm) and yellow (600 nm) regions represent the transitions from conduction band and Zn_i to deep levels ($V_{o\ bulk}$ of ~1 eV above valance band [22]), respectively. The interpretation of the broad

peak has recently been extended to cover the surface defects (i.e. $V_{o\ surface}$) that can be linked to facet-dependent properties depsite the fact that the PL is a bulk technique [13].

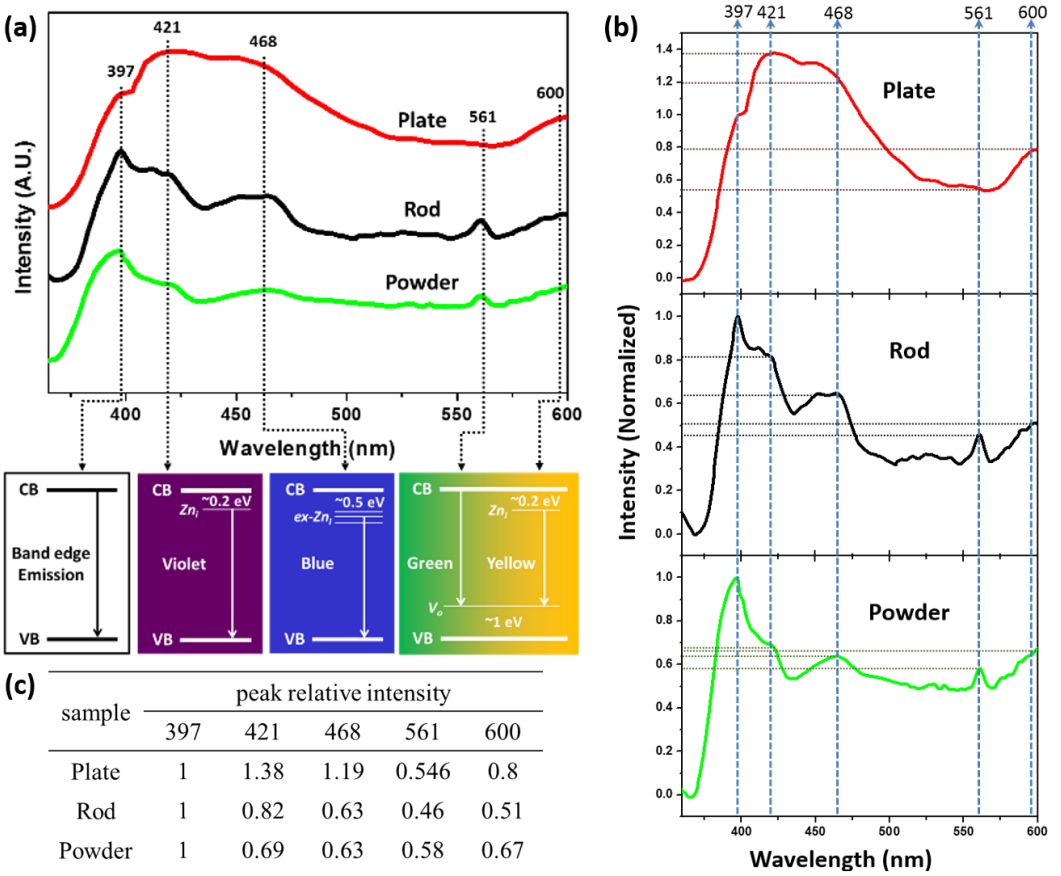

(c)

sample	peak relative intensity				
	397	421	468	561	600
Plate	1	1.38	1.19	0.546	0.8
Rod	1	0.82	0.63	0.46	0.51
Powder	1	0.69	0.63	0.58	0.67

Figure 5-2. a) original and b) normalized (excitonic emission 397 nm to 1) PL spectra of ZnO plate, rod and powder. c) Relative intensity of peaks of normalized PL.

In our case of ZnO nanoparticles, the intensity of the excitonic resounace peak due to the bulk phase (397 nm) is normalized to 1 **(Figure 5-2b&c)**. It is noted that the cumulative peak intensities at the broad peak due to defects are indeed proportional to their surface area being the highest for plate, then rod and powder samples. Thus, the unusal higher emissions at 421 nm (1.38) and 468 nm (1.19) of the plate sample with their ratios larger than unity as compared to band gap emission peak likely reflect the dominance of surface electronic states of low coordinated Zn_{3C} sites on the polar surface **(Table 5-2)** rather than from the insterstitial sites of Zn in the bulk. As similar to the

energy of bulk Zn_i and ex-Zn_i as according to our DFT calculation (see **Figure 4-6** in chapter 4), these low coordinated Zn_{3C} sites on surface shows higher electron density than bulk four-coordinated Zn^{2+} sites (Zn_{4C}) hence placing their modified sub-band below the conduction band. In the case of powder, the absolute and relative concentrations of surface cation and anion defects are the lowest, as the same finding as the NMR data **(Table 5-2)**. The emissive behavior in green-yellow region also agrees with this trend. Both rod and powder show a clear peak at 561 nm (cf. plate) indicating the domination of bulk Zn_{4C} in these two samples. The disappearance of this peak, together with, the increase of peak at 600 nm for plate clearly suggests the dominant concentrations of surface Zn_{3C} and $V_{o\ surface}$. Although these results are in line with the NMR, it is very difficult to derive truly surface information from this technique since the contributions of defects from the bulk and closely peak positions in spectrum do not allow easy identification and quantative treatments of the data.

counts/g ($\times 10^{18}$)	Site I (-43ppm) (100)Zn_{3C}	Site II (-48ppm) (002)Zn_{3C}	Site III (-55ppm) OH on (002)			Site IV (-61ppm) OH on nonpolar surface
			Zn-(002)	O-(002)		
			OH	OH	V_o	
Plate	1.10	8.07	2.55	8.48	1.06	0.91
Rod	9.61	4.36	0.89	4.2	0.53	2.87
Powder	0.98	1.11	0.29	1.12	0.14	13.6

Table 5-2. The quantification and the distribution of sites (i.e. Zn_{3C} and OH) on various facets of ZnO plate, rod and powder at 300 K derived in chapter 4. Powder sample has $\sim 4 \times 10^{18}$ counts of Zn_{3C} (-48 ppm) ions at particle edge/corner are not included in this table.

5.3.3. EPR study of ZnO with different morphologies

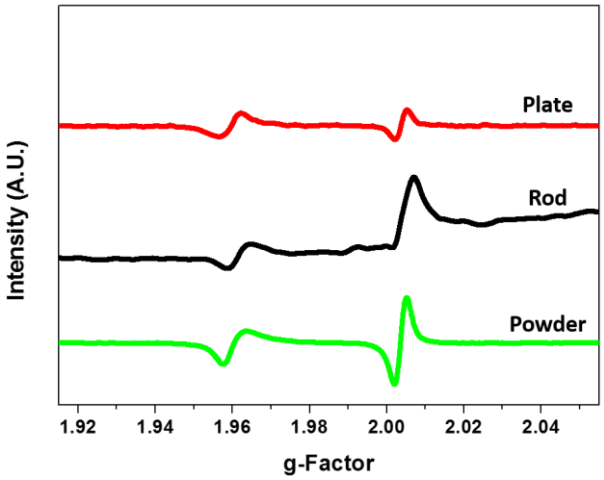

Figure 5-3. The EPR spectra of ZnO plate, rod and powder. These spectra were obtained by X-band CW EPR spectrometer (Bruker EMX) and the signal intensity versus electron spin number was obtained from the double integral of the spectrum.

EPR is another commonly reported technique to evaluate surface V_o. As shown in **Figure 5-3**, the EPR spectra of all three samples reveal two intense signals at about g=1.96 and g=2.00. The signal at g~2.00 is assigned to unpaired electrons from the semiconductor trapped in $V_{o\ surface}$ via adsorbed molecular oxygen from air or related species (O_2^-) and the signal at g~1.96 represents the unpaired electrons trapped by shallow donors or impurities [18,30]. **Table 5-3** shows the electron spin counts per gram of ZnO NPs at these two positions. The concentration of $V_{o\ surface}$ derived from NMR is also included for comparison. For single-crystallined plate and rod, both EPR and NMR data indicate that plate sample possesses twice $V_{o\ surface}$ concentration higher than that of rod. However, the actual $V_{o\ surface}$ concentration on all ZnO NPs measured by EPR (g~2.00) is hundred times lower than that of NMR.

sample (counts/g)	EPR		NMR
	g ~ 1.96	g ~ 2.0	$V_{o\ surface}$
Plate	2.3×10^{16}	8.2×10^{15}	10.6×10^{17}
Rod	1.2×10^{15}	4.5×10^{15}	5.3×10^{17}
Powder	3.2×10^{16}	10.8×10^{15}	1.4×10^{17}

Table 5-3. Comparison of apparent $V_{o\ surface}$ values of ZnO plate, rod and powder derived from EPR and NMR measurements.

With modern EPR and NMR equipments the accuracy of both techniques are expected to be comparable to each other and can reach to a single spin detection. As a result, the large discripancy cannot be accounted by the diffference in sensitivity of the equipments. On the other hand, considering the equation $O_2 + (V_{o\ surface}) + e^- \leftrightarrow O_2^-(V_{o\ surface})$ [24-26]. when O_2 molecule from air is trapped by the $V_{o\ surface}$ and an unpaired electron is then localised to form O_2^- which will give a strong EPR signal at g~2.00. Due to equilibrium limitation of the above equation, not all the V_o centers could take up O_2. The value will depend on equilibrium constant and applied partial pressure of oxygen molecule during the measurements. Our calculated adsorption energy of O_2 on $V_{o\ surface}$ is only -0.13 eV **(Figure 5-1)**, implying the small equilibrium constant. Along the same line, the adsorption of a H_2O molecule is -0.86 eV, which suggests that the measurement can be significantly interfered by the moisture from air after calcination. This high affinity of water molecule to $V_{o\ surface}$ on ZnO O-(002) was also observed experimentally by Diebold et al. using STM and scanning tunneling spectroscopy (STS) [31]. Wöll's and co-workers also showed that the saturation coverage of protons on O-(002) by water molecules at 300 K can be up to 0.8 ML. They then concluded that the adsorption of H_2O on $V_{o\ surface}$ is a favoured dissociative process at temperatures above 200 K [32]. Additionally, the EPR study over the polycrystalline powder sample implies apparently much higher $V_{o\ surface}$ concentration than the other two techniques, making an unexpected order of powder > plate > rod. Since powder sample is characterized

with the lowest surface area on a gram basis and perhaps associating with the lowest percentage of polar (002) surface. On the other hand, the polycrystalline powder is made up of small crystallites **(Figure 5-4)** and terminated with extremely rough surfaces comprising of high degrees of low coordinated step/ corner/ edge/ ridge sites which can also be the centre to trap unpaired electrons on these defective sites easily. As evidenced by Carter et al., in addition to $V_{o\ surface}$, surface nonvacancy metal ions can also stabilize O_2^- and give signal at g~2.00 [33,34]. Accordingly, the EPR signal cannot be all attributed to $V_{o\ surface}$ but partly to other nonvacancy defective sites. As a result, EPR fails to deliver quantitative result and is only applicable to deliver relative $V_{o\ surface}$ values in the comparison between single-crystalline particles.

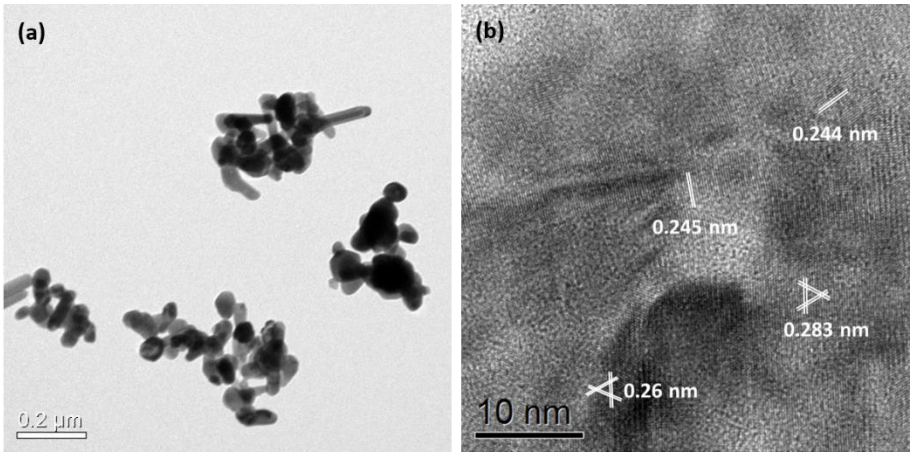

Figure 5-4. (a) Low and (b) high magnification TEM images of ZnO nanopowder. The polycrystalline property can be seen clearly from the mixture of lattices with spacing: 0.24, 0.26 and 0.28 nm corresponds to (101), (002) and (100) planes, respectively.

5.3.4. Facet-dependent photocatalytic activity

There is increasing evidence presented in the literature that photocatalytic activity is highly dependent on the particular facets exposed on transition metal oxide crystals. Using PL spectroscopy, Li et al. discovered a positive correlation between the polar faces exposed and the concentration of surface V_o of the samples [13]. The surface V_o of ZnO can act as potential wells to trap either one or two electrons, aiding electron-

hole pair separation and hence increasing the photocatalytic activity. For decades, a high V_o concentration/exposed polar face has been regarded as the main criterion for high photocatalytic activity [13-17]. However, as shown above, the surface V_o of ZnO is highly unstable when in contact with water, favoring for the formation of OH surface **(Figure 5-1)**.

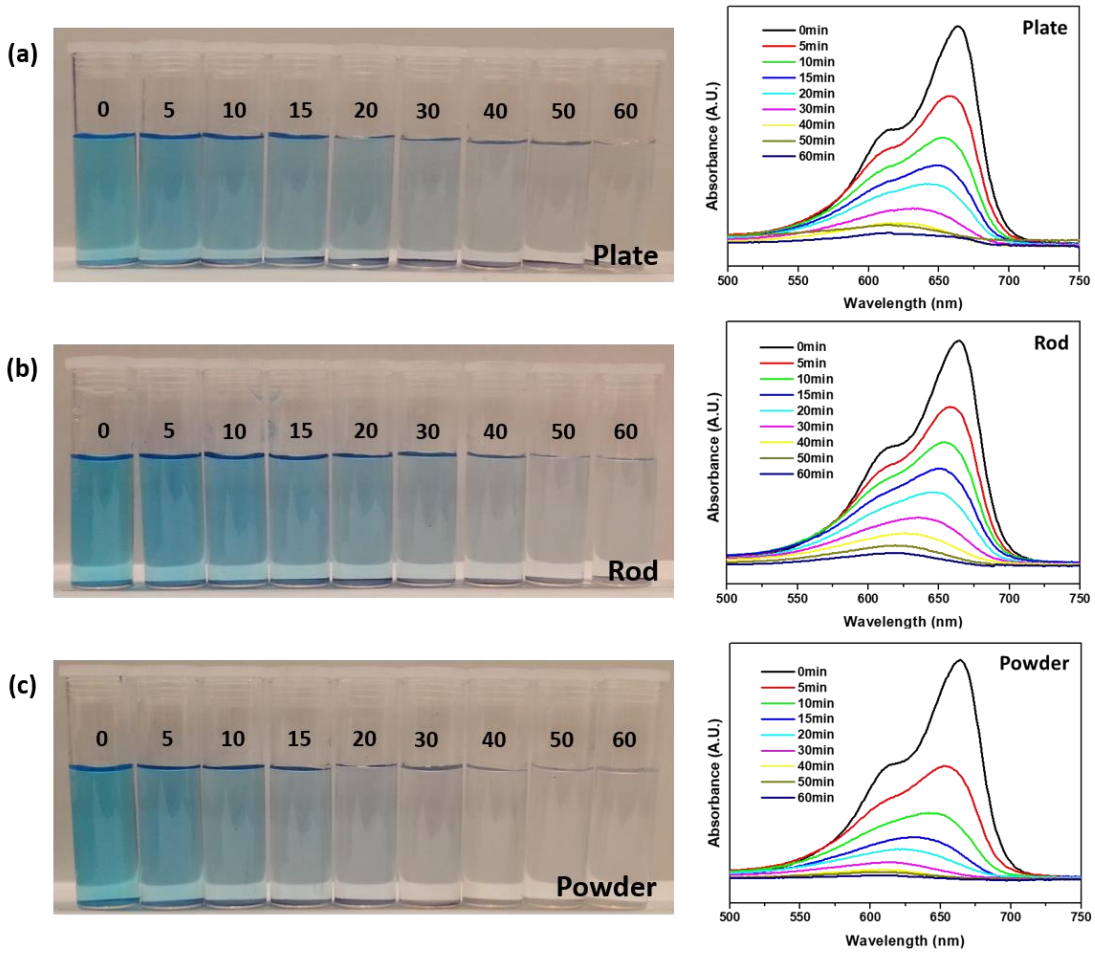

Figure 5-5. Solution appearance andnd UV/Vis absorption curves of methylene blue versus UV irradiation time (min) with ZnO a) plate, b) rod and c) powder.

Accordingly, photocatalytic decomposition of methylene blue (MB) in the presence of ZnO plate, rod and powder samples under ultraviolet irradiation was carried out to evaluate the facet-dependent catalytic activity **(Figure 5-5)**. This reaction, monitored at 664.5 nm, followed pseudo-first order reaction kinetics for all three samples **(Figure 5-6)**.

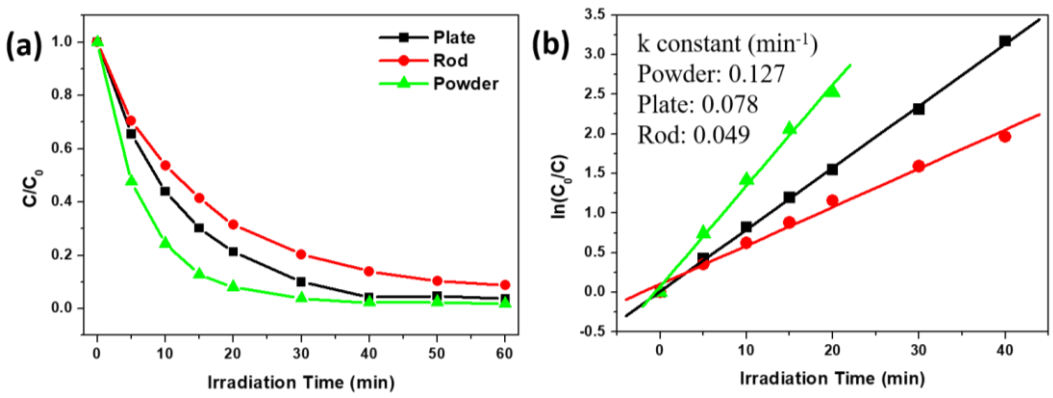

Figure 5-6. Photocatalytic activity plots of ZnO plate, rod and powder using (a) C/C_0 and (b) $\ln(C_0/C)$ versus UV irradiation time.

The k constants for photocatalytic decomposition **(Figure 5-6b)** are compiled with referencing to $V_{o\ surface}$ concentrations derived from EPR and NMR in **Figure 5-7**. The apparent higher rate constant of plate (k=0.078 min^{-1}) while the lower rate constant of rod (k=0.049 min^{-1}) can be clearly correlated with the $V_{o\ surface}$ concentrations derived by both the techniques. However, the polycrystalline powder with the lowest $V_{o\ surface}$ concentration/polar surface by NMR shows the highest reaction rate constant (k=0.127 min^{-1}). On the other hand, the correlation of the apparent $V_{o\ surface}$ evaluated by EPR is excellent. The BET measurement **(Table 5-1)** implies that their surface features, rather than surface area, are the key factors for the observed difference in the decomposition rates.

For decades, it is long thought that ZnO with high surface $V_{o\ surface}$ (acts a potential well) provides the active sites for photocatalysis [13-17]. The use of EPR data appears to support this fact. However, as stated, the EPR signal orginated from trapped unpaired electrons on surface cannot be totally attributed to $V_{o\ surface}$ sites. Also, Carter et al. showed that the $O_2^-(V_{o\ surface})$ species exhibit pronounced photochemical reactivity comparable to the superoxide species adsorbed at nonvacancy sites [34]. It is interesting to note that the order of surface hydroxyl groups shown by NMR exhibits the same

trend as the order of rate constants **(Figure 5-7b)** (cf. $V_{o\ surface}$, **Figure 5-7a** 3b). As a result, it is believed that the photocatalytic OH radical generation in water from ZnO NPs is directly linked with their surface-OH groups.

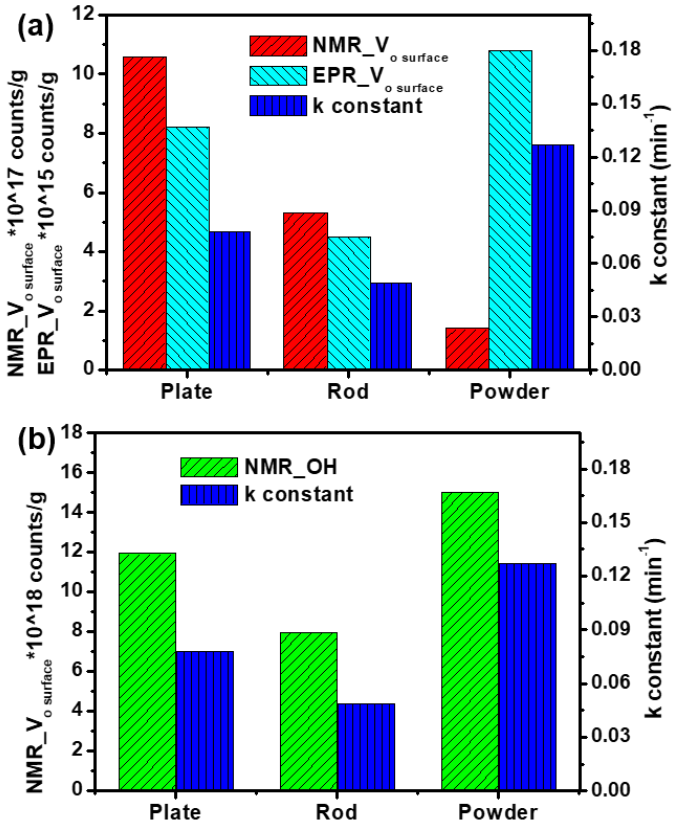

Figure 5-7. Comparison of a) $V_{o\ surface}$ derived from EPR/NMR and b) OH derived from NMR with k constant of ZnO plate, rod and powder.

Noted that the possibility of surface Zn_{3C} sites playing a key role is ruled out since the rod sample, possessing the highest concentration of Zn_{3C} (13.97 umol/g from both (100) and Zn-(002) facets), exhibits the lowest rate **(Table 5-2)**. This result also supports the conclusions of our previous study which found that the adsorption of dye molecules on Lewis acid sites (both V_o and Zn_{3C} herein) is not likely to be the rate determining step for reaction in the ZnO case [35]. As O atoms in the surface lattice do not seem to take part in this catalyzed reaction, the concentration of surface hydroxyl group could be the key factor that overrides the role of V_o in the photocatalysis. Similar result has also

been reported by Jang et al. and McLaren et al., who discovered that OH^- ions prefer to adsorb onto polar faces due to the positive surface charge. These ions can react with holes (h^+) to generate reactive species •OH radicals, hence enhancing the photocatalytic activity [11,12,27].

5.3.5. Photocatalytic mechanism over the Zn-OH surface

Generally, the recombination probability of the photo-generated carriers is high and therefore the lifetime of electron-hole pairs has been regarded as the most vital factor for the photocatalytic process [32]. Under light irradiation, electron transfer from the valance band (VB) to the conduction band (CB) occurs with the formation of electron-hole pairs on ZnO. In the case of ZnO with defects, these photo-generated holes can be trapped by surface defects and the separation of photo-generated electron-hole pairs is facilitated. Moreover, the photo-generated holes trapped by surface defects can also react with electron donors and thus promote the photocatalytic reaction. Since the existence of surface defects obviously play a positive role in the photocatalytic activity, tailoring the concentration of defects has received much attention during the last decade [11-17]. However, according to our result, the powder sample with the lowest V_o concentration exhibits the highest rate constant, indicating the role of V_o in the charge separation and the pre-adsorption of dye is not as significant as previous reported. Since the recombination of a photo-generated electron-hole pair in ZnO occurs on the nanoscale timescale, the rate of electron/hole trapping must be faster than their diffusion, so that the species acting as the carrier traps must be pre-associated with the chemical functionality of the photocatalyst surface [32]. Accordingly, it is the surface hydroxyl group instead of the adsorbed dye on V_o which is responsible for the generation of radicals.

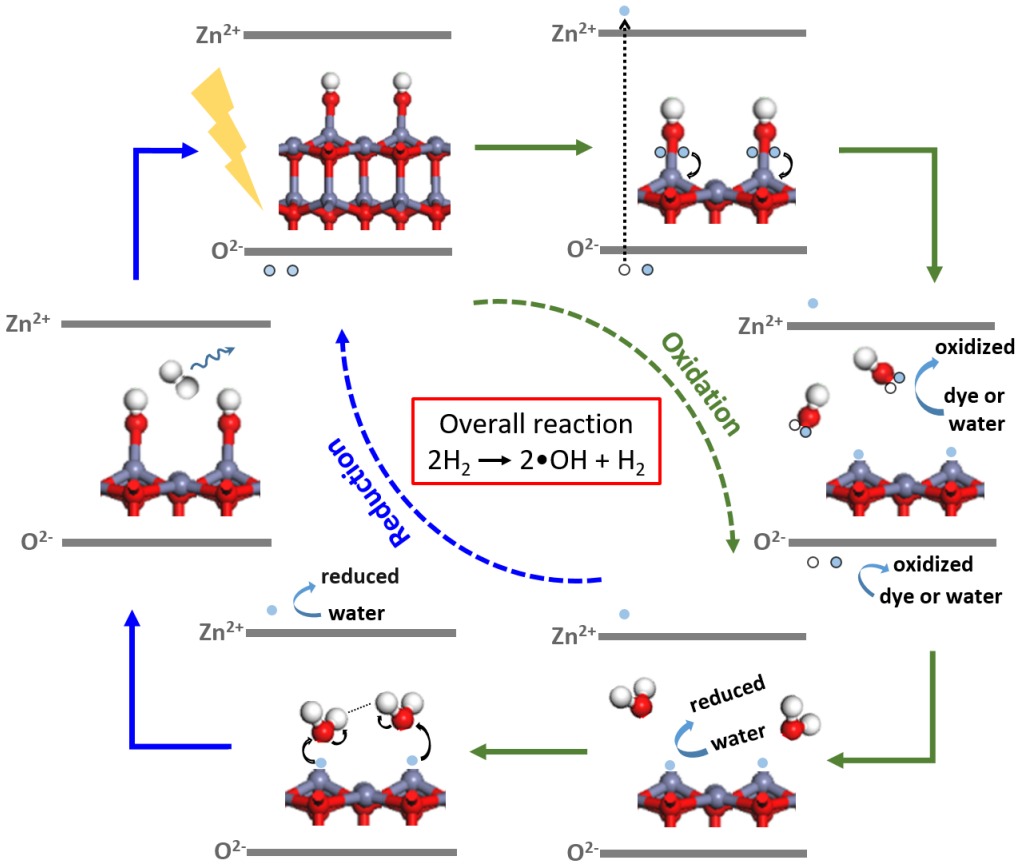

Figure 5-8. Schematic illustration of photocatalytic decomposition of methylene blue dye over ZnO nanoparticle by OH· in water generated from surface -OH.

Figure 5-8 summarizes our proposed model for the enhanced photocatalysis over the Zn-OH surface. Once an electron in the Zn-OH bond is excited by light of an appropriate wavelength, transfer of the electron to the Zn^{2+} site takes place. The high potential of the photogenerated hole in the VB of ZnO (3.0 eV) [31] is adequate to oxidize surface OH groups directly to hydroxyl radicals •OH (E^o -OH/•OH = 2.4 eV). This OH radical will then be liberated from the surface and react with water to generate more radicals which eventually oxidize the methylene blue molecule. As water is the solvent in this system, OH group can be readily regenerated when these photo-generated conduction band electrons on Zn reduce water molecule accompanied by the generation of H_2. The overall reaction is $2H_2O \rightarrow 2•OH + H_2$. Thus, the presence of

surface OH therefore facilitates the trapping and separation of photo-generated electrons and holes, enhancing the photocatalytic degradation process.

5.4. Chapter conclusion

Photoluminescence (PL) and electron paramagnetic resonance (EPR) are the two most commonly used techniques to evaluate surface oxygen vacancy ($V_{o\ surface}$) on photo-active transition metal oxides. However, it is demonstrated using ZnO NPs in this chapter that there are shortcomings of them in characterizing facet-dependent catalysis. PL technique fails to deliver precise $V_{o\ surface}$ with interferences from bulk defects as both defects give green luminescence at around 530 nm. EPR can distinguish defect location between bulk (g=1.9x) and outmost surface (g=2.00) as the unpaired electrons trapped in $V_{o\ surface}$ can be uptake by adsorbed dioxygen (O_2^-). However, it has been shown that the signal at g=2.00 does not necessary correlate to $V_{o\ surface}$ concentration due to equilibrium limitation and there are significant contributions from low coordination sites from polycrystalline particles. Despite the current wide use of the two techniques, they are shown to be incapable of providing precise $V_{o\ surface}$ concentration relevant to facet-dependent properties of ZnO NPs. Also, no information on other surface features (e.g. metal cation and hydroxyl proton) and their corresponding chemical states can be provided. Instead, with the assistance of chemical probe, ^{31}P MAS NMR has been shown in previous chapter can distinguish and quantify surface features of various facets.

We then compared the three above techniques (PL, EPR and NMR) in correlating the photocatalytic decomposition activity of methylene blue (MB) of ZnO NPs for the study of facet-specific photocatalysis. The concentration of surface hydroxyl group has been demonstrated the key factor that overrides the role of surface Vo, Zn_{3C} and O atoms in the MB photo-degradation. Based on this result, a new mechanism for photocatalytic •OH radical generation from direct surface-OH oxidation is revealed. Once an electron in the Zn-OH bond is excited by light of an appropriate wavelength,

transfer of the electron to the Zn^{2+} site takes place. The photogenerated hole in the VB of ZnO can efficiently oxidize surface OH groups directly to hydroxyl radicals •OH. This OH radical will then be liberated from the surface and react with water to generate more radicals which eventually oxidize the methylene blue molecule. As water is the solvent in this system, OH group can be readily regenerated when these photo-generated conduction band electrons on Zn reduce water molecule accompanied by the generation of H_2. The overall reaction is $2H_2O \rightarrow 2•OH + H_2$. Accordingly, this facet-specific technique not only makes cross-literature comparison feasible but also provides more comprehensive information to lead to further understanding of photocatalytic mechanism.

References:

[1] M. H. Huang, S. Rej, C.-Y. Chiu, *Small* **2015**, *11*, 2716–2726.

[2] S. Rej, H.-J. Wang, M.-X. Huang, S.-C. Hsu, C.-S. Tan, F.-C. Lin, J.-S. Huang, M. H. Huang, *Nanoscale* **2015**, *7*, 11135–11141.

[3] H. Dixit, W. Zhou, J.-C. Idrobo, J. Nanda, V. R. Cooper, *ACS Nano* **2014**, *8*, 12710–12716.

[4] C.-S. Tan, S.-C. Hsu, W.-H. Ke, L.-J. Chen, M. H. Huang, *Nano Lett.* **2015**, *15*, 2155–2160.

[5] B. Zhang, D. Wang, Y. Hou, S. Yang, X. H. Yang, J. H. Zhong, J. Liu, H. F. Wang, P. Hu, H. J.; Zhao, H. G. Yang, *Sci. Rep.* **2013**, *3*, 1836;

[6] C. Li, C. Koenigsmann, W. Ding, B. Rudshteyn, K. R. Yang, K. P. Regan, S. J. Konezny, V. S. Batista, G. W. Brudvig, C. A. Schmuttenmaer, J.-H. Kim, *J. Am. Chem. Soc.* **2015**, *137*, 1520–1529.

[7] W. Chrzanowski, A. Wieckowski, *Langmuir* **1998**, *14*, 1967–1970.

[8] B. M. Choudary, R. S. Mulukutla, K. J. Klabunde, *J. Am. Chem. Soc.* **2003**, *125*, 2020–2021.

[9] N. Tian, Z. Y. Zhou, S. G. Sun, Y. Ding, Z. L. Wang, *Science* **2007**, *316*, 732–735.

[10] R. Narayanan, M. A. El-Sayed, *J. Phys. Chem. B* **2005**, *109*, 12663–12676.

[11] E. S. Jang, J. H. Won, S.-J. Hwang, J. H. Choy, *Adv. Mater.* **2006**, *18*, 3309–3312.

[12] A. McLaren, T. Valdes-Solis, G. Li, S. C. Tsang, *J. Am. Chem. Soc.* **2009**, *131*, 12540–12541.

[13] G. R. Li, T. Hu, G. L. Pan, T. Y. Yan, X. P. Gao, H. Y. Zhu, *J. Phys. Chem. C* **2008**, *112*, 11859–11864.

[14] S. A. Ansari, M. M. Khan, S. Kalathil, A. Nisar, J. Lee, M. H. Cho, *Nanoscale*, **2013**, *5*, 9238–9246.

[15] Y. Lv, W. Yao, X. Ma, C. Pan, R. Zong, Y. Zhu, *Catal. Sci. Technol.* **2013**, *3*, 3136–3146.

[16] F. Kayaci, S. Vempati, I. Donmez, N. Biyikli, T. Uyar, *Nanoscale*, **2014**, *6*, 10224–10234.

[17] X. Zhang, J. Qin, Y. Xue, P. Yu, B. Zhang, L. Wang, R. Liu, *Sci. Rep.* **2014**, *4*,

4596.

[18] F. Liao, Y. Huang, J. Ge, W. Zheng, K. Tedsree, P. Collier, X. Hong, S. C. Tsang, *Angew. Chem. Int. Ed.* **2011**, *50*, 2162–2165.

[19] M. Behrens, F. Studt, I. Kasatkin, S. Kühl, M. Hävecker, F. Abild-Pedersen, S. Zander, F. Girgsdies, P. Kurr, B.-L. Kniep, M. Tovar, R. W. Fischer, J. K. Nørskov, R. Schlögl, *Science* **2012**, *336*, 893–897.

[20] Y. Qin, X. Wang, Z. L. Wang, *Nature* **2008**, *451*, 809–813.

[21] T. Andelman, Y. Gong, M. Polking, M. Yin, I. Kuskovsky, G. Neumark, S. O'Brien, *J. Phys. Chem. B* **2005,** *109,* 14314–14318;

[22] H. Zeng, G. Duan, Y. Li, S. Yang, X. Xu, W. Cai, *Adv. Funct. Mater.* **2010**, *20*, 561–572.

[23] L. Wang, Y. Kang, X. Liu, S. Zhang, W. Huang, S. Wang, *Sensor Actuat B-Chem.* **2012**, *162*, 237–243.

[24] B. Yu, C. Zhu, F. Gan, Y. Huang, *Mater. Lett.* **1998**, *33*, 247–250.

[25] L. Jing, Z. Xu, J. Shang, X. Sun, W. Cai, H. Guo, *Mater. Sci. Eng.* **2002**, *A332*, 356–361.

[26] S. Polarz, J. Strunk, V. Ischenko, M. W. E. van den Berg, O. Hinrichsen, M. Muhler, M. Driess, *Angew. Chem. Int. Ed.* **2006**, *45*, 2965–2969.

[27] Y. K. Peng, L. Ye, J. Qu, L. Zhang, Y. Fu, I. F. Teixeira, I. J. McPherson, H. He, S. C. E. Tsang, *J. Am. Chem. Soc.* **2016**, *138*, 2225–2234.

[28] J. K. Nørskov, T. Bligaard, J. Rossmeisl, C. H. Christensen, *Nature Chem.* **2009**, *1*, 37–46.

[29] F. Fabbri, M. Villani, A. Catellani, A. Calzolari, G. Cicero, D. Calestani, G. Calestani, A. Zappettini, B. Dierre, T. Sekiguchi, G. Salviati, *Sci. Rep.* **2014**, *4*, 5158.

[30] V. Ischenko, S. Polarz, D. Grote, V. Stavarache, K. Fink, M. Driess, *Adv. Funct. Mater.* **2005**, *15*, 1945–1954.

[31] U. Diebold, L. V. Koplitz, O. Dulub, *Appl. Surf. Sci.* **2004**, *237*, 336–342.

[32] M. Kunat, S. G. Girol, U. Burghaus, C. Wöll, C. *J. Phys. Chem. B* **2003**, *107*, 14350–14356.

[33] E. Carter, A. F. Carley, D. M. Murphy, *ChemPhysChem* **2007**, *8*, 113–123.

[34] E. Carter, A. F. Carley, D. M. Murphy, *J. Phys. Chem. C* **2007**, *111*, 10630–10638.

[35] Y. Zhao, C. Eley, J. Hu, J. S. Foord, L. Ye, H. He, S. C. E. Tsang, *Angew. Chem. Int. Ed.* **2012**, *51*, 3846−3849.

Chapter 6 TiO_2: Mapping of facets promoted with various surface groups by ^{31}P MAS NMR

6.1. Chapter overview

The uses of surface directing species (SDS) and surface additives to alter nanoparticle morphology and physico-chemical properties of particular exposed facets have recently been attracting a significant attention. However, the challenges in their chemical analysis sometimes at trace levels, understanding their roles to elucidate surface structure-activity relationships in optical (solar cells) or (photo)catalytic performance and their removals, are of great significance that remain to be solved. Here, we show a detailed analysis of TiO_2 facets promoted with surface species (OH, O, SO_4, F) w/o post-treatments by ^{31}P adsorbate-NMR supported with a range of other characterization tools. It is demonstrated for the first time that this study can obtain quantitative evaluations of the electronic and structural effects imposed by these surface additives and their removal mechanisms, which could lead to rational controls of active TiO_2 (001) and (101) facets for important applications.

6.2. Introduction

Surface features and distributions on metal oxide such as oxygen vacancy, cation, anion and hydroxyl groups have been shown to play a decisive role in various important applications such as optics, electronic devices and heterogeneous catalysis, etc [1-5]. In particular, for particle in nano size, the domination of these surface features has been demonstrated exhibiting different physical/chemical properties compared to their bulk. Given that each facet possesses distinctive intrinsic energy, it is understandable that

both concentration and chemical state of surface features differ from facet to facet. Take ZnO nanocrystallite as an example, the interested "surface oxygen vacancy (V_o)" has been shown mostly populated on oxygen-terminated (002) facet [6], which has recently been quantified by Peng *et al* [7]. Also, the chemical properties of surface zinc ion has been shown to be different on (100) and (002) facets, indicating the Lewis acidity of ZnO NP can be modulated by the morphology control [7].

These considerations have added exciting variables in tailoring morphology of nanoparticles (NPs) with preferentially exposed facets during the past decades. Unfortunately, facets with high reactivity are unstable and tend to diminish rapidly to minimize surface energy during the crystal growth [8]. Accordingly, a structural directing specie (SDS) or surfactant is usually employed in the shape control of NPs, which renders them in metastable and high-energy forms. Those adsorbates which range from simple inorganic species to complex organic molecules can subtly modify the chemical state of surface features (especially metal cations) and provide a kinetic growth control for the formation of metastable shaped NPs [1]. As the growth rate of a crystal facet depends on the surface energy (high-energy facets grow more quickly than low energy facets), different morphologies of NP could thus be prepared by using various structural directing molecules [8,9].

We have been interested in structure-activity relationships of titanium oxide nanoparticle, an important solid system with profound technical importance. Particularly, tailoring anatase form of TiO_2 crystals with termination of specific facets have been the hottest research topic since the past decades. However, most synthetic TiO_2 crystals are covered with thermodynamically more stable (101) facets rather than the reactive (001) facets [10,11]. The breakthrough in control synthesizing crystals with

high percentage of reactive high-energy (001) was not made until 2008 [12]. According to that literature, the relative stability of these two facets can be reversed by the use of small quantity of fluorine on (001) surface during the particle synthesis. Since then the control synthesis of TiO_2 nano-crystal with preferentially exposed (001) facet has been shown to display promising properties in photocatalysis [13-24], methanol conversion [25], solar cell [26-29] and lithium battery [30,31], etc.

Generally, the removal of SDS such as fluorine in this case after the shape control of nanoparticle would be required to avoid its interfering to the interested properties on this surface. It can be removed by an introduction of a simple post-treatment step such as calcination at 600°C [12,14-16,19,21,23,26,27,30] or ion exchange with aqueous NaOH [13,15,17-19,24] before the application in order to obtain a so-called "clean surface". However, by adopting different removal methods, diverse results have been obtained in literature in various applications, which create different interpretations and frequently disagreements amongst researchers (also refer to **Table 1-1**) [13-31]. For example, the NaOH treated (001) facet (i.e. Na-(001)) showed higher activity in the photocatalytic degradation of methyl orange (MO) dye than the F-capped (001) facet (i.e. F-(001)) [13], while a reversed result was obtained for the same reaction by the other research group [15]. Also, both NaOH and calcination treatment were reported to increase the facet activity of (101) in photocatalytic hydrogen evolution [16,17], while the NaOH treatment was concluded to lower the facet activity of (001) in this reaction by others [17,18].

Those different observations and interpretations made amongst researchers can be arisen from surface reconstruction of unstable (001) upon its removal during calcination [32,33] or trace of residue SDS remained on surface affecting the chemical state of

exposed titanium (vide infra). So far, no clear rationalization and no guidance for the selection of appropriate post-treatment methods are yet achieved. In addition, the SDS modification on TiO_2 surface has been demonstrated to efficiently modulate the surface Ti chemical state. For example, the post modification of PO_4^{3-}/SO_4^{2-} on the TiO_2 surface has been shown not only to provide extra Brönsted acid (BA) sites but also increase Lewis acidity for enhanced sugar conversion [34,35] and photocatalysis [36,37]. The chelating properties of surface COOH-containing dye molecule plays an important role in modifying TiO_2 conduction band (unfilled d-band of Ti^{4+}) for efficient electron transfer in dye-sensitized solar cell (DSSC) [38]. Also, adding a small quantity of nitrogen-containing heterocycle additive such as 4-*t*-butylpyridine (TBP) to the electrolytic solution has been found to remarkably improve the solar cell performance due to the shift of Ti d-band edge toward negative potentials by adsorption onto the TiO_2 surface, etc [39]. We believe the confusions were arisen mainly from the lack of surface characterization tools for crystal facets which can provide accurate information to correlate to physico-chemical properties.

Given the importance of the facet-dependent properties of TiO_2 nanoparticle and their chemical modifications for a wide range of applications, there is still no detailed work on the mapping of surface features of functionalized TiO_2 with different morphologies. Herein, using anatase TiO_2 samples of different morphologies, we have successfully monitored the subtle changes of Ti chemical state induced by a small quantity of surface adsorbates (i.e. fluorine, sulfate, OH) on various facets using ^{31}P magic angle spinning (MAS) NMR in combined with trimethylphosphine (TMP) as surface probe. This is since the nucleophilic probe TMP molecule can form a stable adduct with the exposed Ti cation (Lewis acid, LA) of TiO_2 surface, the formation of a surface TMP-Ti complex can be realized via coordination of the P atom to the surface Ti cation center. According

to ^{31}P chemical shift ($\delta^{31}P$) of the corresponding surface TMP-Ti complexes, it is demonstrated the surface Ti cations on various facets with different Lewis acidities, surface energies and steric arrangements can be carefully mapped, differentiated and quantitatively analyzed. It is shown that some typical post-treatments (i.e. calcination or NaOH wash) to remove the fluorine (as SDS) can also lead to different surface Ti chemical states. According to our catalytic testing, extra caution must be exercised for even trivial surface treatments as a huge difference in activity can be obtained. This technique (i.e., using TMP as a surface probe) is thus demonstrated as a powerful tool in combination with conventional surface techniques adopted for TiO_2 NPs such as X-ray photoelectron spectroscopy (XPS) and electron paramagnetic resonance (EPR) to offer comprehensive information of surface features on various functionalized facets to guide surface treatments/modifications of TiO_2 nanoparticle for applications.

6.3. Results and discussion

6.3.1. As-prepared TiO_2 nanocrystals and their surface chemical states

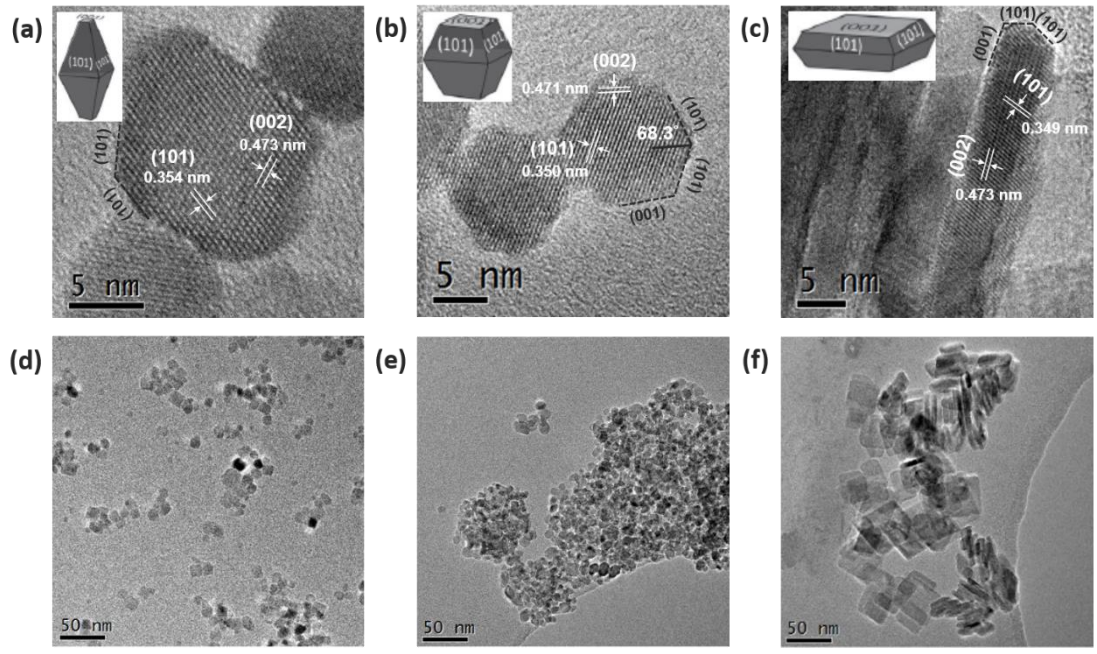

Figure 6-1. High resolution TEM images of as-prepared (a) Powder (PD), (b) F-(101), (c) F-(001). (d), (e) and (f) are their corresponding low magnification TEM images.

The high resolution TEM (HRTEM) and TEM images of as-prepared samples **(Figure 6)** show the emerging of particle shape as a function of HF concentration. Samples prepared with 0 mL, 2 mL and 6 mL of 50 wt% concentration of HF reveal different morphologies and are christened as powder (PD) **(Figure 6-1a)**, F-(101) **(Figure 6-1b)** and F-(001) **(Figure 6-1c)**. All three samples exhibited clear lattice fringes with d-spacings around 0.47 and 0.35 nm, in accordance with [002] and [101] crystallographic planar directions of anatase TiO_2, respectively. According to Wulff construction, the proportion of exposed (101) and (001) facets in as-prepared samples can be calculated from particle face length and thickness. The powder sample (synthesized without HF) was characterized with ~90% (101) facet **(Table 6-1)**, matching well with the predominant thermodynamic stable of (101) facet in anatase TiO_2 predicted by Wulff construction (~ 94%) [40]. These particles gave an average face length of 3.8 ± 0.5 nm. According to literature, when HF concentration used is increased, it can increase the particle face length due to preferential adsorption of F to slow down its growth on this facet and hence the percentage of exposed (001) facet increases. Indeed, when 2 mL HF was used (i.e. F-(101)), an average face length of ca. 6.6 ± 1.0 nm was achieved with a substantial higher proportion of (001) facet **(Table 6-1)**. By using 6 mL HF, the elongated face length of ca. 41.0 ± 10.5 nm with a thickness of ca. 6.2 ± 0.9 nm nanosheet-like F-(001) particles were obtained **(Table 6-1)**. The percentages of exposed (101) and (001) facets of F-(001) were estimated to be 24.6% and 75.4%, respectively **(Table 6-1)**.

Sample	Solvent	% (101)	% (001)
0HF	0.6 mL H_2O	89.8	10.2
2HF	0.2 mL HF/0.4 mL H_2O	78.9	21.1
6HF	0.6 mL HF	24.6	75.4

Table 6-1. Sample preparation conditions and the calculated percentage of exposed (101) and (001) facets.

Figure 6-2 show the corresponding ^{31}P MAS NMR spectra of TMP-adsorbed powder, F-(101), F-(001) samples. It is clear that this technique gives distinctive fingerprint-like NMR patterns for TiO_2 samples with various surface exposures/treatments. In general, the chemical shift of ^{31}P ($\delta^{31}P$) in a range of -2 to -5 ppm has been well attributed to the formation of $TMPH^+$ ionic complex formed when a TMP molecule is protonated (BA site), while the $\delta^{31}P$ of adsorbed TMP spans over a wide range (-20~-58 ppm) when interacting with surface acidic site (LA site) with various Lewis acidity (the formation of TMP-LA) [41]. Thus, a stronger interaction of the surface acidic site with the basic TMP molecule is expected to give a more positive $\delta^{31}P$ shift in the NMR spectrum, the magnitude of this shift should depend on the adsorption energy/geometry on a particular facet and the TMP molecule [7].

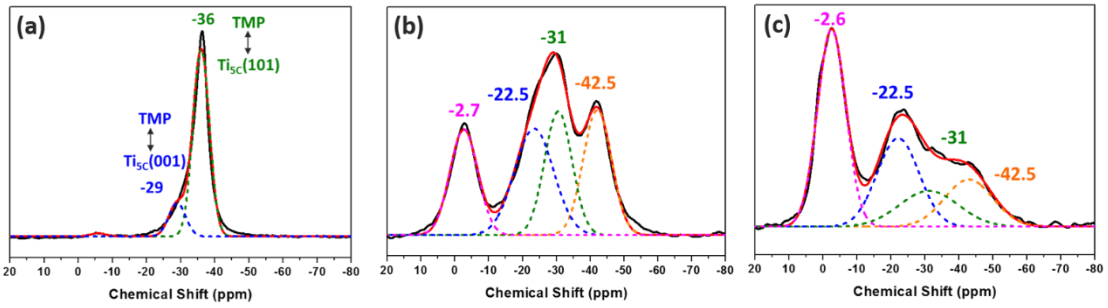

Figure 6-2. ^{31}P MAS NMR spectra of TMP-adsorbed TiO_2 (a) Powder (PD), (b) F-(101) and (c) F-(001). Green represents ^{31}P chemical shift of TMP of surface 5-coordinate Ti^{4+} on (101) facet (i.e. $Ti_{5C}(101)$), blue represents ^{31}P chemical shift of TMP of 5-coordinate Ti^{4+} on (001) facet (i.e. $Ti_{5C}(001)$), orange represents the ^{31}P chemical shift of TMP of surface Ti^{4+} containing OH and F and pink represents ^{31}P chemical shift of TMP on Brönsted acid site (TiO(H)-Ti).

In order to compare these NMR peaks over the samples with different proportions of facets, ^{31}P MAS NMR peaks in the spectra of TMP-adsorbed have been carefully deconvoluted. Powder sample shown in **Figure 6-2a** reveals no significant formation of $TMPH^+$ complex between -2 to -5 ppm but TMP-LA complex with a main peak at -36 ± 1 ppm and a small shoulder at lower chemical shift (-29 ± 1 ppm) are clearly

evident. The error of ± 1 ppm includes variations in facet dimension, defect concentration and measurement inaccuracy, etc in heterogeneous solid system. Notice that similar results in chemical shift values have been shown by Deng and co-workers over their titanium oxide [37]. The major peak at -36 ppm and the shoulder at -29 ppm with the integrated area ratio of 84.8% and 15.2% can be attributed to the interaction between TMP and surface five-coordinate Lewis acids: Ti^{4+} on (101) facet as Ti_{5C}(101) and Ti^{4+} on (001) as Ti_{5C}(001), respectively. This high proportion value of (101) facet in our powder sample matches with our earlier estimation using Wulff construction (89.8%, **Table 6-1**).

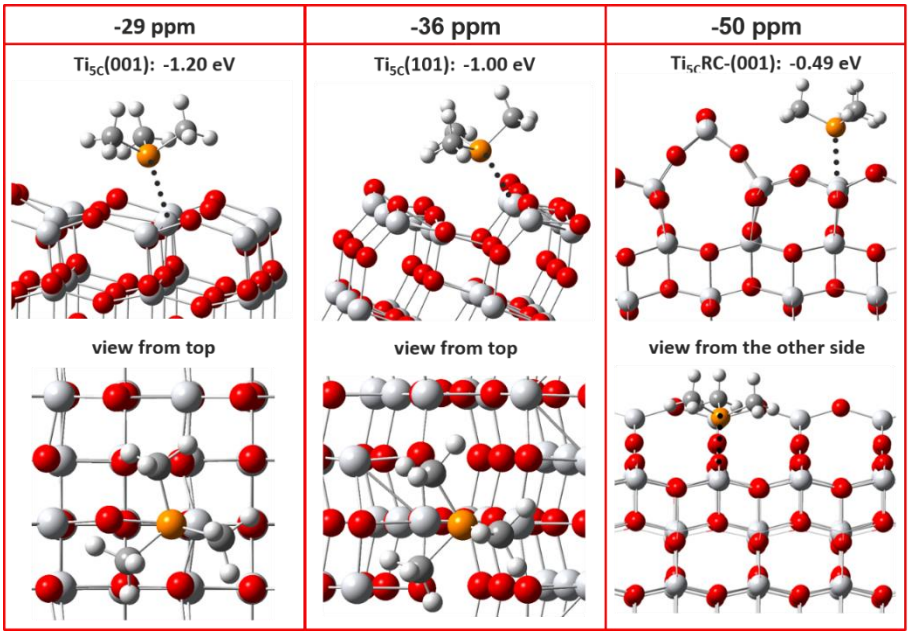

Figure 6-3. Schematic illustrations of molecular interaction and DFT calculated adsorption energy (E_{ad}) between TMP and various TiO_2 facets. Ti_{5C}(001), Ti_{5C}(101) and Ti_{5C}RC-(001). RC-(001) represents reconstructed (1 x 4) (001) facet (carried out by Prof. Hung-Lung Chou).

It has been observed that the adsorption energy of TMP molecule on Lewis acid site shows a strong correlation with its NMR chemical shift value [7,41-43]. As shown in **Figure 6-3**, our calculated adsorption energies of TMP on Ti_{5C}(001), Ti_{5C}(101) and Ti_{5C}

RC(reconstructed)(001) are obtained according to computational models, respectively (calculated by Prof. Hung-Lung Chou, National Taiwan University of Science and Technology). Indeed, it is found that the calculated adsorption energy displays an excellent linear relationship with the experimental chemical shift value obtained **(Figure 6-4)**. Thus, this NMR technique is capable of differentiating facets of decreasing energy: (001) > (101) > RC(001) by their chemical shift values (-29, -36, -50 ppm), respectively. The relatively higher BA signal around -3 ppm of F-(001) sample shown in **Figure 6-2c** as compared to that of F-(101) sample shown in **Figure 6-2b** again clearly indicates the preferential expose of the (001) facet due to the increase in F concentration used.

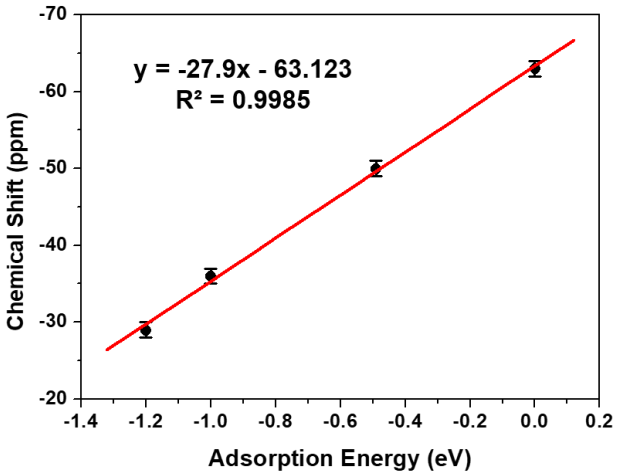

Structure	$E_{adsorption}$ (eV)_cal.	$\delta^{31}P$ (ppm)_expt.
TMP molecule	0	-63 ± 1
Ti_{5C}RC-(001)	-0.49	-50 ± 1
Ti_{5C}(101)	-1	-36 ± 1
Ti_{5C}(001)	-1.2	-29 ± 1

Figure 6-4. A linear regression plot by using experimental $\delta^{31}P$ and calculated adsorption energy.

On the other hand, some immediate questions remain to be answered from **Figure 6-2**. First, why did the resolved (101) peak of chemical shift -31 ± 1 ppm and (001) peak of -22.5 ± 1 ppm from the samples prepared with HF (i.e. F-(101) and F-(001)) show a

consistent and significant 5 to 7 ppm downshift from corresponding facets of -36 and -29 ppm in powder sample (no fluorine contamination), respectively? What is the nature of the peak with chemical value of -42.5 ± 1 ppm, which was not seen over the PD sample? Why did the samples with HF treatment (i.e. F-(101) and F-(001)) show both BA and LA signals but the as-prepared powder sample (PD) possessed mainly LA signal?

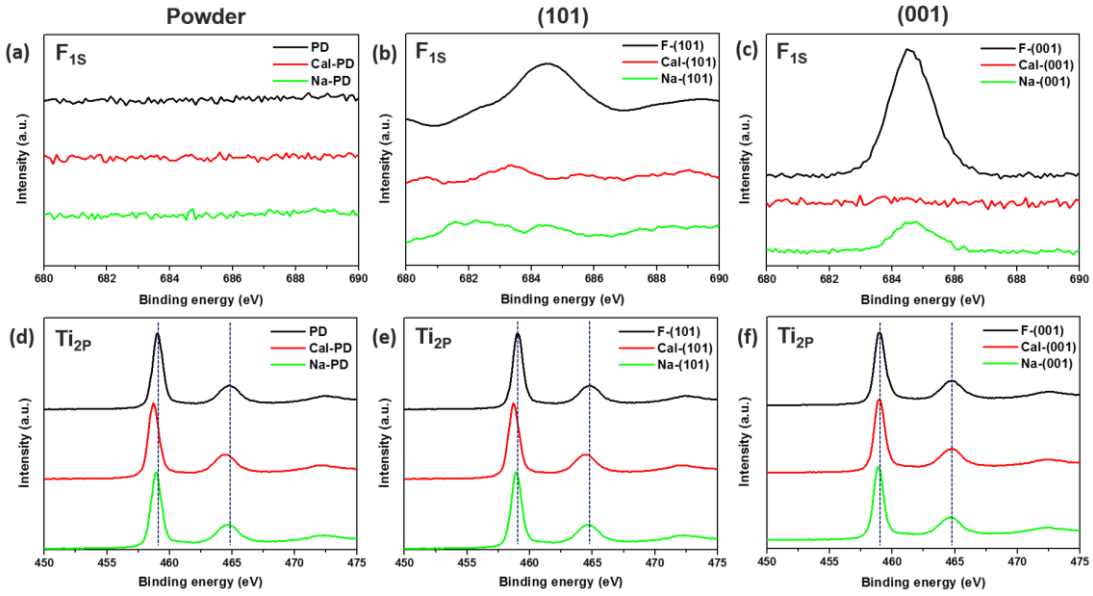

Figure 6-5. XPS F_{1S} spectra of as-prepared (a) PD, (b) F-(101) and (c) F-(001) TiO_2 samples with different treatments (calcination and NaOH wash). (d) to (f) are the corresponding XPS Ti_{2P} spectra.

As X-ray photoelectron spectroscopy (XPS) is a general accepted technique to monitor element(s) on material surface, we then carried out to analyse the surface compositions of these samples. As shown in the first row of **Figure 6-5**, the surface F on powder, F-(101) and F-(001) samples can be monitored by XPS as previously reported [12]. It is noted that F is apparently retained on the facets (101) and (001) when the samples were prepared with F **(Figure 6-5b and Figure 6-5c)** but the powder sample without previous exposure to F shows the total absence of F_{1S} signal **(Figure 6-5a)**. Despite the fact that XPS has been regarded as a surface sensitive technique to atomic chemical state, it fails to give any chemical shift of Ti_{2P} in the presence of fluorine **(second row**

of Figure 6-5). It is clear that the long electron escaping depth with more than outmost atomic layer (few atoms depth) from sample by XPS render it not a truly surface technique (detection limit ~ 0.1% atom) and the monitor of core-electrons makes the binding energy of Ti also less sensitive to electronic effect from neighbour F element(s). Auger electron spectroscopy (AES) is known to provide higher spatial resolution and the energy of ejected Auger electrons is sensitive to chemical environment compared to the core-level signals in XPS. However, as shown in **Figure 6-6**, no peak shift was also observed for five Ti LMM Auger signals (marked by dashed blue line). This indicates the change of chemical state of the outmost Ti atom is still averaged out during the collection of Auger electrons from the electron escaping depth. In contrast, the ^{31}P NMR is much surface sensitive to the electronic change imposed by this SDS.

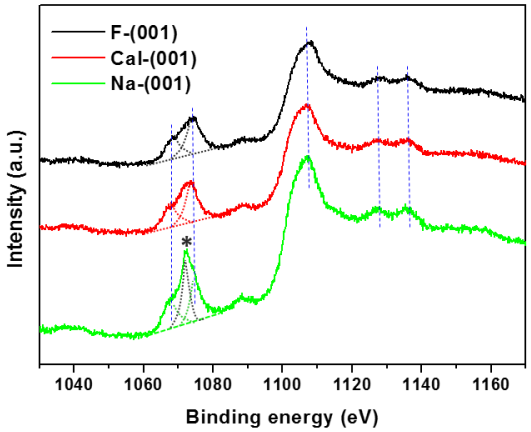

Figure 6-6. XPS Ti LMM Auger spectra of as-prepared F-(001) TiO_2 samples (marked by dashed blue line) with different treatments (Cal: calcination and Na: NaOH wash). The peak marked with asterisk "*" is Na_{1S} signal.

The 5 to 7 ppm downshift values of F-(101) and F-(001) samples from corresponding facets of -36 ppm Ti_{5C}(101) and -29 ppm Ti_{5C}(001) in powder sample to -31 ± 1 ppm and -22.5 ± 1 ppm, respectively are likely due to the presence of the electronic withdrawing effect of fluorine exerted to the Ti^{4+} on these two facets. The corresponding atomic ratios (Ti, O and F) of TiO_2 samples by XPS are summarized in

Table 6-2. The apparent lower Ti: O values in the presence of F clearly suggest the formation of oxygen vacancies (V_o) due to strong electronic withdrawing effect of the surface fluorine groups.

Powder	Ti : O : F ratio	(101)	Ti : O : F ratio	(001)	Ti : O : F ratio
PD	1 : 1.987 : 0.000	F-(101)	1 : 1.915 : 0.180	F-(001)	1 : 1.820 : 0.400
Cal-PD	1 : 1.961 : 0.000	Cal-(101)	1 : 1.980 : 0.000	Cal-(001)	1 : 1.976 : 0.000
Na-PD	1 : 2.050 : 0.000	Na-(101)	1 : 1.955 : 0.000	Na-(001)	1 : 1.976 : 0.124

Table 6-2. Atomic ratios of PD, F-(101) and F-(001) TiO_2 samples evaluated by XPS with different post-treatments (calcination and NaOH wash).

EPR g value at around 2.0 **(Table 6-3)** could also be used to investigate the formation of surface oxygen vacancy imposed by this surface impurity. Thus, such unstable (001) facet with highest F containing surface oxygen vacancies could be hydrolysed (introduction of the OH functional group) during the treatment to account for the -42.5 ± 1 ppm peak observed (see later experiments). In addition, the evolution of Brönsted acidity over the fluorine contaminated facets can be rationalized by the surface hydrogen bonding stabilization of protons by the fluorine. As a result, one has to be very careful about the detainment of surface additive on a particular facet which can subtly affect its electronic, structural and geometric properties (acidity) hence the evaluation of facet-dependent properties. Thus, post-treatment to remove SDS before the study of facet dependent properties is crucially important.

Powder	g~2.0 (counts/g)	(101)	g~2.0 (counts/g)	(001)	g~2.0 (counts/g)	g~1.95 (counts/g)
PD	7.811×10^{14}	F-(101)	1.276×10^{15}	F-(001)	2.576×10^{15}	3.442×10^{15}
Cal-PD	-	Cal-(101)	1.181×10^{15}	Cal-(001)	1.368×10^{15}	-
Na-PD	-	Na-(101)	9.408×10^{14}	Na-(001)	9.020×10^{14}	-

Table 6-3. EPR quantitative information of g value at 2.0 and 1.95 of F-(001), F-(101) and PD TiO_2 samples with different treatment (calcination and NaOH wash).

6.3.2. Post NaOH and calcination treatments

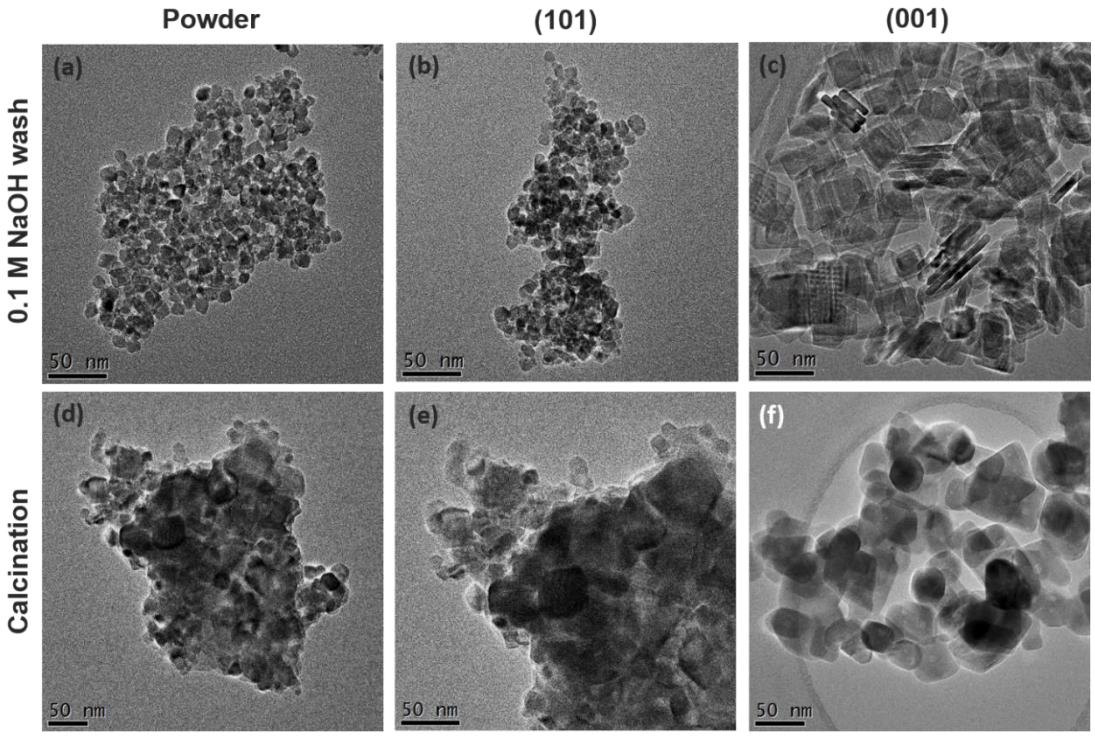

Figure 6-7. Morphology of TiO_2 samples after different treatments. TEM images of TiO_2 samples after (a-c) NaOH wash: (a) Na-PD, (b) Na-(101), (c) Na-(001) and after (d-f) calcination treatment: (d) Cal-PD, (e) Cal-(101), (f) Cal-(001).

As stated, NaOH wash [13,15,17-19,24] and calcination treatment [12,14-16,19,21,23,26,27,30] of F-treated samples at elevated temperature are the two commonly used methods in literature to remove surface F after the controls of TiO_2 particle morphology. The apparent remaining F signal on Na-(001) sample (cf. Cal-(001)) after NaOH (0.1M) treatment shown in **Figure 6-5c** clearly indicates that the F removal was not complete presumably due to the higher F affinity for this energetic surface. In contrast, there is no F found in all calcined samples by the XPS **(the first row of Figure 6-5)**. However, this does not necessary suggest that calcination is a good method since high energetic facet may easily reconstruct to more stable surface at high temperature [32,33]. Moreover, as evidenced by TEM images **(Figure 6-7)**, calcination treatment causes severe particle aggregation for all three as-prepared PD, F-(101) and

F-(001) while NaOH treatment doesn't lead to any observable aggregation and change in morphology. This result can be further supported by their corresponding XRD patterns **(Figure 6-8)**. These two post-treatments according to our surface analysis could generate artefacts when facet dependent properties are studied.

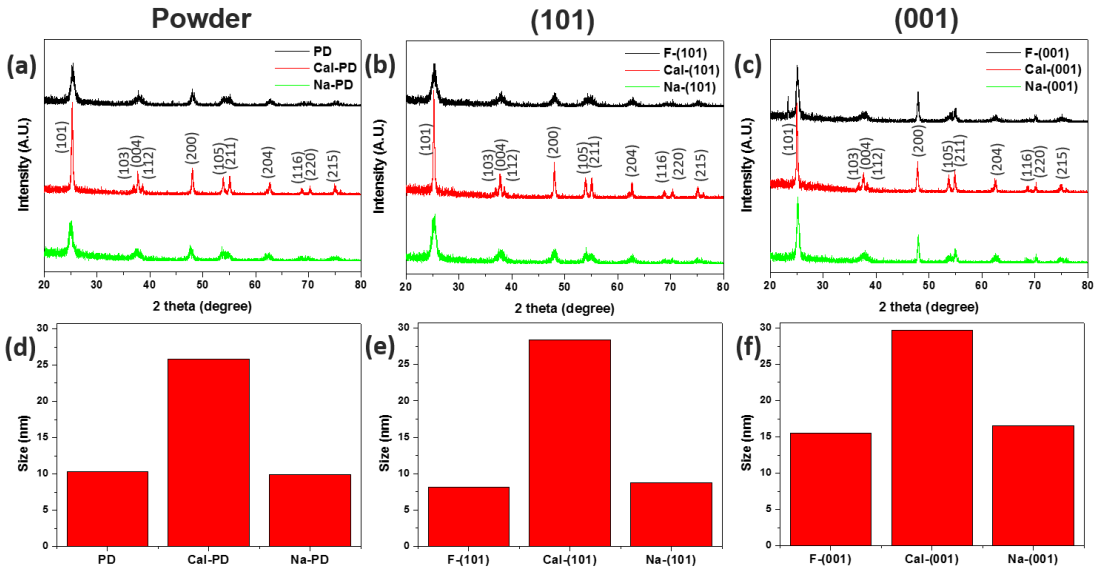

Figure 6-8. XRD spectra of as-prepared (a) PD, (b) F-(101) and (c) F-(001) TiO_2 samples with different post-treatments (calcination and NaOH wash). (d), (e) and (f) are corresponding particle size calculated from the full width at half-maximum of the (101) peak using Scherrer equation.

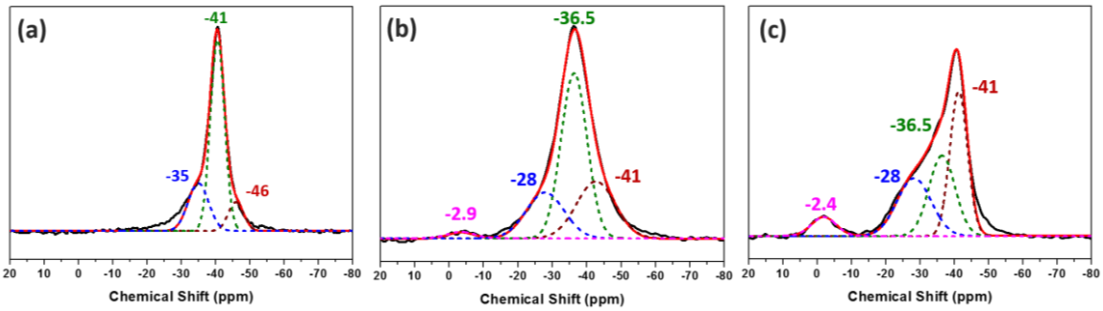

Figure 6-9. ^{31}P MAS NMR spectral deconvolution of TMP-adsorbed TiO_2 samples treated with 0.1 M NaOH (a) Na-PD, (b) Na-(101) and (c) Na-(001).

NaOH wash to remove surface F. As 0.1 M NaOH has been widely adopted in literature to remove surface fluorine [13,15,17-19,24], ^{31}P MAS NMR spectra of TMP-adsorbed Na-PD, Na-(101) and Na-(001) were also collected and are deconvoluted in

Figure 6-9. In order to reduce the influence of NaOH on the measured chemical shift values, the samples after the NaOH treatment were repeatedly washed with DI water. For sample prepared without HF (i.e. PD) **(Figure 6-9a)**, the NaOH treatment, after rinsed with DI water clearly reduces the Lewis acidity of both Ti_{5C}(001) and Ti_{5C}(101) as δ^{31}P shifts from -29 ppm to -35 ± 1 ppm for Ti_{5C}(001) and from -36 ppm to -41 ± 1 ppm for Ti_{5C}(101), respectively for the surface mono-hydroxylation (cf. as-prepared PD, **Figure 6-2a**). A shoulder appears at higher field (~46 ± 1 ppm) which is attributed to the formation of multi-hydroxylation $Ti_{5c}O_{5-x}(OH)_x$ with x > 2 during the extensive hydrolysis by the NaOH treatment at high concentration **(Figure 6-10)** [44,45].

While for F-treated samples (i.e. F-(101) or F-(001)), different LA distributions are obtained after the same NaOH treatment **(Figure 6-9b and Figure 6-9c)**. The conversion of residue F-Ti to HO-Ti on high energetic facets, particularly on (001), by the OH- exchange in NaOH wash can give a very different electron density of Ti_{5C} atoms compared to those surface Ti without the F. This surface chemical functionalization of OH shifts the δ^{31}P of TMP-adsorbed F-Ti_{5C}(001)/F-Ti_{5C}(101) from -22.5 ± 1 ppm /-31 ± 1 ppm **(Figure 6-2b and Figure 6-2c)** to -28 ± 1 ppm /-36.5 ± 1 ppm **(Figure 6-9b and Figure 6-9c)**. In addition, the typical BA signals (the formation of $TMPH^+$) between -2 ~ -5 ppm clearly indicate that there is a residue F left on both Na-(101) and Na-(001) sample surfaces **(Figure 6-9b and Figure 6-9c)**. On the other hand, the total F-depleted surfaces of -35 ± 1 ppm for Ti_{5C}(001) and -41 ± 1 ppm for Ti_{5C}(101) are expected to re-emerge since NaOH is capable of removing some surface F. The former peak (-35 ppm) is unfortunately mixed with the OH shifted F-Ti_{5C}(001) peak (-36.5 ppm) but the prominent at -41 ± 1 ppm can be attributed to the reformation of Ti_{5C}(101) **(Figure 6-10)** during its surface hydrolysis by the NaOH treatment.

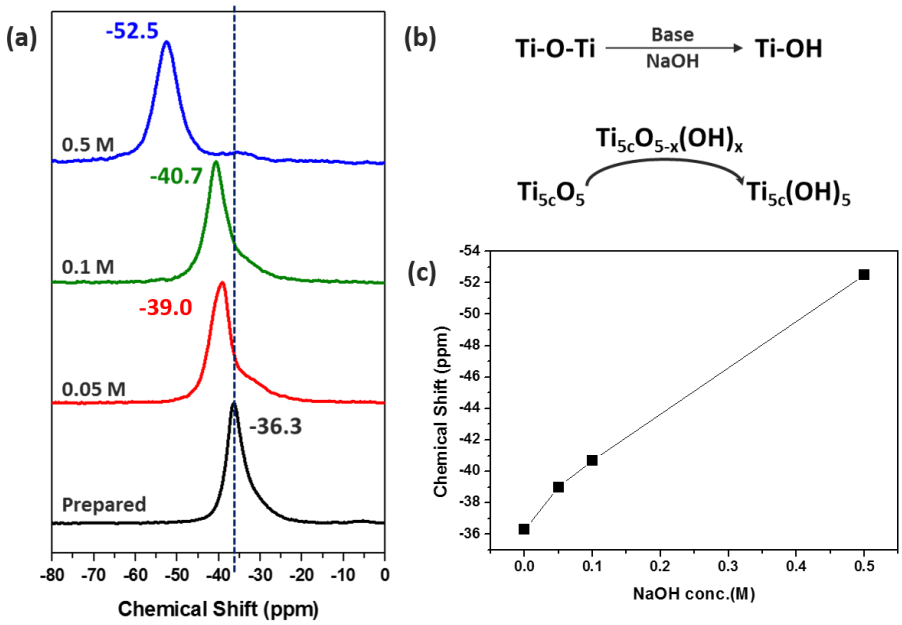

Figure 6-10. (a) ^{31}P MAS NMR spectra of TMP-adsorbed powder (PD) samples treated with various NaOH concentrations; (b) schematic illustration of the hydrolysis of surface Ti-O-Ti (c) corresponding linear regression plot by using ^{31}P chemical shift and NaOH concentration.

Post-calcination to remove surface F. Recently, the heat-induced aggregation of sheet-like anatase TiO_2 has been shown preferentially along particle [001] crystallographic direction, driven by the minimization of surface energy [46,47]. According to Yang et al. [46], surface Ti-F groups are totally hydrolyzed during calcination in moisturised air at high temperature (endothermic reaction) **(Figure 6-11)**.

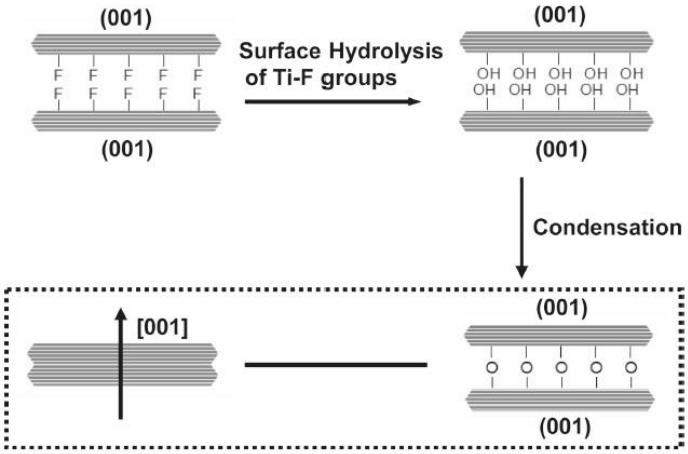

Figure 6-11. The growth mechanism of stacked anatase TiO_2 nanosheets dominated by (001) facets at their interfacial regions proposed by Yang et al. [46].

In this case, the exposed surfaces of sheet-like anatase TiO_2 are also mainly covered by -OH groups. As (001) facet has a higher surface energy than (101) facet, the (001) interfaces between adjacent nanosheets would be eliminated through the condensation of Ti-OH groups (formation of Ti-O-Ti linkages) at high temperature and therefore the (101) facet becomes dominant **(Figure 6-11)**. According to our XPS **(Figure 6-5)**, TEM **(Figure 6-7)** and XRD **(Figure 6-8)** data, the post calcination although is effective to remove F from (001) and (101) surfaces, which can clearly induce aggregation.

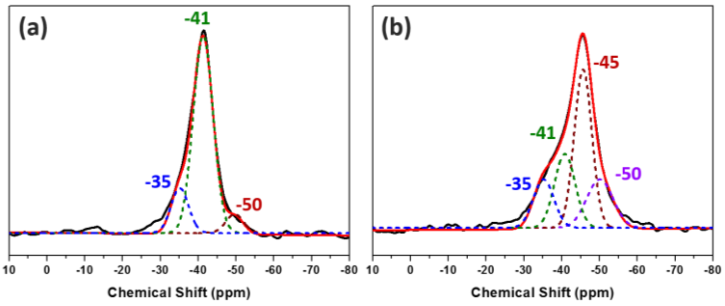

Figure 6-12. ^{31}P MAS NMR spectral deconvolution of TMP-adsorbed TiO_2 samples treated with calcination (a) Cal-PD, (b) Cal-(001)

^{31}P MAS NMR spectra of TMP-adsorbed Cal-PD and Cal-(001) were deconvoluted and are shown in **Figure 6-12a** and **Figure 6-12b**. It is noted that calcination in moisturised air pushes the $\delta^{31}P$ of $Ti_{5C}(001)/Ti_{5C}(101)$ of PD from -29/-36 ppm to -35 ± 1 ppm /-41 ± 1 ppm due to the surface mono-hydroxylation as mentioned previously (cf. as-prepared PD, **Figure 6-2a**). Interestingly, **Figure 6-12a** shows a new but characteristic signal of Cal-PD at -50 ± 1 nm. According to our DFT calculation (i.e. -50 ppm, **Figure 6-3**), this is due to the adsorption of TMP on Ti_{5C} on (1 x 4) reconstructed (001) facet (Ti_{5C}RC-(001)). Thus, this peak can be used as a diagnostic peak to indicate reconstruction/aggregation induced by calcination. While for F-(001), the same chemical shifts for $Ti_{5C}(001)/Ti_{5C}(101)$ (i.e. -35 ± 1 ppm /-41 ± 1 ppm) indicative of the mono-hydroxylation of the surfaces with no residue F can be obtained by the calcination

(Figure 6-12b) but not for the NaOH wash at room temperature, where detainment of F on Ti_{5C}(001)/F-Ti_{5C}(101) is evident (-28 ± 1 ppm /-36.5 ± 1 ppm, see **Figure 6-9c**). The large signal of Cal-(001) at -45 ± 1 ppm **(Figure 6-12b)** can be assigned to the meta-stable (1 x 3) and (1 x 5) (001) facets originated from the dominant high energy but unstable (1 x 1) (001) facet before their further transformation to the more stable reconstructed (1 x 4) structure (at -50 ppm) [33]. By comparing the area of deconvoluted peaks of Cal-(001), we are able, for the first time, to show an approximate 80% of (001) facet that had been reconstructed during the calcination.

6.3.3. Surface sulfation

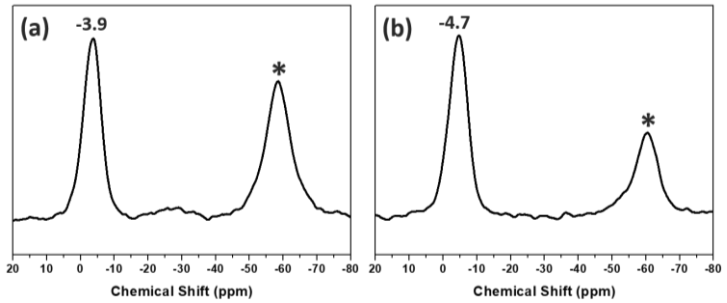

Figure 6-13. ^{31}P MAS NMR spectra of TMP-adsorbed calcined TiO_2 samples after following sulfation treatment (a) S-Cal-PD, (b) S-Cal-(001). *: physisorbed TMP (~-61 ppm).

As stated, surface functionalization could severely alter facet properties but this issue has not been much addressed in previous literature. The sulfation of TiO_2 facets over samples was therefore investigated after the calcination or NaOH wash with a prolonged period of time to ensure no F remained on the surfaces. The ^{31}P MAS NMR result for calcined samples after sulfation treatment (i.e. S-Cal-PD and S-Cal-(001)) were shown separately in **Figure 6-13a** and **Figure 6-13b**. As calcination treatment causes severe aggregation and unavoidable facet reconstruction, we herein focus on the sulfation of NaOH washed samples. For F-(101) and F-(001) samples, BA (Ti-O(H)-Ti) sites removed by NaOH wash can clearly be re-introduced by a sulfation step with the

large and distinctive peak around -4 ppm **(Figure 6-14b and Figure 6-14c)**. It is interesting to note that two new and characteristic strong LA peaks due to TMP adsorption on sulphated surfaces namely -25.5 ± 1 ppm and -34 ± 1 ppm are introduced. It is postulated these two new LA sites are arisen from the Ti^{4+} modified directly by SO_4 at high surface coverage during the extensive sulfation but further verifications are required. Their strengths (peak shifts) are sensitive to the particularly facets and their relative concentrations (peak areas) also depend on the relative proportions of (101) and (001) in the samples. For instance, S-Na-(101) with the preferential exposed (101) facet shows a stronger signal at -34 ± 1 ppm **(Figure 6-14b)**, while for S-Na-(001) with the preferential exposed (001) facet gives a more dominant signal at -25.5 ± 1 ppm **(Figure 6-14c)**. For PD sample after the extension hydrolysis during treatments, surface multi-hydroxylation is expected to give a peak at -50 ± 1 ppm apart from the two LA peaks of -25.5 ± 1 ppm and -34 ± 1 ppm **(Figure 6-14a)**.

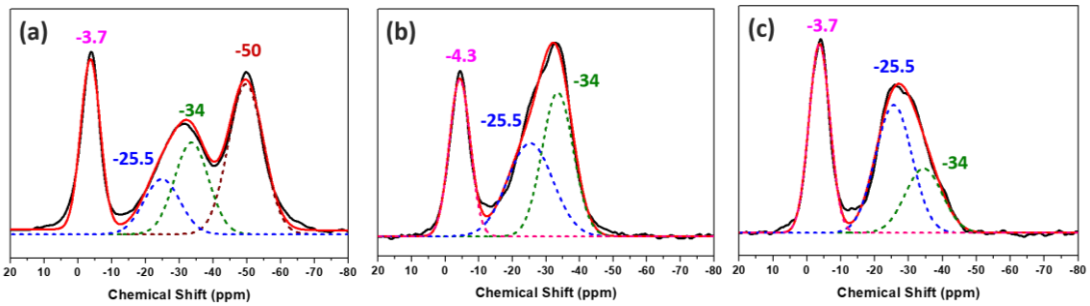

Figure 6-14. ^{31}P MAS NMR spectral deconvolution of TMP-adsorbed NaOH washed TiO_2 samples after following sulfation treatment (a) S-Na-PD, (b) S-Na-(101) and (c) S-Na-(001).

6.3.4. Summary of ^{31}P MAS NMR results

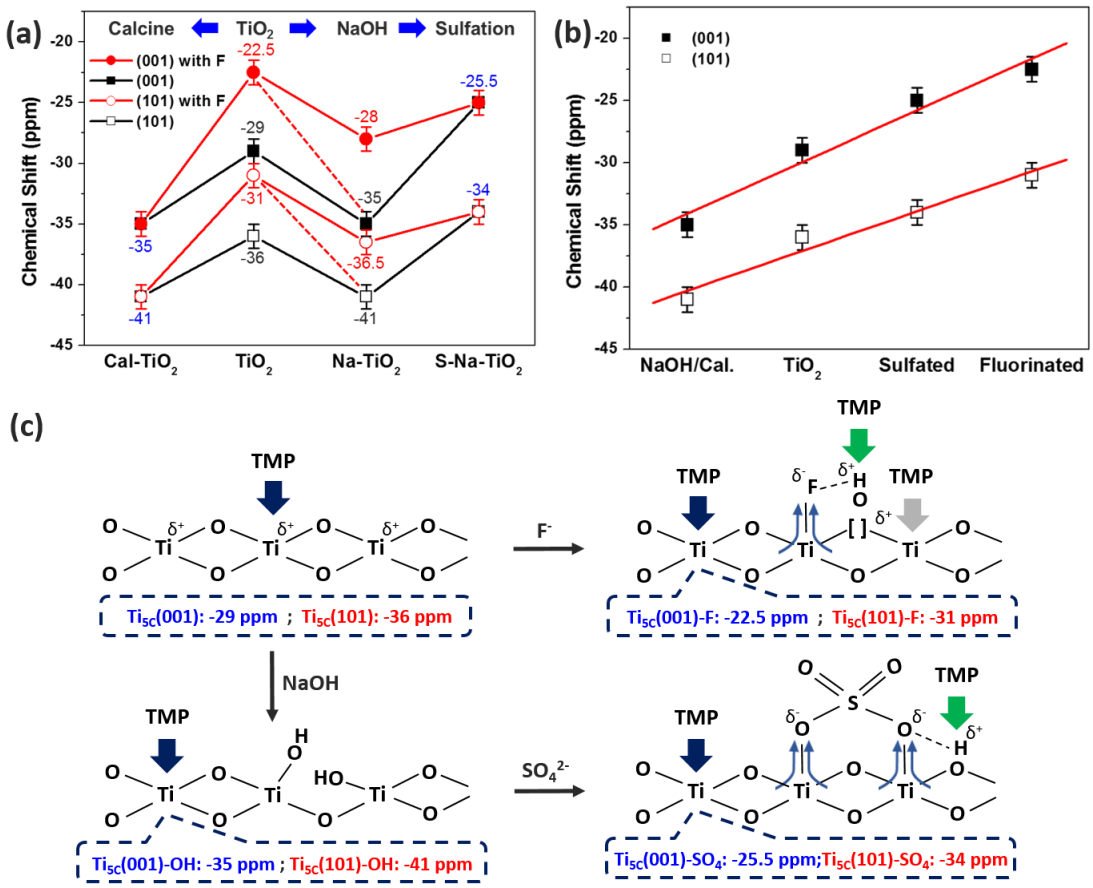

Figure 6-15. (a) The δ^{31}P of TMP-adsorbed Ti_{5C} on (001)/(101) facets (from PD) and on F-modified (001)/(101) facets (from F-(001) and F-(101)) with different treatments/modifications. (b) The summary of δ^{31}P of TMP-adsorbed Ti_{5C} on (001)/(101) facets with different treatments (calcination/NaOH wash) and modification (sulfate/fluorine). (c) Illustration of facet-dependent interaction between TMP and surface features on TiO_2 facets with various treatments/modifications.

Figure 6-15 and **Table 6-4** summarize qualitative (chemical shift) and quantitative (peak area) information of deconvoluted peaks in TMP-adsorbed TiO_2 ^{31}P MAS NMR spectra under various treatments. First, **Figure 6-15a** shows that the adsorption of TMP on LA centers of higher energy (001) facet gives lower chemical shift value (-29 ± 1 ppm) than that of the more stable (101) facet (-36 ± 1 ppm) in our samples. F treated (001) and (101) facets can clearly enhance the LA strengths, shifting them to -22.5 ± 1 ppm and -31 ± 1 ppm, respectively. This surface group with the highest electron

withdrawing ability can also generate oxygen vacancies hence activating the surfaces substantially. However, it is clear from our study that calcination in moisturized air at elevated temperature can indeed remove the surface F groups by introducing hydroxylation to the surfaces. Replacing F of strongest withdrawing propensity by much weaker surface OH group will render the upshifts to -35 ± 1 ppm for (001) facet and -41 ± 1 ppm for (101) facet due to mono-hydroxylation as mentioned previously (multi-hydroxylation can further upshifting the δ^{31}P of the adsorbed TMP). However, the high coverage of OH particularly on (001) facet at elevated temperature during calcination can concomitantly lead to severe aggregation. For prolong period of time, this can lead to stepwise reconstruction of (1 × 1) (001) facets to the more stable reconstructed (1 × 4) structure (at -50 ppm).

On the other hand, the replacement of surface F with OH using NaOH wash at room temperature can also achieve the F removal but retain the integrity of interested facets from significant aggregation and reconstruction, giving the same shift values of -35 ± 1 ppm for (001) facet and -41 ± 1 ppm for (101) facet. However, our TMP-adsorbed technique supported by XPS shows clearly that NaOH wash at room temperature may not be sufficient to remove all surface F from the TiO_2. If F is retained together with the mono-hydroxylated OH can give two new δ^{31}P values (different LA strengths) of TMP-adsorbed F-Ti_{5c}(001)/F-Ti_{5c}(101) of -28 ± 1 ppm /-36.5 ± 1 ppm **(Figure 6-15a)**. In addition, two strong BA strengths (the formation of $TMPH^+$) at -2.9 ppm **(Figure 6-9b)** and -2.4 ppm **(Figure 6-9c)** are also achieved due the proton stabilization by residue F left on both Na-(101) and Na-(001) sample surfaces. Upon extension sulfation after the samples are calcined or NaOH washed to replace all F with SO_4, weaker BA strengths between -3.7 ~ -4.7 ppm with protons influenced by neighbour SO_4 are obtained **(Figure 6-13 and Figure 6-14)**. In terms of LA alteration, -25.5 ± 1 ppm from

sulfation of (001) and -34 ± 1 ppm of (101) facets can be tuned. **Figure 6-15b** shows the highly sensitive $\delta^{31}P$ value towards increasing electron withdrawing ability to the surface Ti^{4+} from OH < -O- < SO_4 < F which can provide fine-tuning of LA and BA sites on TiO_2 facets by these surface additives. **Figure. 6-15c** summarizes the anticipated molecular interactions between TMP and surface features on TiO_2 with various treatments/modifications.

Samples	BA site (-2~-5 ppm)		LA sites (-20~-58 ppm)						
	ppm	Total TMP*	Ti_{5c}(001) (ppm)	TMP*	Ti_{5c}(101) (ppm)	TMP*	Others (ppm)	TMP*	Total TMP*
F-(001)	-2.6	89.4	-22.5	53.2	-31	32.0	-42.5	33.1	118.3
Cal-(001)	-	-	-35	21.9	-41	32.9	-45/-50	61.6/28.6	145
Na-(001)	-2.4	30.9	-28	135.1	-36.5	149.1	-41	181.6	465.8
S-Cal-(001)	-4.7	70.7	-	-	-	-	-	-	-
S-Na-(001)	-3.7	91.4	-25.5	116.4	-34	53.6	-	-	170.0
F-(101)	-2.7	50.1	-22.5	72.4	-31	57.1	-42.5	60.9	190.4
Na-(101)	-2.9	5.8	-28	96.0	-36.5	222.6	-41	117.8	436.4
S-Na-(101)	-4.3	83.6	-25.5	97.5	-34	105.6	-	-	203.1
PD	-	-	-29	106.8	-36	605.3	-	-	712.1
Cal-PD	-	-	-35	12.7	-41	66.2	-50	5.9	84.8
Na-PD	-	-	-35	143.3	-41	393.9	-46	59.7	596.9
S-Cal-PD	-3.9	85.4	-	-	-	-	-	-	-
S-Na-PD	-3.7	128.7	-25.5	75.6	-34	117.1	-50	191.2	383.9

Table 6-4. Summary of the qualitative (chemical shift) and quantitative (peak area) of each deconvoluted peak in the region of BA site (-2 ~ -5 ppm) and LA site (-20 ~ -58 ppm). The concentration of adsorbed TMP on each site was calculated according to corresponding peak area (*Adsorbed TMP molecules in μmol/g).

In addition, the TMP assisted NMR technique displays quantitative assessments on the surface speciation **(Table 6-4)**. The total adsorbed TMP over different samples also show strong correlations with the total BET surface areas of the samples (BET of S-Na-PD = 107.0 m^2/g, S-Na-(101) = 77.3 m^2/g and S-Na-(001) = 67.4 m^2/g **(Table 6-5)**, which proportional to their total TMP/g (both BA and LA from **Table 6-4**) uptakes of 512.6, 286.7 and 261.4 μmol/g, respectively). Typically, this new technique shows a better surface sensitivity for example, 5.8 μmol/g BA stabilized by F on Na-(101) is

detectable by the NMR **(Table 6-4)** but no corresponding F signal is observed by XPS **(Figure 6-5b)**. It is particularly noted that XPS fails to reveal the change in Ti_{2P} electronic state w/o fluorine **(Figure 6-5)** but ^{31}P MAS NMR can lead to their detailed assessments **(Table 6-4)**.

Powder	BET (m^2/g)	(101)	BET (m^2/g)	(001)	BET (m^2/g)
PD	123.3	F-(101)	163.0	F-(001)	83.0
Cal-PD	15.8	Cal-(101)	40.8	Cal-(001)	29.9
Na-PD	145.4	Na-(101)	152.4	Na-(001)	85.1
S-Na-PD	107.0	S-Na-(101)	77.3	S-Na-(001)	67.4

Table 6-5. BET surface area of TiO_2 samples.

6.3.5. DFT calculation

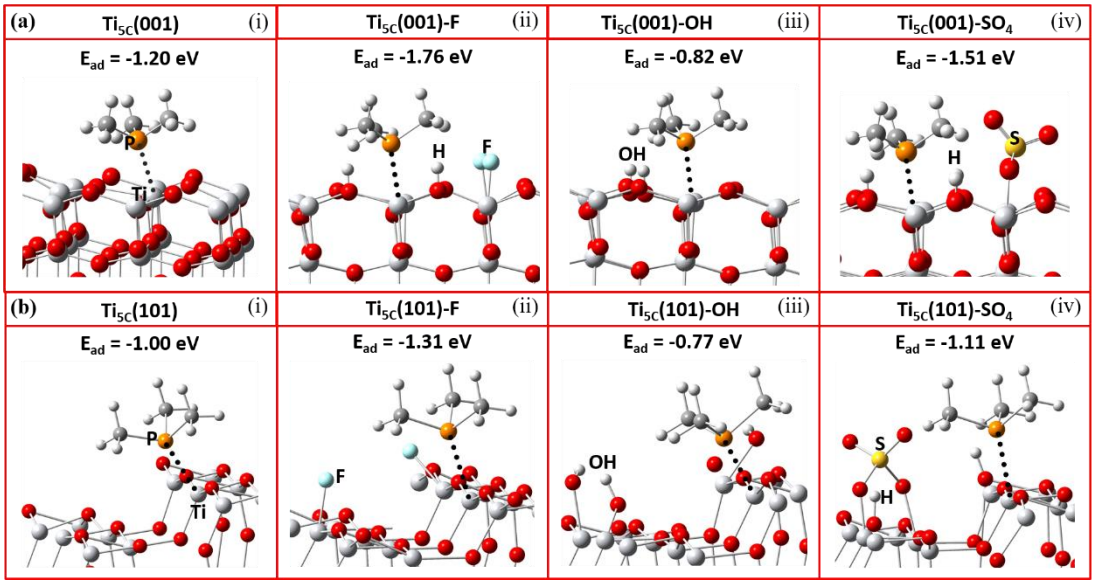

Figure 6-16. Schematic illustrations of molecular interaction and DFT calculated adsorption energy (E_{ad}) between TMP and Ti_{5C} on TiO_2 (a) (001) and (b) (101) facets promoted with (i) -O-, (ii) -F, (iv) -OH and (v) -SO_4 groups. (Ti: light grey; O: red; P: orange; C: grey; H: white; S: yellow) (carried out by Prof. Hung-Lung Chou).

It is expected that the stronger Lewis acid-base interaction between adsorbate and surface Ti give stronger surface adsorption. To confirm the effects of various adsorbates to surface Ti chemical states among facets, we then carried out DFT investigation of -

O-, F-, OH-, SO_4-attached (001) and (101) facets and calculated the corresponding adsorption energy (E_{ad}) of TMP **(Figure 6-16)**. For (001) facet, the E_{ad} between TMP and Ti_{5C} on the clean (001) facet is greatly increased from -1.20 eV **(Figure 6-16a(i))** to -1.76 eV **(Figure 6-16a(ii))** when surrounding Ti_{5C} is fluorinated. This can be supported by our experimental result that a 7 ppm downfield shift from -29 ppm of Ti_{5C}(001) in PD sample to -22.5 ppm of Ti_{5C}(001)-F in both F-(101) and F-(001) samples **(Figure 6-15a)**. Similar increase in the E_{ad} (from -1.2 to -1.51 eV, **Figure 6-16a(iv)**) and downfield shift in experimental chemical state (from -29 to -25.5 ppm, **Figure 6-15a**) can be observed also for sulphated (001) facet (Ti_{5C}(001)-SO_4) (cf. clean (001) facet). Both cases support the reported downward shift of electronic energy levels induced by Lewis-basic adsorbate [1]. Conversely, a decrease in the E_{ad} of TMP from -1.2 to -0.82 eV observed upon hydrolysis of clean (001) facet (i.e. Ti_{5C}(001)-OH, **Figure 6-16a(iii)**) can be supported by the NaOH treatment associated with the upshift of $\delta^{31}P$ from -29 ppm to -35 ppm (Ti_{5C}(001)-OH, **Figure 6-15a**). Accordingly, the electronic effect of adsorbates to the E_{ad} of TMP on Ti_{5C}(001) matches the order derived experimentally: -F > -SO_4 > -O- > -OH. Similar trend but lower calculated E_{ad} of TMP for each adsorbates can be found for Ti_{5C}(101) **(Figure 6-16b)**.

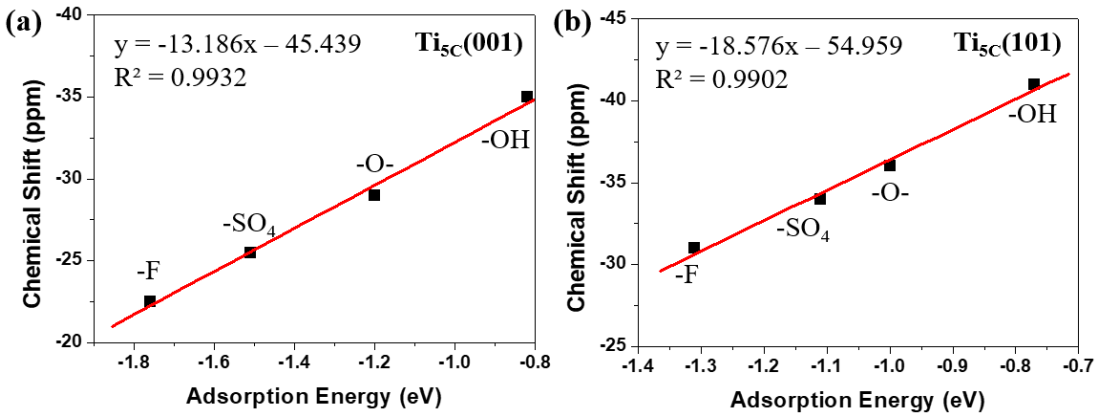

Figure 6-17. A linear regression plot by using experimental $\delta^{31}P$ and calculated adsorption energy on TiO_2 (a) (001) and (b) (101) facets promotes with various -O-, -F, -OH and -SO_4 groups.

It has been observed that the E_{ad} of TMP molecule on Lewis acid site shows a strong correlation with its NMR chemical shift value [7,41,42]. Indeed, it is found that the calculated E_{ad} displays an excellent linear relationship with the experimental chemical shift value obtained for both (001) **(Figure 6-17a)** and (101) **(Figure 6-17b)** facets promotes with various -O-, -F, -OH and -SO_4 groups. Noticeably, different y-axis intercepts were obtained for Ti_{5C}(001) (-45.439 ppm) and Ti_{5C}(001) (-54.959 ppm) when the E_{ad} of TMP is zero on these two facets. According to DFT calculation from literatures, the (101) surface couples strongly with bulk and can be regarded as an extension of bulk states, while the (001) surface strongly deviates from the bulk due to the surface stress-induced orbital interactions and thus gives rise to its unique reactivity [48]. As the stronger TMP-Ti bond formation would push $\delta^{31}P$ toward downfield, the ~9.5 ppm difference can be attributed to the intrinsic electronic structure of (001) and (101) facets. Here, the unusual strong molecule affinity to Ti_{5C} on (001) facet (cf. Ti_{5C} on (101) facet) is, for the first time, qualitatively observed by this technique and may explain the reported dissociative adsorption of water on (001) facet (cf. associative adsorption on (101) facet) [32,49]. On the other hand, it is thought that the slight steeper slope (-13.186, **Figure 6-17a**) obtained for Ti_{5C}(001) promoted with various adsorbates under the same surface treatments may indicate a higher degree of surface coverage for stronger adsorbates such that the -F and -SO_4 as compared to that of (101) facet (-18.576, **Figure 6-17b**).

6.3.6. Catalytic testing

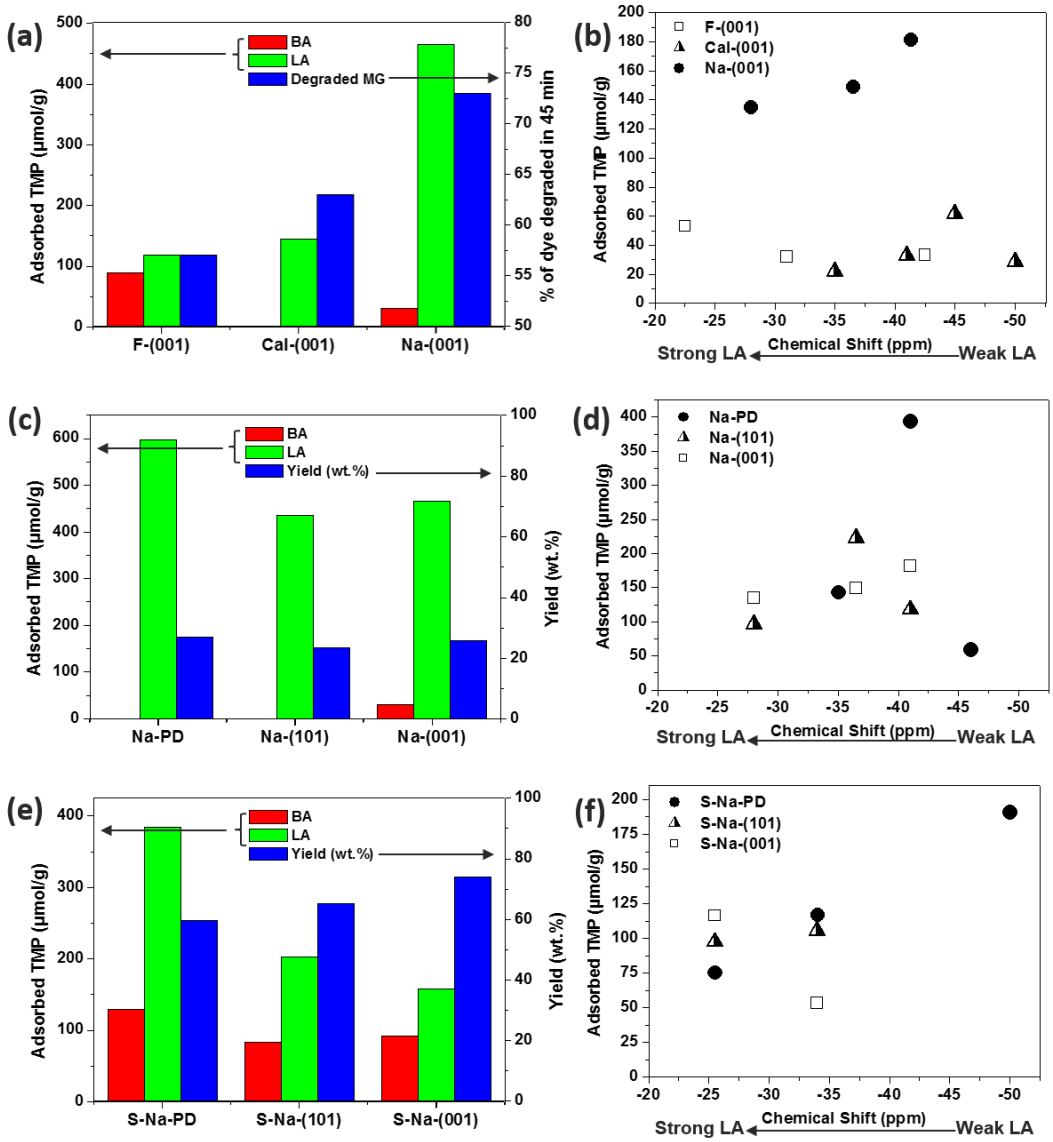

Figure 6-18. Comparison of BA and LA for (a) photocatalytic decomposition rate of Malachite Green (MG) dye in 45 min over F-(001) samples with various treatments. Pechmann condensation activity over (c) NaOH treated samples and (e) further sulfated samples. (b), (d) and (f) are corresponding concentrations of LA sites of tested samples with different strengths.

It is well accepted that photocatalytic activity is highly dependent on particular facets of transition metal oxide crystals. Pioneered by Han *et al.* [13] and Yang *et al.* [14], using sheet-like TiO_2 with higher percentage of reactive (001) facet was proved to exhibit higher photocatalytic activity in aqueous medium (cf. P25). Both of the above

reports in literature also showed that the photocatalytic efficiency of the TiO_2 nanosheets can be further improved after removing surface fluorine either by calcination [12,14] or NaOH wash [13]. However, the changes in the quantity and quality of active sites on this (001) facet upon the above treatments were still unable to offer detailed analysis and assessment due to the lack of appropriate characterization techniques [12-31]. To illustrate the importance of acquiring the delicate surface electronic and structural changes imposed by particular facet and surface chemical modifier, the influence of various treatments to TiO_2 surface features were monitored **(Table 6-4)**. The photocatalytic decomposition rate of Malachite Green (MG) upon F-(001), Cal-(001) and Na-(001) in static solution was therefore studied to re-assess the surface structure-photocatalytic activity relationships [13-24]. Corresponding results are shown in **Figure 6-18a**.

For samples with the preferential exposure of (001) facet, the NaOH washed F-(001) sample (i.e. Na-(001)) shows the highest photo-decomposition efficiency while the sample without any treatment (i.e. F-(001)) shows the lowest efficiency (activity: Na-(001) > Cal-(001) > F-(001)). This result indicates that neither crystallinity nor surface area are the key factors. This is because F-(001) possessing similar crystallinity **(Figure 6-8)** / surface area **(Table 6-5)** as Na-(001) and giving higher surface area than Cal-(001) shows the lowest activity. The role of surface defect such as V_o is also proved to be minor as both XPS Ti to O ratio **(Table 6-2)** and quantitative EPR signal at g~2.0 **(Table 6-3)** suggest the V_o concentration is in a reverse order: F-(001) > Cal-(001) > Na-(001). According to our NMR results, the possibility of BA playing a key role is also ruled out as the Cal-(001) with no detectable BA exhibits higher % of MG degradation rate than F-(001) with the highest BA concentration in solution. The acid strength of LA also doesn't seem to play the key role in this reaction either as F-(001)

with the strongest LA site (at ~ -22 ppm, **Figure 6-18b**) exhibits the lowest activity. In this case, the total LA concentration (465.8 μmol/g of Na-(001) > 145 μmol/g of Cal-(001) > 118.3 μmol/g of F-(001)) appears to be the primary cause for this activity **(Figure 6-18a)** as it is proportional to the rate and yield of photo-decomposition of the MG molecules. As the fluorine binds strongly to the surface Ti atom (blocking the LA site) on (001) facet, it is not surprising that its removal by NaOH wash in the Na-(001) sample with similar particle size (cf. F-(001)) has quadrupled the LA surface concentration. Despite the fact that severe aggregation is taken place over the calcined Cal-(001) sample, which also possesses a higher LA concentration (cf. F-(001)). This indicates that the type and concentration of surface features are the key factors for the observed difference in the decomposition rates. This result can be supported by the observation of our previous study which found that the small degree of adsorption of dye molecules due to limited Lewis acid sites was the rate-determining step for photo-catalytic reaction in the Nb_2O_5 case in static solution [50].

However, the photocatalytic reaction carried out in the flowing air seems to depend on LA strength more than the total LA concentration. Xiang *et al.* reported that F-TiO_2 gives better activity than treated TiO_2 (i.e. Cal-TiO_2 and Na-TiO_2) for the photocatalytic degradation of acetone in flowing air [19]. They suggested the strong electron-withdrawing ability of the surface Ti-F groups reduces the recombination of photo-generated electrons and holes, and enhances the photocatalytic activity. While, according to our result, we believe the adsorption dynamic of acetone in flowing air is very different from that of dye in static water and can only be efficiently adsorbed from the gas phase by the stronger LA site of F-TiO_2 (e.g. -22 ppm, **Figure 6-18b**) before the photodecomposition. Thus, the stronger nature of LA site of F-TiO_2 renders higher activity than that of treated TiO_2 (i.e. Cal-TiO_2 and Na-TiO_2) in the gas phase

degradation of acetone in air.

To demonstrate the importance of assessment of electronic and structural states on facets in both qualitatively and quantitatively in heterogeneous catalysis, the catalytic performances of Na-PD, Na-(101), Na-(001) and corresponding sulfation samples (i.e. S-Na-PD, S-Na-(101) and S-Na-(001)) for catalytic Pechmann condensation reaction using phloroglucinol and ethyl acetoacetate as starting reagents were carried out and the results are shown in **Figure 6-18c** and **Figure 6-18e**. In view of Pechmann reaction, the condensation of phenol and β-keto ester proceeds through transesterification followed by intramolecular hydroalkylation and dehydration [51]. As shown in **Figure 6-18c**, the yield of 5,7-dihydroxy-4-methyl coumarin of Na-PD (27.13 wt. %) ≥ Na-(001) (25.86 wt. %) = Na-(101) (23.53 wt. %) in solution shows a slight correlation with total LA concentration but both LA strength **(Figure 6-18d)** and the trace BA of Na-(001) show almost no significantly influence (total concentration of LA is more important than its strength in solution catalysis as previously discussed). However, the yield is almost tripled when using corresponding sulfation samples in the order of S-Na-(001) (73.87 wt. %) > S-Na-(101) (65.16 wt. %) > S-Na-PD (59.68 wt. %) **(Figure 6-18e)**. This huge increase in yield for all the three samples could be easily mistakenly attributed to the introduction of weak BA by sulfate modification at the expense of LA sites **(Figure 6-18c and Figure 6-18e)**. However, S-Na-PD with the highest total concentrations in both BA and LA shows the lowest yield among the three samples and similar BA strength is actually obtained for all the three samples. Thus, BA does not seem to be the main active site for this catalyzed reaction. Notice that the sulfate modification of S-Na-PD, S-Na-(101) and S-Na-(001) also concomitantly introduces a new LA site of much stronger strength than unmodified samples **(Figure 6-18f)**. The strength of this newly generated LA site at ~ -25 ppm (Ti^{4+} modified directly by the

neighbours SO_4 and OH, **Figure 6-15c**) is found to be comparable to sulfated/BF_3-modified metal oxides (SO_4^{2-}/ZrO_2 [52], BF_3/Al_2O_3 [53]) which is characteristic of super Lewis acidity. This LA concentration is clearly found to be in the order of S-Na-(001) > S-Na-(101) > S-Na-PD **(Figure 6-18f)** in according with the order of their product yield, which undoubtedly suggests that the specific concentration of this new-generated super acid site is responsible to catalyze this reaction in solution accordingly.

6.4. Chapter conclusion

Nanometer dimensions and intrinsic heterogeneity of NPs that each particle typically exposes several facets with different patterns of surface atoms make experimental study of surfaces challenging. |For instance, the uses of surface directing species (SDS) to alter nanoparticle morphology and physico-chemical properties of particular exposed facets have recently been attracting a significant attention. However, the challenges in their chemical analysis sometimes at trace levels, understanding their roles to elucidate surface structure-activity relationships and their removals, are of great significance that remain to be solved. Traditional tools such as XPS and EPR have been widely employed to bridge facet-controlled NPs and their corresponding facet-dependent performances. However, as demonstrated in this study (using TiO_2), those techniques (XPS: **Figure 6-5**; EPR: **Table 6-3**) can only provide very limited information on the chemical state of surface cations and their distribution among facets, causing difficulty to explain corresponding facet-dependent results. Moreover, various processing steps and post-treatment techniques (e.g. NaOH/calcination treatment here) used during the preparation of NPs from group to group further complicate surface environment and always lead to different interpretations and disagreements amongst researchers.

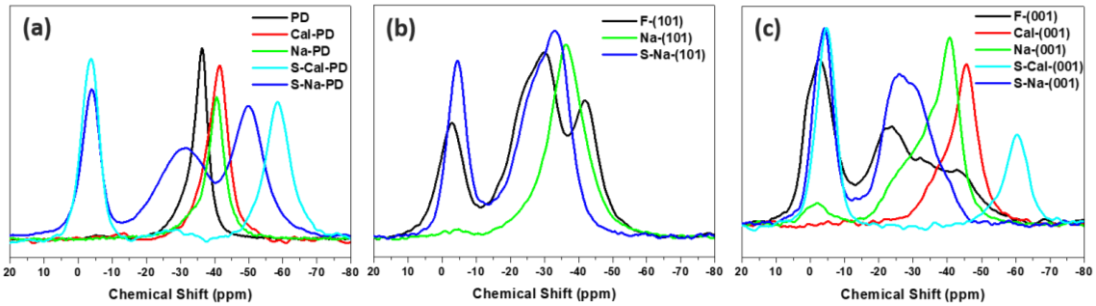

Figure 6-19. Summary of the electronic effect (chemical shift) imposed by different adsorbates during sequential treatments/modifications on (a) PD, (b) F-(101) and (c) F-(001) with various exposed facets.

Herein, qualitative and quantitative information on both chemical state and distribution of surface cations among facets promoted with various groups have been well-resolved achieved by the assistance of NMR-active probe **(Figure 6-19)**. We show a detailed analysis of TiO_2 facets promoted with surface species (OH, O, SO_4, F) w/o post-treatments (calcination or NaOH wash) by ^{31}P adsorbate-NMR supported with a range of other characterization tools. Quantitative evaluations of the electronic and structural effects imposed by these surface additives and their removal mechanisms were monitored for the first time during sequential treatments/modifications to NP surface cation. The photocatalytic dye decomposition and Pechmann condensation reaction were carried out to illustrate the importance of acquiring the delicate surface electronic and structural changes imposed by particular facet and surface chemical modifier. We showed that the LA strength is the key factor when photocatalytic reaction is carried out in the flowing air, while the total LA concentration is more important than the acid strength effect in in closed water. We believe this difference is due to the adsorption dynamic of molecule in flowing air is very different from that of dye in closed water environment and can only be efficiently adsorbed from the gas phase by the stronger LA site. For Pechmann condensation reaction, the condensation of phloroglucinol and ethyl acetoacetate to 5,7-dihydroxy-4-methyl coumarin has been reported can be catalyzed by either LA or BA sites. However, we show here that BA can be more efficiently than mild LA, while LA will be dominant when it becomes superacid.

It is noted that the employment of a NMR chemical probe to aid to characterize the acidity of zeolite was introduced firstly by Lunsford *et al.*(1984) [54] and utilized for various solid acid catalysts nowadays [55]. However, there is no report regarding its potential use in differentiating adsorbate-dependent chemical state of cations on various crystal facets, which can be crucial for filling the gap between the model catalysts used

in surface science and the real catalysts found in practical applications. It is clear from this study that type and quantity of surface Ti electronic state and structure are highly sensitive to the intrinsic nature and the amount of particular facets, SDS and additives used as well as treatment methods adopted (calcination or NaOH wash), etc. They play decisive role(s) for a wide range of TiO_2 applications especially optical and thermal catalysis, which are closely associated with the coordination environment and the chemical state of surface titanium atoms at the catalyst surface. Hence, we believe that this study gives new insights to resolve the current debates and confusions in some facet-dependent properties in literature, should more comprehensive surface characterization including ^{31}P adsorbate assisted MAS NMR can be invoked.

References

[1] M. A. Boles, D. Ling, T. Hyeon,D. V. Talapin, *Nat. Mater.* **2016**, *15*, 141–153.

[2] X. Zhang, J. Qin, Y. Xue, P. Yu, B. Zhang, L. Wang, R. Liu, *Sci. Rep.* **2014**, *4*, 4596.

[3] D. N. Mueller, M. L. Machala, H. Bluhm, W. C. Chueh, *Nat. Commun.* **2015**, *6*, 6097.

[4] A. Llordés, Y. Wang, A. Fernandez-Martinez, P. Xiao, T. Lee, A. Poulain, O. Zandi, C. A. Saez Cabezas, G. Henkelman, D. J. Milliron, *Nat. Mater.* **2016**, *15*, 1267−1273.

[5] O. Zandi, T. W. Hamann, *Nat. Chem.* **2016**, *8*, 778–783.

[6] G. R. Li, T. Hu, G. L. Pan, T. Y. Yan, X. P. Gao, H. Y. J. Zhu, *Phys. Chem. C* **2008**, *112*, 11859−11864.

[7] Y. K. Peng, L. Ye, J. Qu, L. Zhang, Y. Fu, I. F. Teixeira, I. J. McPherson, H. He, S. C. E. Tsang, *J. Am. Chem. Soc.* **2016**, *138*, 2225−2234.

[8] Y. Yin, A. P. Alivisatos, *Nature* **2005**, *437*, 664−670.

[9] M. S. Bakshi, *Cryst. Growth Des.* **2016***, 16*, 1104−1133.

[10] S. Liu, J. Yu, M. Jaroniec, *Chem. Mater.* **2011**, *23*, 4085–4093.

[11] G. Liu, H. G. Yang, J. Pan, Y. Q. Yang, G. Q. Lu, H.-M. Cheng, *Chem. Rev.* **2014**, *114*, 9559−9612.

[12] H. G. Yang, C. H. Sun, S. Z. Qiao, J. Zou, G. Liu, S. C. Smith, H. M. Cheng, G. Q. Lu, *Nature* **2008**, *453*, 638−641.

[13] X. Han, Q. Kuang, M. Jin, Z. Xie, L. Zheng, *J. Am. Chem. Soc.* **2009**, *131*, 3152–3153.

[14] H. G. Yang, G. Liu, S. Z. Qiao, C. H. Sun, Y. G. Jin, S. C. Smith, J. Zou, H. M. Cheng, G. Q. Lu, *J. Am. Chem. Soc.* **2009**, *131*, 4078–4083.

[15] S. Liu, J. Yu, M. Jaroniec, *J. Am. Chem. Soc.* **2010**, *132*, 11914–11916.

[16] J. Pan, G. Liu, G. Q. Lu, H.-M. Cheng, *Angew. Chem. Int. Ed.* **2011**, *50*, 2133–2137.

[17] T. R. Gordon, M. Cargnello, T. Paik, F. Mangolini, R. T. Weber, P. Fornasiero, C. B. Murray, *J. Am. Chem. Soc.* **2012**, *134*, 6751−6761.

[18] J. Yu, L. Qi, M. Jaroniec, *J. Phys. Chem. C* **2010**, *114*, 13118–13125.

[19] Q. Xiang, K. Lv, J. Yua, *Appl Catal B.* **2010**, *95*, 557–564.

[20] Y. Jiang, J. Scott, R. Amal, *Appl Catal B.* **2012**, *126*, 290–297.

[21] T. Tachikawa, S. Yamashita, T. Majima, *J. Am. Chem. Soc.* **2011**, *133*, 7197–7204.

[22] M. D'Arienzo, J. Carbajo, A. Bahamonde, M. Crippa, S. Polizzi, R. Scotti, L. Wahba, F. Morazzoni, *J. Am. Chem. Soc.* **2011**, *133*, 17652–17661.

[23] J. Yu, J. Low, W. Xiao, P. Zhou, M. Jaroniec, *J. Am. Chem. Soc.* **2014**, *136*, 8839−8842.

[24] X. Yu, B. Jeon, Y. K. Kim, *ACS Catal.* **2015**, *5*, 3316−3322.

[25] F. Xiong, Y.-Y. Yu, Z. Wu, G. Sun, L. Ding, Y. Jin, X.-Q. Gong, W. Huang, *Angew. Chem. Int. Ed.* **2016**, *55*, 623–628.

[26] J. Yu, J. Fan, K. Lv, *Nanoscale* **2010**, *2*, 2144–2149.

[27] X. Wu, Z. Chen, G. Q. Lu, L. Wang, *Adv. Funct. Mater.* **2011**, *21*, 4167–4172.

[28] F. Hao, X. Wang, C. Zhou, X. Jiao, X. Li, J. Li, H. Lin, *J. Phys. Chem. C* **2012**, *116*, 19164−19172.

[29] L. Chu, Z. Qin, J. Yang, X. Li, *Sci. Rep.* **2015**, *5*, 12143.

[30] J. S. Chen, Y. L. Tan, C. M. Li, Y. L. Cheah, D. Luan, S. Madhavi, F. Y. C. Boey, L. A. Archer, X. W. Lou, *J. Am. Chem. Soc.* **2010**, *132*, 6124–6130.

[31] X.-L. Cheng, M. Hu, R. Huang, J.-S. Jiang, *ACS Appl. Mater. Interfaces* **2014**, *6*, 19176−19183.

[32] S. Selçuk, A. Selloni, *J. Phys. Chem. C* **2013**, *117*, 6358−6362.

[33] W. Yuan, Y. Wang, H. Li, H. Wu, Z. Zhang, A. Selloni, C. Sun, *Nano Lett.* **2016**,

16, 132–137.

[34] L. Atanda, S. Mukundan, A. Shrotri, Q. Ma, J. Beltramini, *ChemCatChem* **2015**, *7*, 781–790.

[35] L. Atanda, A. Shrotri, S. Mukundan, Q. Ma, M. Konarova, J. Beltramini, *ChemSusChem* **2015**, *8*, 2907–2916.

[36] X. C. Wang, J. C. Yu, P. Liu, X. X. Wang, W. Y. Su, X. Z. Fu, *J. Photochem. Photobiol. A* **2006**, *179*, 339−347.

[37] H. Zhang, H. Yu, A. Zheng, S. Li, W. Shen, F. Deng, *Environ. Sci. Technol.* **2008**, *42*, 5316–5321.

[38] B. E. Hardin, H. J. Snaith, M. D. McGehee, *Nat. Photonics* **2012**, *6*, 162–169.

[39] H. Kusama, H. Orita, H. Sugihara, *Langmuir* **2008**, *24*, 4411–4419.

[40] M. Lazzeri, A. Vittadini, A. Selloni, *Phys. Rev. B* **2001**, *63*, 155409.

[41] Y. Chu, Z. Yu, A. Zheng, H. Fang, H. Zhang, S.-J. Huang, S.-B. Liu, F. Deng, *J. Phys. Chem. C* **2011**, *115*, 7660−7667.

[42] K. Tedsree, C. W. A. Chan, S. Jones, Q. Cuan, W.-K. Li, X.-Q. Gong, S. C. E. Tsang, *Science* **2011**, *332*, 224−228.

[43] Y. K. Peng, Y. Fu, L. Zhang, I. F. Teixeira, L. Ye, H. He, S. C. E. Tsang, *ChemCatChem* **2017**, *9*, 155–160.

[44] Z. R. Ismagilov, L. T. Tsykoza, N. V. Shikina, V. F. Zarytova, V. V. Zinoviev, S. N. Zagrebelnyi, *Russ. Chem. Rev.* **2009**, *78*, 873–885.

[45] D. J. Belton, O. Deschaume, C. C. Perry, *FEBS J.* **2012**, *279*, 1710-1720.

[46] X. H. Yang, Z. Li, C. Sun, H. G. Yang, C. Li, *Chem. Mater.* **2011**, *23*, 3486–3494.

[47] K. Lv, Q. Xiang, J. Yu, *Appl Catal B.* **2011**, *104*, 275–281.

[48] H. Chen, J. A. Dawson, N. Umezawa, *Phys. Rev. Applied,* **2015**, *4*, 014007.

[49] Y. Shi, H. Sun, W. A. Saidi, M. C. Nguyen, C. Z. Wang, K. Ho, J. Yang, J. Zhao, *J. Phys. Chem. Lett.* **2017**, *8*, 1764−1771.

[50] Y. Zhao, C. Eley, J. Hu, J. S Foord, L. Ye, H. He, S. C. E. Tsang, *Angew. Chem. Int. Ed.* **2012**, *51*, 3846–3849.

[51] S. Sudha, K. Venkatachalam, S. Vishnu Priya, J. Herbert Mabel, M. Palanichamy, V. Murugesan, *J. Mol. Catal. A: Chem.* **2008**, *291*, 22–29.

[52] H. Yu, H. Fang, H. Zhang, B. Li, F. Deng, *Catal. Commun.* **2009**, *10*, 920–924.

[53] J. Yang, A. Zheng, M. Zhang, Q. Luo, Y. Yue, C. Ye, X. Lu, F. Deng, *J. Phys. Chem. B* **2005**, *109*, 13124–13131.

[54] W. P. Rothwell, W. Shen, J. H. Lunsford, *J. Am. Chem. Soc.* **1984**, *106*, 2452–2453.

[55] A. Zheng, S.-J. Huang, S.-B. Liu, F. Deng, *Phys. Chem. Chem. Phys.* **2011**, *13*, 14889–14901.

Chapter 7 Conclusions and future perspectives

Undoubtedly, the development of semiconductive transition metal oxides with tailored facets has been one of the most significant events in environment and electronics related photocatalytic research in the past decades. Ideally, the continuing development of these catalysts with facet-dependent activity would not only deepen the understanding of the structural sensitivity of such catalysts, by correlating their reaction performance with their dominant crystal facet, but also bridge the gap between the model catalysts used in surface science and the real catalysts found in practical applications Often, however, comparison of such facet-dependence is limited to individual studies, as the processing and post-treatments used in the preparation of catalysts or later removal of adsorbates (e.g. surfactant employed in facet control) varies from group to group. In most cases, those so-called "clean surfaces" were not so clean as they claimed since each facet possesses distinctive intrinsic energy that both concentration and chemical state of surface active features (V_o, OH, cations…etc.) should differ from facet to facet after reaching equilibrium with post-treatments.

As residue adsorbates have been shown remain on the facets and influence the adsorption of reactant molecules and the chemical states of surface active features. This forms an obstacle for reliably evaluating the facet-dependent photocatalytic performance. Moreover, from characterization side, traditional surface techniques such as PL, EPR and XPS are collecting data from the bulk of particle while not from the specific facets. Even though XPS have been regarded as the most sensitive technique to surface atomic chemical state, it fails to give any chemical shift of surface features in the presence of adsorbates. Accordingly, these traditional techniques provide very

limited information on the chemical state of surface active features and their distribution among facets, causing difficulty to unambiguously correlate facet-dependent results and thus always lead to different interpretations amongst researchers during the past decades. This thesis firstly reviews on how researchers have correlated the performance of faceted ZnO and TiO_2 nanoparticles to their activities. Those traditional techniques have been shown shortcomings in the characterization of facet-dependent features that some surface details have been missed in their study. To address this issue, chemical probe-molecule-assisted NMR was adopted in this thesis to differentiate surface active sites between facets (ZnO case, Chapter 4 and 5) or facets promoted with various surface groups (TiO_2 case, Chapter 6).

In Chapter 4, we firstly demonstrated this technique can provide comprehensive information (both qualitative and quantitative) on the surface features of faceted ZnO nanoparticles. As TMP, an electron donor molecule (Lewis base, LB), can form a stable adduct with the exposed cation of an oxide surface (Lewis acid, LA), the formation of a surface TMP-LA complex can be realized via coordination of the P atom to the LA center. It is shown that the ^{31}P chemical shift ($\delta^{31}P$) of the surface TMP-LA complex can differentiate between surface cations (Zn^{2+} or H^{+}) on facets at high resolution, with various Lewis acidities and surface energies due to the stronger LA site pushing $\delta^{31}P$ to downfield. Single-crystalline plate- and rod-shaped ZnO nanoparticles with preferentially exposed (002) and (100) facets, respectively and polycrystalline ZnO powder, were prepared to study the correlation between $\delta^{31}P$ and the adsorption configurations of TMP on various ZnO facets. Information such as the nature, binding strength and concentration of active sites on the various facets was shown can be obtained from a single ^{31}P solid-state NMR spectrum.

Later, in Chapter 5, the commonly used PL and EPR techniques were compared and shown to be incapable of providing quantitative Vo surface assessment to facet-dependent properties of ZnO nanoparticles. PL technique fails to deliver precise Vo surface with interferences from bulk defects. EPR is a surface technique but is found dependent on many experimental factors. The signal originated from trapped unpaired electron does not necessary correlate to Vo surface concentration due to equilibrium limitation and there are significant contributions from low coordination sites from polycrystalline particles. We further compared results from PL, EPR and NMR in correlating the photocatalytic decomposition activity of methylene blue (MB) of ZnO NPs for the study of facet-specific photocatalysis. The concentration of surface hydroxyl group has been shown the key factor that overrides the role of surface Vo, Zn_{3C} and O atoms in the MB photo-degradation. Based on this result, a new mechanism for photocatalytic •OH radical generation from direct surface-OH oxidation is revealed.

In Chapter 6, using anatase TiO_2 samples of different morphologies, we have successfully monitored the subtle changes of Ti chemical state induced by a small quantity of surface adsorbates (i.e. fluorine, sulfate, OH) on various facets using ^{31}P NMR with TMP as surface probe. Similar to ZnO case, the surface Ti cations on various facets with different Lewis acidities and surface energies can be mapped, differentiated and quantitatively analyzed. It is shown, for the first time, that some typical post-treatments (i.e. calcination or NaOH wash) to remove the fluorine (as SDS) can lead to different surface Ti chemical states. The photocatalytic dye decomposition and Pechmann condensation reaction were carried out to illustrate the importance of acquiring the delicate surface electronic and structural changes imposed by particular facet and surface chemical modifier. Accordingly, extra caution must be exercised for even trivial surface treatments as a huge difference in activity can be obtained. This

technique is thus demonstrated as a powerful tool in combination with conventional surface techniques adopted for TiO_2 NPs such as XPS and EPR to offer comprehensive information of surface features on various functionalized facets to guide surface treatments/modifications of TiO_2 nanoparticle for applications.

As demonstrated in this thesis, this advance in facet-specific characterization technique gives new insights to resolve the current debates and confusions in some facet-dependent properties in literature. In combining with traditional techniques, we believe this technique can open up a new route for the understanding of photocatalytic mechanisms. Overall, the development of semiconductive transition metal oxides with tailored facets and surface characterization techniques should keep pace with each other in order to unambiguously correlate the facet-dependent surface feature with corresponding performance.